Proceedings of the 4th BSME-ASME International Conference on Thermal Engineering
27-29 December, 2008, Dhaka, Bangladesh

AN EXPERIMENTAL INVESTIGATION ON GOLF SHOE DESIGN USING FOOT-PRESSURE DISTRIBUTION DURING THE GOLF SWING

Md. Tofajjal Hossain Chowdhury and Yong-Jin Kim

Division of Mechanical and Automotive Engineering, College of Engineering, Kongju National University, 275 Boodae-Dong, Cheonan, Chungnam-do, Korea

rashed9837@yahoo.com

ABSTRACT

The study aim to analyze the pressure and center-of-pressure (COP) under feet in order to design insoles inside the golf shoes during the golf swing. Four subjects were used for this study. COP and pressure are found to be important factors influencing the stability. For all subjects, overall instability is large in the left feet comparing to the right feet during the golf swing. During the swing phases (impact, follow-through, and end of follow-through), for all subjects, the left insoles should be designed laterally under toes, metatarsal head, midfoot, and heel regions in anterior-posterior direction, while for the right insoles, the design should be in the anterior part (metatarsal head and toe regions) in medial-lateral direction, according to the peak pressures.

Keywords: *Foot-pressure, COP, golf swing*.

1. INTRODUCTION

Golf is a sport enjoyed by different sectors of the public and by different ages which is expanded dramatically [5]. During the golf swing, foot is the only anatomical structure that comes in contact with the ground. Previous studies looked at the kinematic and kinetic aspects of the swing [1, 8]. Carlsoo [2] analyzed the ground reaction forces by using a pressure-sensitive plate during the golf swing in a Swedish player. By using force plates, Cooper, et al [3] examined forces generated by each foot separately to see the shift in the axis of the central load, with the axis itself being determined by Kinematographic techniques. In order to illustrate the kinematic and kinetic description of the feet during the golf swing, Williams and Cavanagh [10] studied the movements and the forces generated by the feet using force plates. The present study has examined the peak pressures and COP under feet during the golf swing to provide information about biomechanics of the feet, and then used this information to suggest design criteria for golf insoles, which would be suitable for the golfers.

2. METHOD

2.1. Subjects and Instrumentation

Four (two men and two women) professional golfers took part in this study (table 1). Two

clubs (driver and 7-iron) were used. The footscan® insole system (RSscan International, Olen, Belgium, 500Hz) was used to measure in-shoe pressures [4] and from the pressures it was calculated COP [6]. The experimental setup is illustrated in figure 1.

Table 1. Subjects characteristics: age, body weight, height, and handicap

Subjects	Age (yrs)	Body weight (kg)	Height (m)	Handicap
Man (1)	22	68	1.76	2 (Low)
Man (2)	31	63	1.73	3 (Low)
Woman (1)	21	71	1.75	8 (Medium)
Woman (2)	21	55	1.65	8 (Medium)

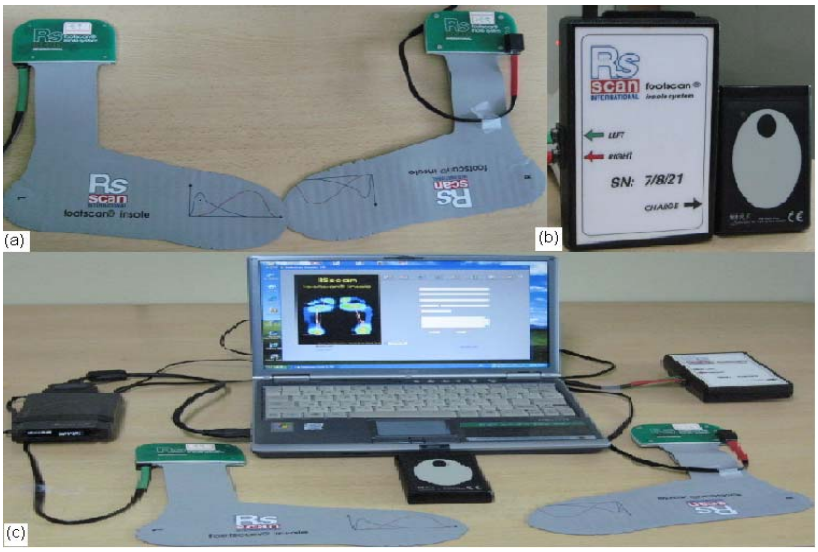

Figure 1. The experimental setup: (a) Rsscan insoles, (b) Data logger with remote control, (c) The footscan® insole system.

2.2. Data Collection and Analysis

By using insole system, data were recoded in a memory card (fig. 2) which enabled dynamic in-shoe pressure measurements including 2s swing (backswing, downswing, impact and following-through) data, for both feet during 8s. In this insole system, landmarks (T1-T5, M1-M5, V1-V4, H1-H4: fig. 2) are located on the pressure images, which are based on the anatomical structures of the foot. The measurements data were analyzed using footscan® insole 2.39 software, in which the subjects body weight was used. It is considered the swing phases (impact: F, follow-through: G, and end of follow-through: H: fig. 4a, 4b, 4c & 4d) to analyze the peak pressures and COP in order to design insoles. In this study, the results are considered only for driver club condition for all subjects. As there is no significant differences in the pressures between the clubs at the time before impact, so the patterns of pressure distribution during the swing are not affected by the clubs.

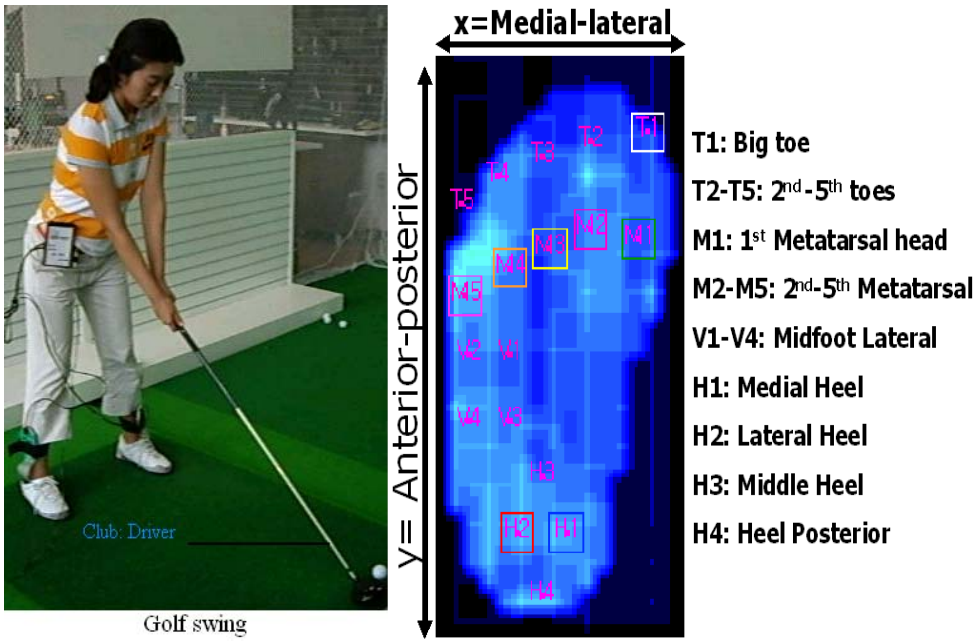

Figure 2. Experimental data collection during the golf swing and the 2D foot pressure screen represents eighteen anatomical landmarks.

3. RESULTS

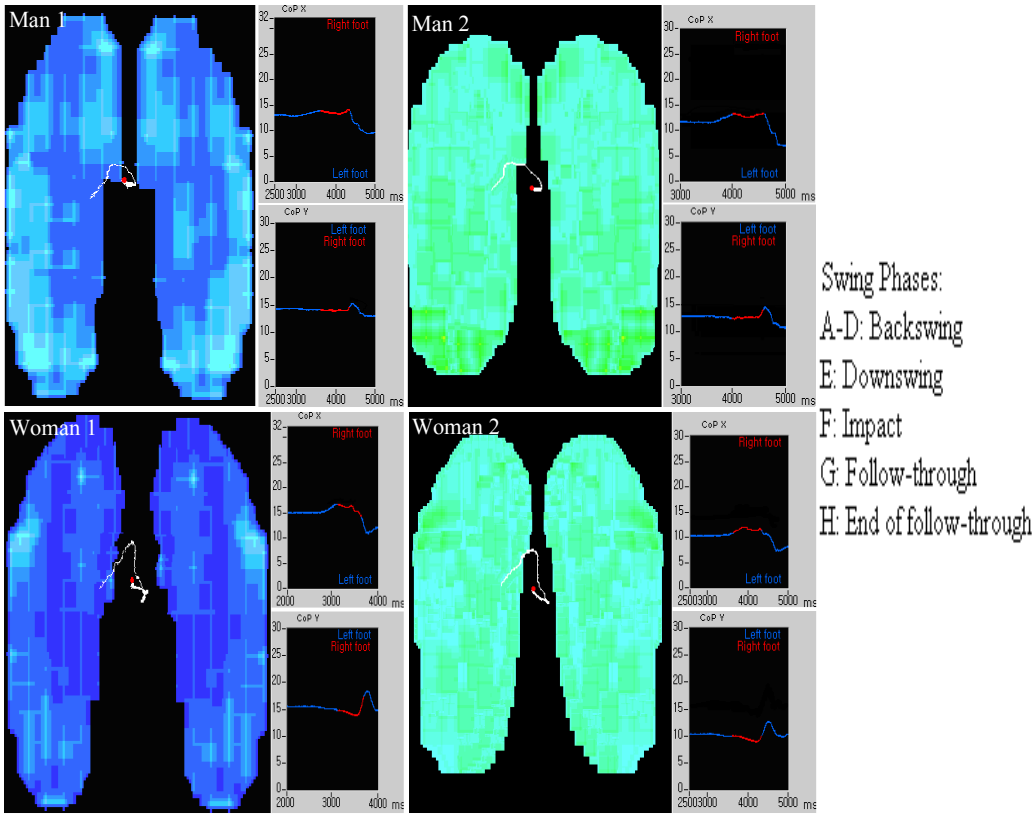

Figure 3. The COP screen (2D views) and COPx (medial-lateral)-time as well as COPy (anterior-posterior)-time curves: (a) for man (1), (b) for man (2), (c) for woman (1), and (d) for woman (2).

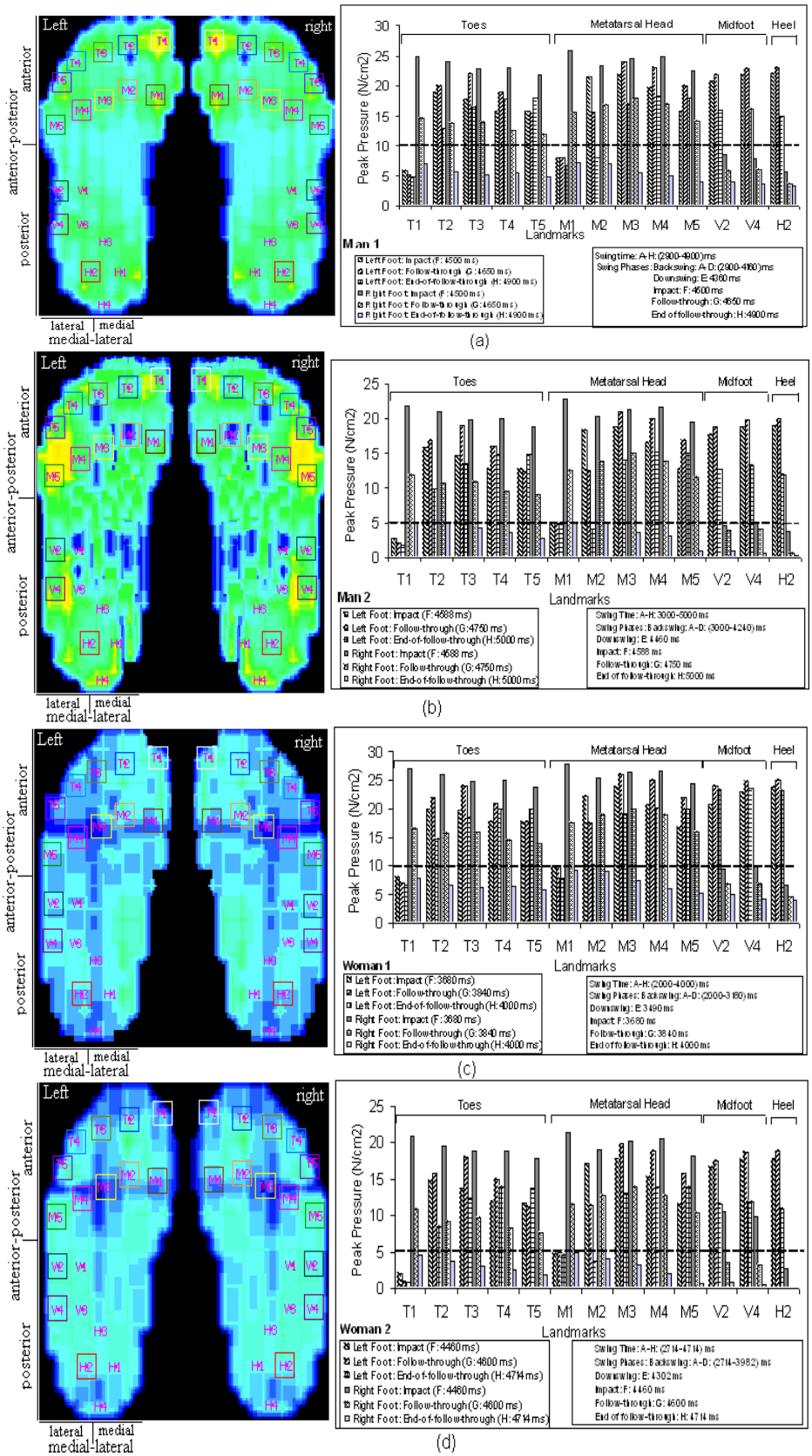

Figure 4. The pressure screen (2D views) and peak pressures under both feet over landmarks: (a) for man (1), (b) for man (2), (c) for woman (1), and (d) for woman (2).

4. DISCUSSIONS

4.1. Peak pressures effect

In the left feet for men (1 &2), during the impact (fig. 4a: 4500 ms & fig. 4b: 4588 ms), the highest pressure is changing in a decreasing order in the regions of the H2 (lateral heel), M3 (3^{rd} metatarsal head), V4 (midfoot lateral, M2 (2^{nd} metatarsal head), V2 (midfoot lateral), M4 (4^{th} metatarsal head), T2-T5 (2^{nd}-5^{th} toes), and M5 (5^{th} metatarsal head). During the follow-through (fig. 4a: 4650 ms & fig. 4b: 4750 ms), the peak pressure is changing in a decreasing order in the regions of the M3 (3rd metatarsal head), M4 (4th metatarsal head), H2 (lateral heel), V4 (midfoot lateral), T3 (3rd toe), V2 (midfoot lateral), M5 (5th metatarsal head), T2 (2nd toe), T4 (4th toe), M2 (2nd metatarsal head), and T5 (5th toe). At the end of follow-through (fig. 4a: 4650 ms & fig. 4b: 4750 ms), the peak pressure is under the M4 (4th metatarsal head), followed by low pressure under the M5 (5th metatarsal head), T5 (5th toe), T4 (4th toe), M3 (3rd metatarsal head), T3 (3rd toe), V4 (midfoot lateral), V2 (midfoot lateral), H2 (lateral heel), and T2 (2nd toe) regions. Oppositely, in the right feet for men (1& 2), during the impact (fig. 4a: 4500 ms & fig. 4b: 4588 ms), the highest pressure is observed under the M1, T1, M4, M3, T2, M2, T4, T3, M5, and T5 respectively. During the follow-through (fig. 4a: 4650 ms & fig. 4b: 4750 ms), the peak pressure is changing in a decreasing order in the regions of the M3, M4, M2, M1, T1, M5, T3, T2, T4 , and T5. At the end of follow-through (fig. 4a: 4650 ms & fig. 4b: 4750 ms), the pressures under the heel (H1-H4), midfoot (V1-V4), metatarsal heads (M1-M5), and toes (T1-T5) are low (less than 10 N/cm2 for man 1 and less than 5 N/cm2 for man 2).

On the other hand, In the left feet for women (1 & 2), during the impact (fig. 4c: 3680 ms & fig. 4d: 4460 ms), the highest pressure is changing in a decreasing order in the regions of the H2, M3, V4, M2, V2, M4, T2-T5, and M5. During the follow-through (fig. 4c: 3840 ms & fig. 4d: 4600 ms), the peak pressure is changing in a decreasing order in the regions of the M3, M4, H2, V4, T3, V2, M5, T2, T4, M2, and T5. At the end of follow-through (fig. 4c: 4000 ms & fig. 4d: 4714 ms), the peak pressure is under the M4, followed by low pressure under the M5, T5, T4, M3, T3, V4, V2, H2, and T2 regions. Oppositely, in the right feet for women (1& 2), during the impact (fig. 4c: 3680 ms & fig. 4d: 4460 ms), the highest pressure is observed under the M1, T1, M4, M3, T2, M2, T4, T3, M5, and T5, respectively. During the follow-through (fig. 4c: 3840 ms & fig. 4d: 4600 ms), the peak pressure is changing in a decreasing order in the regions of the M3, M4, M2, M1, T1, M5, T3, T2, T4, and T5. At the end of follow-through (fig. 4c: 4000 ms & fig. 4d: 4714 ms), the pressures under the heel (H1-H4), midfoot (V1-V4), metatarsal heads (M1-M5), and toes (T1-T5) are below 10 N/cm2 for woman 1 and 5 N/cm2 for woman 2.

4.2. COP effect

COPx (medio-lateral) and COPy (antero-posterior) are used as an indicator of stability [7, 9]. In figure 3, COP is represented as a length in cm. In the graphical representation of the COP (fig. 3a, 3b, 3c & 3d), it is clear that there is a non-cyclic and asymmetric movement between both feet. Besides, for all subjects, COPx (medial-lateral) and COPy (anterior-posterior) were mostly observed in the left foot comparing to the right one. During the time of impact (F: fig. 3a, 3b, 3c & 3d) it has been noticed that, under the right foot, COPx for women was larger than COPx for men, while the COPy for men was larger than the COPy for women. On the other hand, for the left foot case during the follow-through (G-H: fig. 3a, 3b, 3c & 3d), both COPx and COPy for women were much higher than those for men.

4.3. Design Insoles

According to swing phases (impact, follow-through, and end of follow-through), the insoles of the right feet should be designed so that it is provided with a better ability to rock in the regions (M1, M2, M3, M4, and M5) of the metatarsal joints. The toe parts (T1, T2, T3, T4, and T5) should be also considered based on the peak pressures. As a result, only the anterior part of the right foot in the medial-lateral direction can be considered for designing the right feet insoles. On the other hand, the insoles of the left feet should be designed in the lateral regions (H2, V2, V4, M2, M3, M4, M5, T2, T3, T4, and T5) based on the peak pressures. This means that the left feet insoles should be designed in a lateral side in the anterior-posterior direction. This will support the end position of the left feet on its lateral edge to provide wider contact surface. In this connection, Williams and Cavanaugh [10] suggested to rearrangement of the spikes in the outsole by considering the pressures and COP results.

5. CONCLUSION

An asymmetrical design should be considered between the left and the right insoles due to asymmetrical movement of the two feet during the golf swing. The present study shows that during the golf swing, the design for left insole would be more prior than right one. The left insole should be designed under heel, midfoot, metatarsal head, and toe regions laterally, while for the right insole, the design should be in the metatarsal head and toe regions based on the peak pressures. So for the golf shoe, the insoles design should be constructed to reduce the foot pressure and to improve the desired aspects of the swing during the golf swing.

REFERENCES

[1] Budney, D.R. & Bellow, D.G. Kinetic analysis of a golf swing. *Research Quarterly*, 50(Suppl. 2) (1979), pp.171-179.

[2] Carlsoo, S. Kinetic analysis of the golf swing. *Journal of Sports Medicine and Physical Fitness*, 7 (1967), pp.76–82.

[3] Cooper, J. R., et al. kinematic and kinetic analysis of the golf swing. In R.C. Nelson & C.A. Morehouse (Eds.), *Biomechanics IV*. Baltimore: University Park Press, (1974), pp. 298-305.

[4] Cordero, A.F., et al. Use of pressure insoles to calculate the complete ground reaction forces. *Journal of Biomechanics*, 37 (2004), pp.1427–1432.

[5] Holt, R. & Mason, T. *Sport in Britain 1945–2000*. Oxford: Blackwell Publishers Ltd, 2000.

[6] Han, T.R., et al. Quantification of the path of center of pressure (COP) using an F-scan in-shoe transducer. *Gait and posture*, 10(Suppl. 3) (1999), pp. 248-254.

[7] Hof, A.L., et al. The condition for dynamic stability. *Journal of Biomechanics*, 38(2005), 1-8.

[8] Neal, R.J. & Wilson, B.D. 3D kinematics and kinetics of the golf swing. *International Journal of Sport Biomechanics*, 1(Suppl. 3) (1985), pp. 221-232.

[9] Prieto, T.E., et al. Measures of postural steadiness: differences between healthy young and elderly adults. *IEEE Transactions on Biomedical Engineering*, 43 (1996), pp. 956-966.

[10] Williams, K.R. & Cavanagh, P.R. The mechanics of foot action during the golf swing and implications for shoe design. *Medicine and Science in Sports and Exercise*, 15 (Suppl. 3) (1983), pp. 247-255.

Proceedings of the 4th BSME-ASME International Conference on Thermal Engineering
27-29 December, 2008, Dhaka, Bangladesh

EXPERIMENTAL INVESTIGATION OF LIFT TO DRAG RATIO BETWEEN VOLUMETRICALLY EQUIVALENT FUSELAGES.

Mohammad Mainuddin and M. A Taher Ali
Department of Mechanical Engineering
Bangladesh University of Engineering & Technology (BUET)
Dhaka-1000, Bangladesh
E-mail: mainuddin@me.buet.ac.bd

ABSTRACT

To improve the overall lift to drag a new concept on fuselage of an Unmanned Aerial Vehicle (UAV) is investigated where the fuselage along with the wings contribute to certain percentage of lift. To investigate the improvement of lift to drag two fuselages are considered, one is conventional cylindrical shaped and the other is aerofoil shaped. Two fuselage models with a scale of 1:32 one with aerofoil cross-section and other with conventional cylindrical cross section is manufactured such that both the models have the same volume. Same set of wings is used in both the models so that the results show the comparison between the two types of fuselage. To reduce the induced drag, winglets are used in aerofoil shaped fuselage and then all the three fuselages i,e circular shaped, aerofoil shaped and aerofoil shaped with winglets are placed in a wind tunnel to measure the lifts and drags with the help of two component balance specially made for the purpose. Measurements are taken for different angles of attack of the fuselages to find the overall lift drag response characteristics.

Keywords: *UAV, Equivalent fuselage, Aerofoiled fuselage, Wingleted fuselage.*

1. INTRODUCTION

In early 20th century a famous professional aircraft designer Vincent Justus Burnelli [1] developed the concept of all body lifting aircraft where he used fuselages of aerofoil cross section. But this fuselage aerofoil section had to be sufficiently thick such that man could ride in it. So the scientific community had raised a number of technical concerns related to the large fuselage and its impact on aerodynamics. Amongst these primary concerns was the negative aerodynamic drag effects attributed to the lifting-body fuselage due the increased fuselage frontal area and the fuselage wing interference. An analysis of the concept performed by Wertenson [2, 3] in 1931 showed that the Burnelli's design concept resulted in less frontal area than a conventional twin-engine transport airplane and that the negative fuselage wing interference is more than compensated by the increased lift of the fuselage. Subsequent analysis performed at this time by some researchers [4, 5, 6, 7] also supported the findings of Wertenson. It is important to note

that Burnelli was not alone in the development of all-lifting vehicle technology, there were more than fifty all-lifting aircraft developed during the last century [1, 8]. But all of these aircraft were designed for large carrying capacity. But now-a-days small Unmanned Aerial Vehicle (UAV) concepts are developed and this UAV does not require thicker fuselage besides it uses sophisticated electronic elements that are small in size but weighty. So UAV requires higher lifting force with a smaller size. National Aeronautics Space Administration's (NASA) X-39, X-43B, X-45A and all Unmanned Combat Aerial vehicle (UCAV) also uses all-lifting body fuselage but all of these are designed for high-speed transport under Future Aircraft Technology Enhancements (FATE) program [9,10].

As some of the UAV have to operate in the speed of 50km/hr to 100km/hr, the present investigation is carried out in this speed range. Further the design of nature and the practical aspects of streamline form may be studied from the bodies of fishes and birds, the profiles of which have been gradually meet the requirements of least resistance for motion through a fluid, water or air, as the case may be [11]. In this context the gliding bird's body shape could be a good natural example for a UAV design and for most of the gliding birds like Harris' hawk (Parabuteo unicinctus) have aerofoil body shape rather than conventional cylindrical shape [12]. Again on fly birds continuously change their feathers position to improve their maneuvering capability with minimum energy loss. For example the feathers at the wing tips of most birds that soar over land separate both horizontally and vertically in flight to form slotted tips. The individual feathers in the slotted tips resemble the winglets used on the wing tips of some aircraft to reduce induced drag.
In this experimental test we introduce aerofoil fuselage to produce some lift from the fuselages but this finite width aerofoiled fuselages also generate induced drag due to tip vortices that ultimately reduce the overall lift to drag. So we incorporate winglets at both sides of the fuselage to reduce the induced drag.

2. EXPERIMENTAL DETAIL

The experiment is carried out in a 700mm×700mm closed circuit wind tunnel as shown in fig.1. The wind speed is created by the two 700mm counter rotating woods aerofoil (U.K.) fans. To minimize transmission of vibration generated in the fans unit, to the rest of the wind tunnel it is mounted in a separated heavy foundation and is connected with the wind tunnel by vibration isolator made of heavy canvas cloth. At the discharge of the fans there is a silencer to reduce the sound level. From the silencer air flow passes through the flow controlling butterfly valve, diffuser and the plenum chamber to stabilize the flow to certain level. Air from the plenum chamber passes over the cooling coil and through the air filter before entering the parabolic contraction cone. In the contraction cone the dimension is reduced from 1525mm×1525mm to 700mm×700mm. at the delivery of the contraction cone where there is a honey comb flow strainer to straighten out any flow diversity and break down any large eddy before entering into the test section. From that the air flow goes back to the fan unit through the return duct. The fan motors are powered by 400V-3Φ-50Hz power supply through motor speed controller. Thus the wind speed in the tunnel can be varied both by controlling the fan motor speed as well as by controlling the butterfly valve.

To facilitate the present experiment in the open air condition the diffuser at the end of the test section is taken out and the discharge side of the test section is fitted with a 700mm×700mm discharge duct and a 1000mm×1000mm to 762mm×762mm bell mouth entry is added at the return duct to have smooth entry. Thus the 406mm open flow field created between the discharge duct and bell mouth entry become the experimental space where desire velocity is obtained.

The two components spring balance system (fig-2) specially made for the experiment is mounted on a support frame and is placed in the experimental space. The balance is such that fuselage models can be mounted on the holding bar which is supported by springs and is guided by bearings so that by the action of the lift force it can move up against the spring force with negligible friction. The holding bar is held in the vertical position by a horizontal drag force balancing spring system mounted on the same support frame. When the drag force deviate the holding bar from the vertical position then by adjusting the drag spring the bar can be push back to its vertical position and both the drag force and the lift force found simultaneously can be determined from the deflection of the springs.

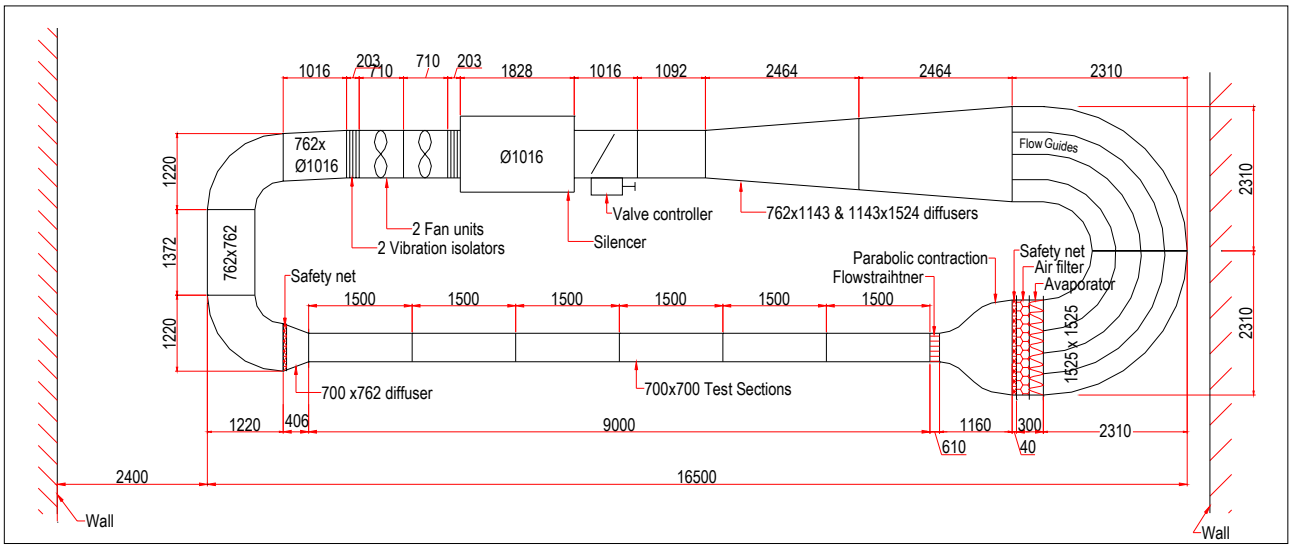

Figure 1: 700mm × 700mm closed circuit Wind Tunnel

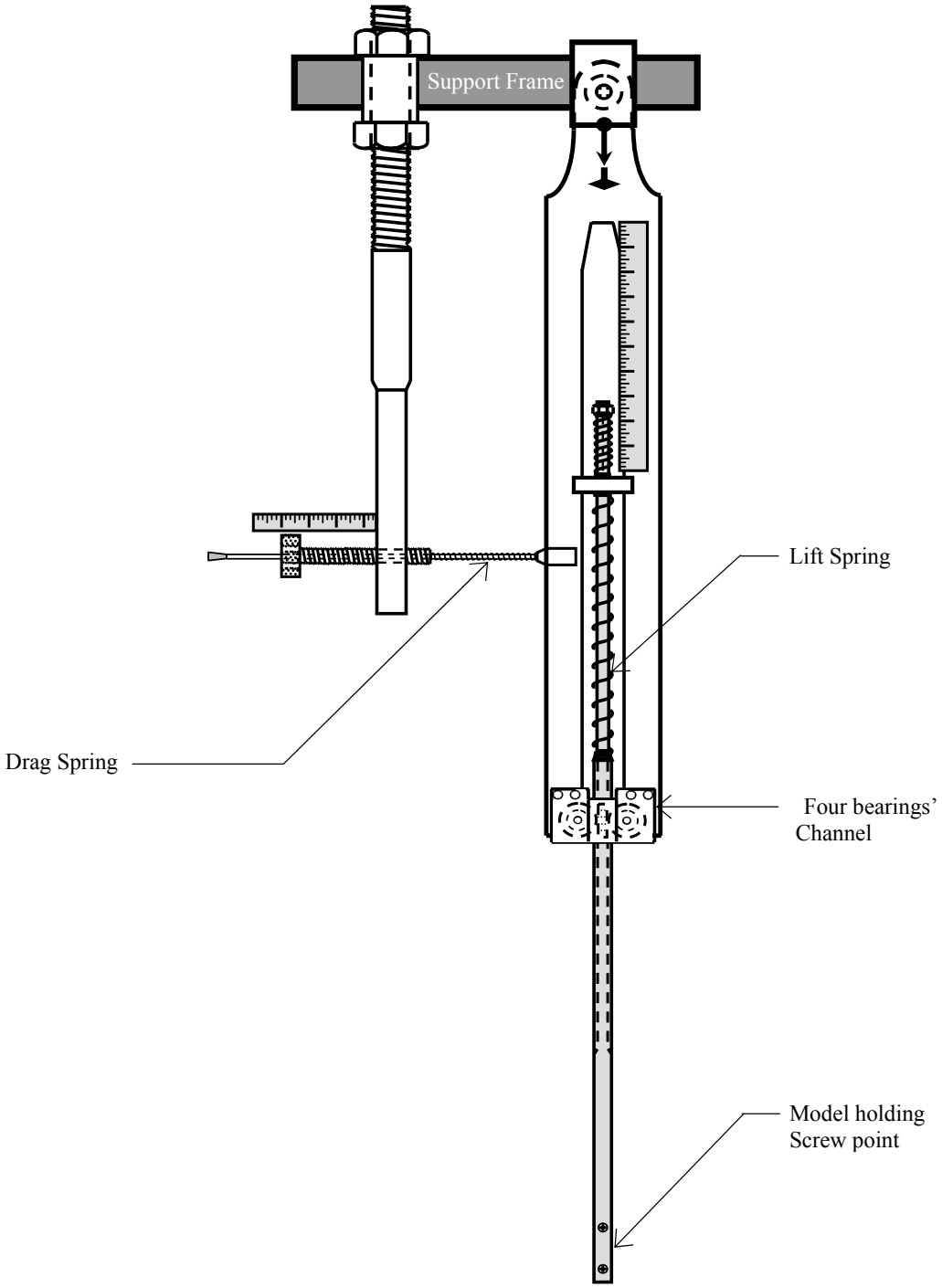

Figure 2: Spring balance system to measure the lift and drag simultaneously.

A number of 1:32 scale fuselages models both with aerofoil cross-section as well as conventional cylindrical cross section are manufactured such that both the type of models have the same volume.

The circular fuselage model has a total length of 274 mm with 44 mm long nose section, 70 mm long tail section and 160 mm long circular body with a diameter of 50 mm. Its sectional views are shown in figure 3.

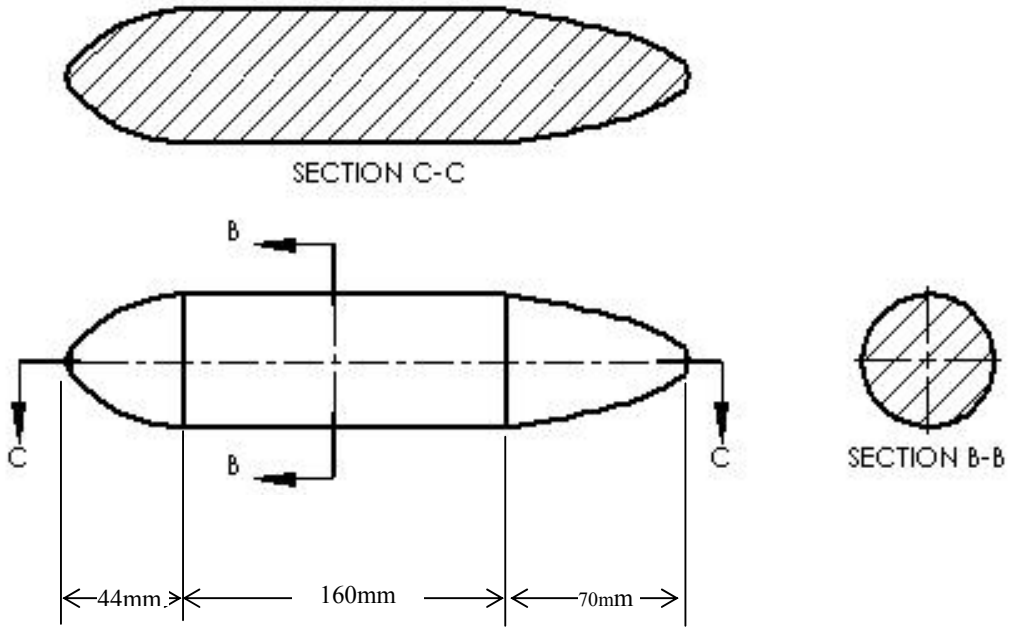

Figure 3: Cross section of the circular fuselage

It is found that **NACA** 4 digit aerofoil section is suitable for low speed aircraft so in this investigation **NACA 2412** cambered aerofoil section is used for both the fuselage as well as for the wings but of different cord length and span. For fuselage its cord length is 238mm and the span is 100mm so that the total volume would be same as circular fuselage i,e 438400 mm^3. The common wings which are used for both the fuselages have its cord length 80mm and total span 400mm. Figure 4 shows the **NACA 2412** cambered aerofoil section.

Figure 4: NACA 2412 cambered aerofoil section

3. EXPERIMENTAL PROCEDURE

At first the models with its force balance system are placed in the experimental space of 700mm × 700mm wind tunnel as described above. These arrangements are made to get the desired wind speed at atmospheric pressure. Then the tunnel is started and the air velocity is

gradually increased with the help of a frequency changing knob of the frequency inverter. An 8mm diameter and 750mm long pitot static tube of CASELLA LONDON (U.K.) is placed in the test section and is connected to a digital pressure/velocity transducer of Furness Control Ltd. (U.K.) to monitor the air velocity.

For spring balance system at any air speed the drag spring have to adjust in such a way that the rectangular stem remains vertical. This is a balanced condition of the system. At this position the deflection of the horizontal spring provides the drag force and the deflection of the vertical spring provides the lift force.

There are two springs in the vertical stem. The small spring provides the lift until the lift overcomes the model self weight. When the smaller spring expands fully the long spring began to compress. Then the long spring force combine with model self weight give the actual lift.

The experiment is carried out for different angles of attack of the fuselages and the wings at different air speeds.

4. RESULT AND DISCUSSION

For all the three models the angle of attack of the fuselage (θf) are fixed at 4^o and the relative angles between wings and fuselage (θw) are set at 2^o and for different air speed the respective lift and drag are forces are recorded.

The lifts, drags and the lift to drag ratios for all the three models are plotted. To compare amongst the model performance the variation of lifts for all the models are drawn in a single graph. Similarly the variation of drags and L/D's are also drawn separately in single graphs as shown in figures 5, 6 & 7 for fuselage angle of attack θf = 4^o and θw = 2^o.

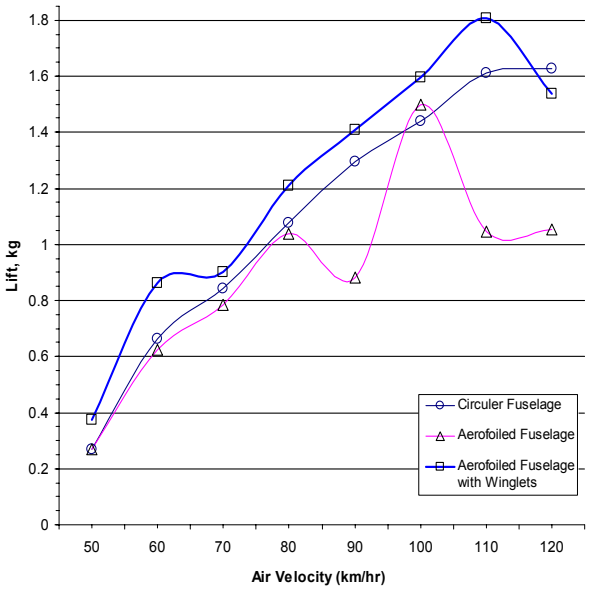

Figure 5: Lift vs. Velocity curves for θf = 4, θw = 2

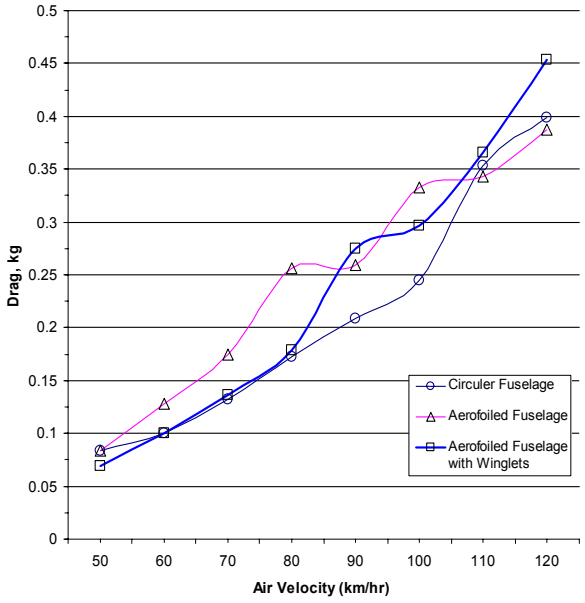

Figure 6: Drag vs. Velocity curves for θf = 4, θw = 2

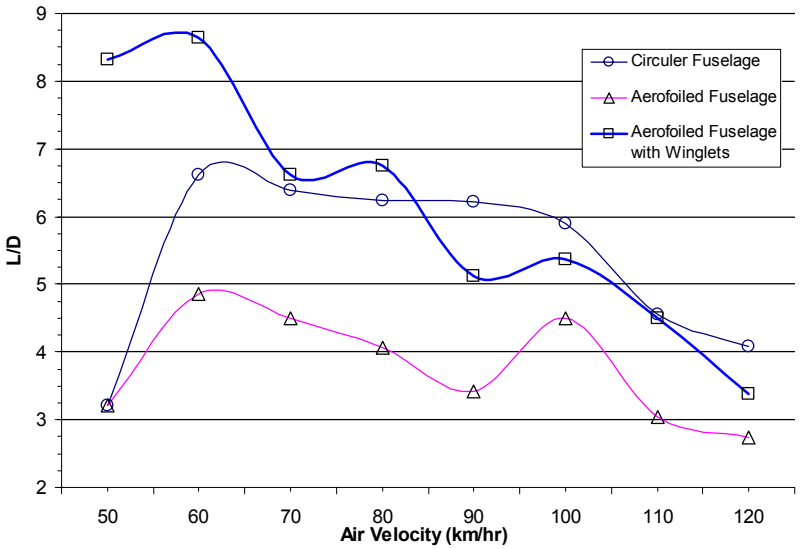

Figure 7: L/D vs. Velocity curves for θf = 4, θw = 2

In figure 5 it is seen that for θf = 4^o and θw = 2^o setting both the circular and aerofoiled fuselages produce approximately the same lift force up to 80 km/hr air speed. At air speed between 80 and 100 km/hr the lift force of the aerofoiled fuselage decreases due to some unwanted instability which creates flow separation on its upper tail side. As the flow reattachment occurs at 100 km/hr air speed the lift force increases to its normal expected value and then again decreases indicating the permanent flow separation near the top tail end of the fuselage. By adding winglets at the aerofoiled fuselage the lift forces increases by approximately 10%. The winglets reduce the flow instability thereby preventing the early flow separation. The nature of lift curves of all the fuselages show the clear indication of flow separation occurring at around 100 km/hr airspeed.

Figure 6 shows the increase of drag force with the air speed. At lower speed both the circular fuselage and the wingleted-aerofoiled fuselage has the same drag and both have a value lower than the drag produced by aerofoiled fuselage. But at higher velocities the total drag for circular fuselage again increases due to higher profile drag at high air speed.

It is found in figure7 that lift to drag ratio for aerofoiled fuselage is much lower than circular fuselage if there are no winglets. But using winglets in the aerofoiled fuselage shows a higher lift to drag ratio.

So after analyzing all the graphs it is found that aero-foiled fuselages with winglets provided maximum lift with respect to drag.

5. CONCLUSIONS

Although aerofoiled fuselages have to greater lift over circular fuselage but due to induced drag in aerofoil fuselages overall lift to drag reduces.

But if the induced drag is checked by winglet then a greater improvement of the overall lift to drag is achieved.

REFERENCES

[1] Wood R. M., "The Contributions of Vincent Justus Burnelli" AIAA 2003-0292, Jun. 2003.
[2] Wertenson, I. F., "Investigation of the Burnelli Type Airplane" Jan. 1931.
[3] Wertenson, I. F., "Investigation into the Development of The Burnelli Type Airplane" Aero Digest, March 1931.
[4] Wertenson, F., "The Economical Cruising Speed of the Burnelli All-Wing Monoplane Flight" Aug. 24, 1933, pp. 854-856.
[5] Klemin, A., "All-Wing Lifting Fuselage, Scientific America" April 1935.
[6] Burnelli Model UB-14 14-Passenger Transport Aero Digest, August 1935.
[7] Watter, M. "The Burnelli Airfoil Body. Flight" The Aircraft Engineer, Sept 26, 1935.
[8] Wood, R. M. and Bauer, S. X. S. "Flying Wings/Flying Fuselages" AIAA 2001-0311, Jan. 8-11, 2001.
[9] http://www1.msfc.nasa.gov/NEWSROOM/news/releases/2002/02-182.html, November 2002.
[10] Jenkins D. R., Landis T., and Miller J., "American X-Vehicles, An Inventory—X-1 to X-50, Centennial of Flight Edition, Monographs in Aerospace" History No. 31, SP-2003-4531, June 2003.
[11] Hansen J. R., Kinney J., "Taylor D. B., Prickett M., and Lee J. L., The Wind and Beyond, A Documentary Journey into the History of Aerodynamics in America" Volume II: Reinventing the Airplane June 2000.
[12] Tucker V. A., "Gliding Birds: Reduction of Induced Drag by Wing Tip Slots Between the Primary Feathers" Department of Zoology, Duke University, Durham, NC 27706, USA, Accepted 5 March 1993.

APPENDIX

For convenience the following symbols are used in all the data tables:

Θf => Fuselage angle of attack in degree

Θw => Relative angle between wing and fuselage

So, actual wing angle of attack is **(Θf +Θw)** degree

L => Lift force in kg, **D** => Drag force in kg

L/D => Lift to Drag ratio.

Proceedings of the 4th BSME-ASME International Conference on Thermal Engineering
27-29 December, 2008, Dhaka, Bangladesh

CONSTRUCTAL PATTERN FORMATION OF A FLUID NETWORK: A PRELIMINARY INVESTIGATION

A. K. Das[1], P. K. Das[1] and G. Das[2]

[1]Department of Mechanical Engineering, Indian Institute of Technology, Kharagpur- 721302, India
[2]Department of Chemical Engineering, Indian Institute of Technology, Kharagpur- 721302, India
Phone: 03222-282916, Fax: 03222-282278, Email: arup@mech.iitkgp.ernet.in

ABSTRACT

Network based constructal fluid pattern is formed using stochastic brunching of flow channel experimentally. The network is self similar and fractal in nature. Fractal scaling is used for the parameterization of the branches and different generations. It has been observed that spatial ranges of different generations are almost segregated and not coupled with each other. Moreover, span of region is magnified as the hierarchy of the network increases. Efforts have also been made to determine a fractal dimension of the network.

Key words: *Flow network, Fractal scaling, Generation, Constructal*

1. INTRODUCTION

Natural river basin is irregular in nature and shows lots of wiggle-waggle down the valley. As per rule river will follow the shortest route and meet with sea under the attraction of gravity. But in actual case formation of brunch river and side river make a net like structure in the basin. It resembles various self similar structures in nature like roots, stems and leaves in plants, arteries network in animal bodies etc. Study of river morphology is becoming popular and essential for determination of various important hydrological factors like width ratio, expenditure energy, initiation function and rainfall field.

In 1932 Horton [1] first characterized the river network and tried to identify the consequences of brunching of a river. He proposed a hierarchical classification of the brunches which was later developed by Strahler [2]. Topological randomness of the river network and statistical independence of interior and exterior link have been pointed out by Shreve [3]. Terminologies like bifurcation ratio, length ratio and area ratio in the context of river network was first identified by La Barbera and Rosso [4]. They also suggested that such ratios are constants for a particular river network irrespective of its length scale. Later on, various researchers [5-7] suggested that bifurcation ratio is equal or more than the dimension of the Euclidian space. As a result it appears that river network is an area filling phenomena.

Fractal geometry has also been used by Rodríguez-Iturbe and Rinaldo [8] for the prediction of river morphology. As the methodology of fractal mechanics do not care the flow dynamics it can only be used as a descriptive tool rather than prediction of flow phenomena. With the introduction of constructal theory by Bejan [9] various theories of minimum energy dissipation rate, minimum stream power and maximum transportation capacity has been proposed. A well written review of the above methodologies has been presented by Huang and Nanson [10]. Recently Molner [11] proposed a geometrical scaling for the river network taking care about the probability of termination, continuation and brunching of stream. Constructal

theory has been used [12] for scaling of river brunching minimizing the overall resistance to flow. De Bartolo et al. [13] proposed a generalized dimension of river network which approaches the envelopes of the spectra of side brunching corresponding to different hortonian [1] stream order.

In the present paper we have experimentally created one reverse fluid stream network in order to study the fractral dimensions and average area of brunch formation of different levels. In the downstream fluid channels are merged to form upper level streams and subsequently fuse into a single stream. From the photographic view of the system Image Pro Plus software is used to measure the brunch length of various levels. Fractral dimensions are calculated from the individual stream lengths and positions of junctions are determined for identification of influence area per level. In the next section experimental details are mentioned. Results obtained from the experiment and investigation towards fractal dimension is reported later on. Finally important conclusions are mentioned which states the significance of the present work.

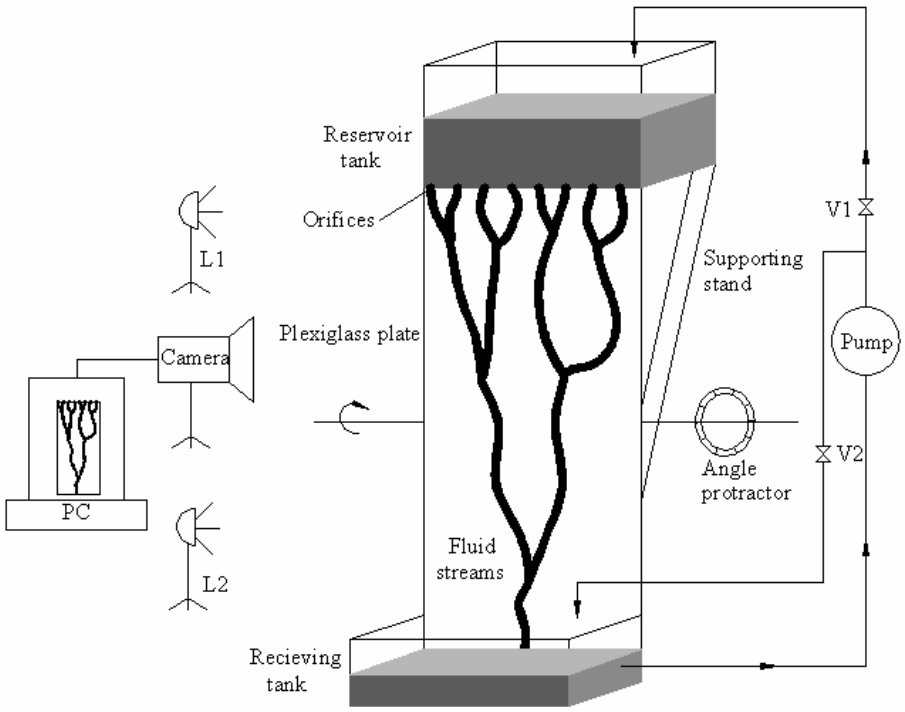

Fig.1 Schematic diagram of the experimental facility

2. EXPERIMENTAL FACILITY

The setup as shown in fig. 1 consists of in three parts. At the top one 130X90X50mm reservoir tank is kept filled with distilled water. For better visualization red pigment is mixed with water in the reservoir. Water is then allowed to flow through a number of submerged circular orifices having diameter of 1 mm. After flowing through the orifices, water jet will fall over a smooth polished plexiglass sheet (observation plate) having 400 mm length, 150 mm width and 4 mm thickness. 5 mm high rim is also placed around the observation plate to resist the splashing of the get. Reservoir over the observation plate is held firmly with support. One tilting arrangement is also attached with the support in order to allow the jet to fall over the plate. Fluid streams originating from the orifices will merge with each other over the observation plate

and is collected in the receiving tank. Fluid accumulated at the receiving tank is again pumped in the reservoir tank to maintain a fixed fluid level there. Blotting paper is used to suck the occasional appearance of liquid drop over the plate before the start of streaming of fluid jet.

Initially the orifices are blocked using wax and the reservoir tank is filled with dyed water. Then the blockages of selected orifices are opened and the fluid is allowed to stream through it. The whole system is then rotated along the horizontal axis to a little bit (5°-10°) which allows the jet to fall over the observation plate and flow through it. One angle protractor is attached with set up from which rough estimate of the angle of tilt can be made. A height measuring scale is attached along with the reservoir tank. A constant height of the fluid level is maintained by running the pump at a certain opening of discharge. Valve V1 and V2 is manipulated simultaneously in order to do so. Outlet of the pump is attached with the side wall of the reservoir tank to minimize the turbulence in the reservoir due to impingement of jet.

A digital camera (Sony Cyber-shot) with a low frame rate of 20 shots/sec was used to record the images of the network of the fluid streams with proper lighting (L1 and L2). Special care has been taken to maintain almost uniform illumination of the observation plate. Camera is connected with a dedicated pc which saves and analyzes the captured figures. Software Image Pro Plus (Version 6.3) is used to get the intricate details of the frames.

3. RESULTS AND DISCUSSIONS:

For a fixed height of the reservoir liquid level jet Reynolds number (Re_j) is calculated using the orifice diameter (d_o) as the characteristics length. The relation is as follows:

$$\mathrm{Re}_j = \frac{\rho_w U_j d_o}{\mu_w} \tag{1}$$

where,

$$U_j = \sqrt{2g\cos\theta H_r} \tag{2}$$

In the above expressions, ρ_w is the density of water and μ_w is the viscosity of the water. U_j is the jet velocity which is dependent over gravitational acceleration g, angle of tilt θ and height of the liquid pool at the reservoir tank H_r.

Fig.2 Photographic view of the fluid stream network at a Reynolds number 1900-2000

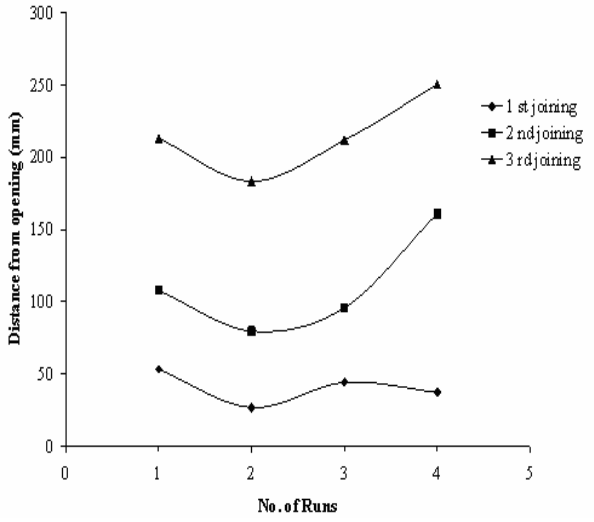

Fig.3 Axial locations of different levels of joining for various run

One specimen of the captured frame is shown in fig. 2. In the figure 16 orifices are opened at a constant interval among them. Flow Reynolds number is around 1900-2000 for fig. 2. It can be seen that adjacent first order stream is joined with each other to form 8 2nd order streams. These second order streams are again joined with adjacent stream to form 4 3rd order streams. 3rd order streams are merged to form 2 4th order streams and finally one 5th order stream is formed. It can also be noticed that the stream depth is increasing at the downstream. From the plane of the orifices first junction is almost equidistant. Similarly, all the junctions have particular region for merging. The phenomenon is stable but not repetitive. For the same Reynolds number the network looks different from run to run. But the average location of junction remains more or less same. Investigation has also been made to identify the distance of the junction from the orifices. Fig. 3 depicts the axial locations of the junctions for four different runs of same Re.

It can be seen from the figure that location of the junctions never intersects with each other. It can also be noticed that length required for junctions increases as the level increases. Then we have tried to characterize the generated network based on Tokunaga [14] taxonomy. Fig. 4 shows the arrangement of the nomenclature for an arbitrary fluid stream network.

The streams ejecting from the orifice are named as 11. When two first order streams (11) are joined a second order stream (22) is formed. In the absence of any side brunching in the present network no stream of name 12, 13, 14, 23, 24, 34 are formed. Continuing like this, a stream 33 is formed after joining two second order (22) stream. Finally stream 44 is developed after merging of two third order stream (33). Total number of each stream order (N_{ij}) is shown in the upper triangular matrix of fig. 4. Summation of all brunches of the same order (N_i) is also shown in the matrix as per the following rule.

$$N_i = \sum_{for\ all\ j} N_{ij} \tag{3}$$

Horton's [1] bifurcation ratio (R_B) which is defined below is calculated.

$$R_B = \frac{N_i}{N_{i+1}} \tag{4}$$

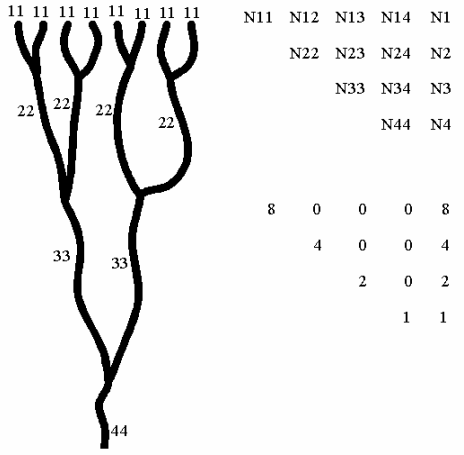

Fig.4 Nomenclature of the river network as per Tokunaga taxonomy

Fig. 2 has been studied in this respect and R_B turn out to be 2.0. Similarly effort has also been made to calculate Horton's [1] ratio (R_L) of channel length (L_i). It can be defined as follows:

$$R_L = \frac{L_i}{L_{i+1}} \tag{5}$$

Table.1 Lengths of different streams as measured from software Image Pro Plus 6.3

$L1_1$	33.9	$L2_1$	22.3	$L3_1$	166.3	$L4_1$	100.6
$L1_2$	45.8						
$L1_3$	44.8	$L2_2$	21.0				
$L1_4$	41.0						
$L1_5$	45.2	$L2_3$	94.7	$L3_2$	106.2		
$L1_6$	48.5						
$L1_7$	63.2	$L2_4$	59.5				
$L1_8$	66.8						
$L1_9$	32.2	$L2_5$	80.1	$L3_3$	120.7	$L4_2$	139.1
$L1_{10}$	37.3						
$L1_{11}$	15.6	$L2_6$	82.9				
$L1_{12}$	17.5						
$L1_{13}$	70.3	$L2_7$	106.4	$L3_4$	52.5		
$L1_{14}$	74.9						
$L1_{15}$	80.7	$L2_8$	91.4				
$L1_{16}$	86.0						
$\Sigma L1_i/n$	50.2	$\Sigma L2_i/n$	69.8	$\Sigma L3_i/n$	111.4	$\Sigma L4_i/n$	119.9
R_{L1}	1.39	R_{L2}	1.59	R_{L3}	1.076		
R_L	1.35						

Tab. 1 states the lengths of the curvilinear path of the streams of different order which is measured using software Image Pro Plus (Version 6.3). Calculated R_L for three different levels as well as their average is depicted in the table. Average channel length ratio turn out to be 1.35. The fractal dimension (D) for the channel network can be expressed in terms of brunching and length order ratio as follows:

$$D = \frac{\log(R_B)}{\log(R_L)} \tag{6}$$

For the present case (fig. 2) where Reynolds number is around 1900-2000, fractal dimension comes out to be 2.31. Fig. 5 shows the variation of fractal dimension for different Reynolds number. It is evident from the figure that fractal dimension increases as the liquid height in the reservoir tank increases. With the increase of Reynolds number chances of wiggle waggle decreases that causes the decrease of fractal dimension.

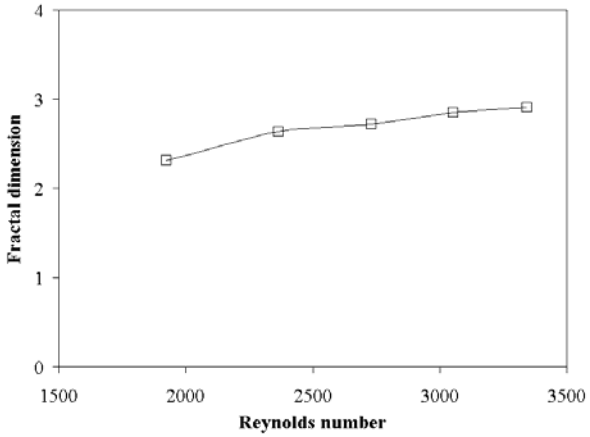

Fig.5 Variation of fractal dimension for different Reynolds number

4. CONCLUSION

The salient conclusions of the experimental investigation are stated below:

- A reverse fluid stream network is formed which shows fractal behavior in nature.
- Different levels of streams merge with each other to form higher order stream. The area of mergence is not colliding with each other. It shows different levels have their own area to roam around.
- To characterize the streams Tokunaga [14] taxonomy is used. Absence of side brunch makes the nomenclature simple and self descriptive.
- Horton's [1] bifurcation ratio and channel length ratio is calculated from the captured frame. Fractal dimension is also obtained using the above mentioned ratio which turns out to be less than 2. This shows the fluid stream network is not area filling phenomena.
- Variation of fractal dimension with Reynolds number shows that with the increase of Reynolds number the network tends towards area filling system.

REFERENCE

[1] Horton, R. E., Drainage basin characteristics, *Transactions of the American Geophysical Union,* 13 (1932), pp. 350–370.

[2] Strahler, A. N., Hypsometric (area-altitude) analysis of erosional topography, *Geological Society American Bulletin,* 63 (1952), pp. 1117–1142.

[3] Shreve, R. L., Infinite topologically random channel networks, *J. Geology,* 75 (1967), pp. 179-186.

[4] La Barbera, P., Rosso, R., Fractal geometry of river networks, *Transactions of the American Geophysical Union,* 68 (1987), pp. 12-76.

[5] Tarboton, D. G., Bras, R. L., Rodriguez-Iturbe, I., The fractal nature of river networks, *Water Resources Research*, 24 (1988), pp. 1317–1322.

[6] La Barbera, P., Rosso, R., On the fractal dimension of stream networks, *Water Resources Research,* 25 (1989), 4, pp. 735–741.

[7] Tarboton, D. G., Bras, R. L., Rodriguez-Iturbe, I., Comment on 'On the fractal dimension of stream networks' by P. La Barbera and R. Rosso, *Water Resources Research*, 26 (1990), pp. 2243–2244.

[8] Rodríguez-Iturbe, I., Rinaldo, A., Fractal River Basins, Cambridge University Press, New York, 1997.

[9] Bejan, A., Advanced Engineering Thermodynamics, Wiley, New York, 1997.

[10] Huang, H. Q., Nanson, G. C., Hydraulic geometry and maximum flow efficiency as products of the principle of least action, *Earth Surf. Process. Landf.*, 25 (2000), pp. 1–16.

[11] Molner, P., On geometrical scaling of cayley trees and river networks, *J. of Hydrology,* 322 (2006), pp. 199-210.

[12] Reis, A. H., Constructal view of scaling laws of river basins, *Geomorphology*, 78 (2006), pp. 201-206

[13] De Bartolo, S. G., Veltri, M., Primavera, M., Estimated generalized dimensions of river networks, *J. of Hydrology,* 322 (2006), pp. 181-191.

[14] Tokunaga, E., Consideration on the composition of drainage networks and their evolution, *Geog. Rep. Tokyo Metro.,* Univ., 13 (1978), pp. 1-27.

Proceedings of the 4th BSME-ASME International Conference on Thermal Engineering 27-29 December, 2008, Dhaka, Bangladesh

MODELING OF THE DEVELOPED FLEXIBLE SKIRT AIR-CUSHION TRACK VEHICLE MODEL

Altab Hossain[a, *], Ataur Rahman[b], A.K.M. Mohiuddin[b], A.K.M P Iqbal[a]

[a] Department of Mechanical Engineering, Faculty of Engineering, University Industry Selangor, Malaysia
[b] Department of Mechanical Engineering, International Islamic University Malaysia, Malaysia

ABSTRACT

This research work describes the mathematical model development and analysis of the flexible skirt air-cushion track vehicle model for the collection and transportation operation of oil palm fresh fruit bunches (FFB) on swamp peat terrain in Malaysia. The main criterion of this research work is to produce an economical design which possesses low bearing capacity (7kN/m^2) for the swamp peat terrain. The track mechanism is used as the driving system to overcome the motion resistance and the flexible skirt air cushion which is supported by the pressurized air is used to increase the floatation capacity of the vehicle. The design and analysis of the flexible skirt air-cushion track vehicle model have been done using Ds CATIA V5 version 16. Air-cushion is pressurized by using a compressor which is powered by a DC motor. The mathematical model and design parameter simulations of the flexible air-cushion track vehicle model for straight motion have been considered for this study.

Keywords: *Mathematical model - Bearing capacity - Motion resistance - Air-cushion.*

1. INTRODUCTION

The rapid growths of the oil palm industry are the present development in Malaysia, in terms of cultivated area and volume of production. Oil palm industry has become a major contributor to Malaysia's export earnings. Palm oil will become the leading oil in the world around the year 2016 and average annual production of palm oil in the country will reach to 15.4 million tones in the period of 2016-2020. Palm oil is expected to become the world's leading oil in the next decade. In view of the scarcity of land in peninsular Malaysia, the expansion of new planting of oil palm will be mainly in Sabah and Sarawak. In Sarawak, about 2.5 million ha are considered suitable for agricultural development, but they are mainly on hilly or steep terrain or peat swamps. The bearing capacity of the peat swamps in Sarawak is very low which 7 kN/m^2 is. While, the ground contact pressure of the pneumatic wheel vehicle and tracked vehicle without payload would not be less than 10 kN/m^2. It is not possible at all to develop a wheel or tracked vehicle for the collection-transportation operation of oil palm fresh fruit bunches (FFB) on the peat swamp in Malaysia. Therefore it is urgent need to develop a vehicle for the infield collection-transportation operation of the oil palm fresh fruit bunches on the peat swamp terrain.

* Corresponding author: *E-mail address:* altab75@unisel.edu.my; Tel: 60-0169128403

The infield collection-transportation operation accounts a major part of the labour employed in the oil palm cultivation in peat soil. This labour shortage in the plantation is likely to become a serious problem in the future in Malaysia if no concentrated efforts are being made to mechanize the FBB collection-transportation operation. Various forms of machine systems have been imported, modified and tested by the machine manufacturers, machine suppliers, plantation companies, research institutions, and universities to contribute in fulfilling the need for mechanizing the infield collection-transportation operation in peat terrain.

The super Crawler by Holy Drilling Machines Sdn. Bhd., a track machine having 1500 mm wider and 3000 mm ground contact length, was locally developed to work on soft terrain but it could not operate on peat terrain due to excessive surface shearing-off that severely affect its sinkage and finally reduces its tractive performance. The Peat Prototype tracked Tractor by Ooi [1], a track machine having 1560 mm wider and 3000 mm ground contact length wooden grouser tracks, was developed to work on peat terrain including areas with very high water table level. The problem associated with peat-Prototype Tracked tractor is that the machine is difficult to operate on the terrain during turning due to the highly rigidity of the track and too much vibrations. The FBB picker MRK-1 by Yahya, et. al, [2] was developed from MALTRAK to mechanize and automate the infield collection-transportation of FBB. The main problem with MALTRAK and FBB Picker MRK-1 was that the tracks of these machines could easily slip out from the traction wheels when machine were making turnings. The segmented Rubber track vehicle was developed based on the Sepang peat terrain bearing capacity of 17 kN/m^2 for the collection-transportation operation of FBB. Furthermore, from the field performance test on the different terrain in Sepang peat area it was found that the vehicle is quite suitable for Sepang peat terrain. But, this vehicle can't consider for the Sarawak and Sabah even after ballast change.

Many research works have been carried out and different types of prototypes have been introduced by [3-5]. They introduced a novel semi-tracked air-cushion vehicle for soft terrain. The main problem of the machine is that the cushion part always is kept-in-touch with the ground and it is guided by a rear centre wheel. A hybrid vehicle which combines air-cushion technology with a full-track driving mechanism has been proven to be an efficient solution for a heavy duty vehicle on the low bearing capacity peat swamp for all working conditions. It is possible to get the ground contact pressure of this vehicle even less than 7 kN/m^2. The study on the enhanced performance of the air-cushion track vehicle model which would provide the solution of collection and transportation operation of palm oil on low bearing capacity ($7kN/m^2$) swamp peat terrain is also given by incorporating the data simulations.

2. METHODOLOGY

The air-cushion track vehicle model is comprised mainly with full track system and air-cushion system, DC motors, a battery pack, and a compressor (Fig. 1). The full rubber track mechanism is used as driving system to overcome travelling resistance, and the air-cushion system as vehicle body to support vehicle partial weight. The pressure to the air-cushion is provided by a single compressor to support the partial vehicle weight. For tractive performance and motion resistance, mathematical model has been developed with considering the vehicle in straight motion with uniform ground pressure distribution (UGPD). The mathematical model is then used for optimizing the vehicle design parameters and simulating the vehicle tractive

performance. Based on vehicle mathematical model and theoretical analysis, flexible skirt air-cushion track vehicle model has been designed and developed.

Figure 1: Air cushion track vehicle model

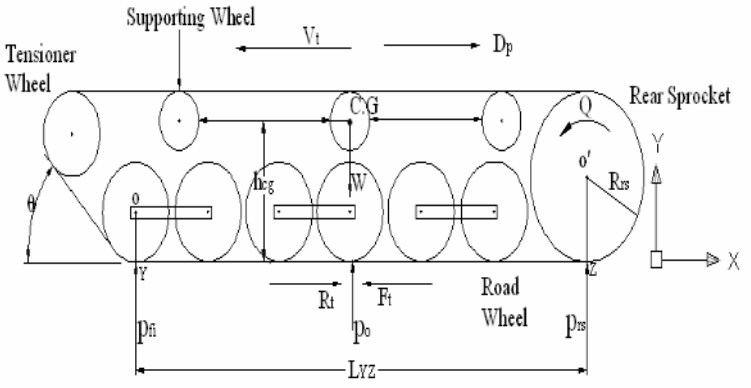

Figure 2: Force acting on driven belt of vehicle with UGPD

2.1 Mathematical Model Development

Mathematical model for the vehicle motion resistances and tractive performance computations are formulated by simplifying the mathematical models of the researcher [3-8] and made based on vehicle straight motion with uniform ground pressure distribution. The section of the track of front guider tensioned wheel and the end of the first road-wheel is set at 35° in order to overcome easily the front obstacles and climbing the 45° steep terrains as shown in Fig. 2.

The uniform ground pressure distribution (UGPD) over the track–terrain interface is done by locating the centre of gravity of the vehicle at the middle of the track ground contact length. The prime importance of this principle is to examine the vehicle mobility, which refers to the relative ease or difficulty of the vehicle to establish traverse motion over the unprepared peat terrain. The vehicle is considered with a rigid link segmented rubber track of total weight W, track ground contact length *L* and width *B*, grouser height *H*, rear sprocket R_{rs}, and road-wheel R_r, and height of the centre of gravity h_{cg}, vehicle constant speed of v_t, driving torque *Q* at the rear sprocket.

Sinkage

The sinkage of a tracked vehicle causes the power and traction loss. The vehicle performance is severely affected if the sinkage of the vehicle is more than or equal to the vehicle critical sinkage.

(i) For $0 \le z \le 5cm$: $z_1 = \dfrac{-\left(\dfrac{k_p D_h}{4m_m}\right) \pm \sqrt{\left[\left(\dfrac{k_p D_h}{4m_m}\right)^2 + \dfrac{D_h}{m_m} p_0\right]}}{2}$ with, $D_h = \dfrac{4BL}{2(L+B)}$, $p_0 = \dfrac{W}{A_t}$ (1)

(ii) For $z \ge 5cm$: $z_2 = \dfrac{-\left(\dfrac{k_p D_h}{4m_m}\right) \pm \sqrt{\left[\left(\dfrac{k_p D_h}{4m_m}\right)^2 + \dfrac{D_h}{m_m} p_0\right]}}{2}$ with, $D_h = \dfrac{4BL}{2(L+B)} + \dfrac{4A_c}{2(p_{ac})}$, $A_T = (A_t + A_c)$ (2)

where, p_0 is the normal pressure of the vehicle in kN/m^2 and z is the sinkage in m, m_m is the surface mat stiffness in kN/m^3, k_p is the underlying peat stiffness in kN/m^3, D_h is the hydraulic diameter in m, A_c is the air cushion area, A_t is the track area, W is the vehicle load, B and L are the width and ground contact length of the track in m, respectively and P_{ac} is the perimeter of the air cushion in m.

Traction Force

A tracked vehicle develops its tractive effort by deforming the soil in longitudinal shear. The tractive effort of the vehicle in this study is calculated in two ways.

(i) For $0 \le z \le 5cm$

$$F_b = A_t\left(c+\sigma\tan\varphi\right)\left[\frac{K_w}{iL}e^1-\left(1+\frac{K_w}{iL}\right)\exp\left(1-\frac{iL}{K_w}\right)\right] \quad \text{with } A_t = 2\left(B\times L_t\right),\ \sigma=\frac{W}{A_t},\ W=W_d+W_L+W_c \qquad (3)$$

where, F_b is tractive effort that develop at the bottom part of the track in kN and L is the ground contact part of the track in m, A_t is the area of the track ground contact length in m^2, σ is the vehicle normal stress kN/m^2, W is the total load of the vehicle in kN, W_d is the dry load of the vehicle, W_L is the track load of the vehicle, W_c is the air cushion load, c is the cohesiveness in kN/m^2, φ is the terrain internal friction angle in degree, K_w shear deformation modulus in m, i is the slippage of the vehicle in percentage.

(ii) For $z \ge 5cm$

$$F_{tc} = A_T\left(c+\sigma_{tc}\tan\varphi\right)\left[\frac{K_w}{iL}e^1-\left(1+\frac{K_w}{iL}\right)\exp\left(1-\frac{iL}{K_w}\right)+C_{sk}p_cA_c\right] \text{ with } \sigma_{tc}=\frac{W}{A_T} \text{ and } A_T = A_t + A_c \qquad (4)$$

where, F_{tc} is the tractive effort of the vehicle after the air-cushion touches the terrain in kN, C_{sk} is the coefficient of skirt contact drag, σ_{tc} is the vehicle normal stress after air-cushion touches the terrain in kN/m^2, p_c is the air pressure in the cushion in kN/m² and A_c is the cushion effective area in m^2.

Motion Resistance

The total motion resistance R_t which affects the vehicle differently for different values of sinkage.

(i) For $0 \le z \le 5cm$: $R_t = R_c + R_{in}$ (5)

(ii) For $z \ge 5cm$: $R_t = R_c + R_{in} + R_{sk}$ (6)

where, R_c is the motion resistance of the vehicle due to terrain compaction in kN, R_{in} is the vehicle rolling components internal frictional resistance, and R_{sk} is the skirt-ground interaction resistance in kN. The motion resistance of the vehicle due to terrain compaction is computed as:

(i) For $0 \le z \le 5cm$: $R_c = 2B\left(\frac{k_p z_1^{\,2}}{2}+\frac{4}{3D_h}m_m z_1^{\,3}\right)$ (7)

(ii) For $z \ge 5cm$: $R_c = 2B\left(\frac{k_p z_2^{\,2}}{2}+\frac{4}{3D_h}m_m z_2^{\,3}\right)+C_{sk}P_cA_c$ (8)

The motion resistance of the vehicle due to internal friction losses is computed by the following equation mentioned by Wong. Y.J. [9]:

$$R_{in} = \left(\frac{W}{10^6}\right)\left[222 + 3v_t\right] \quad (9)$$

where, R_{in} is the motion resistance of the vehicle for internal friction of the moving parts in kN, v_t is the theoretical velocity of the vehicle in km/h, W is the vehicle weight in kg.

2.2 Vehicle Design and Development

Computer Aided Design Ds Catia V5 version 16 software package has been used to develop the three-dimensional design of the flexible skirt air cushion and air cushion track vehicle model. All of the component of the track such as rubber track, front idler, road wheel, rear sprocket, supporting wheel and tension device have been designed based on identified optimized design parameters. The design is analyzed further for its practibility and capability to withstand all the applied stresses while transverse in the designated terrain.

3. RESULTS AND DISCUSSIONS

The stress analysis has been carried out using CATIA for the two different loads 3 N and 5 N respectively (Figure 3 to 4). In the figures, red colour has been indicated as the maximum stresses and blue colour has been as the minimum stresses. Figure 3 to 4 indicate the air cushion in which rubber material have been used for the analysis using CATIA. The stress analysis has been done with von misses type in which the value for each stresses applied at the object has been shown for each load applied. The Young Modulus for the rubber material is $2x10^6$ N/m^2,

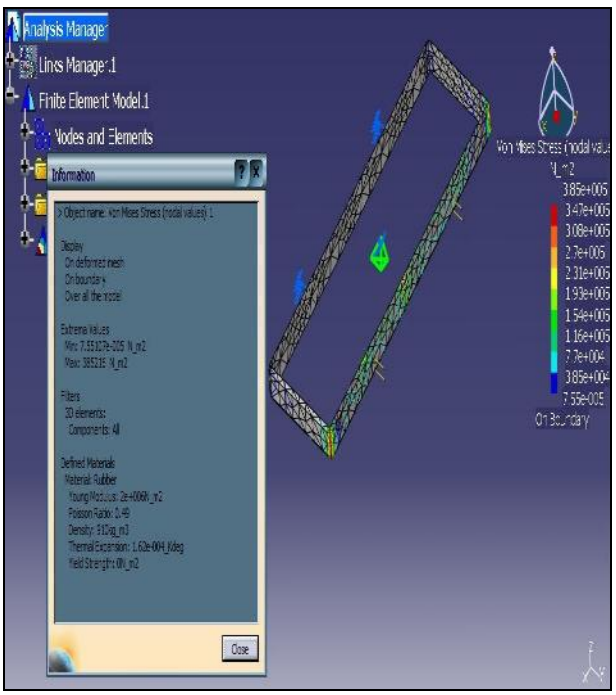

Figure 3: Analysis with 3 N load

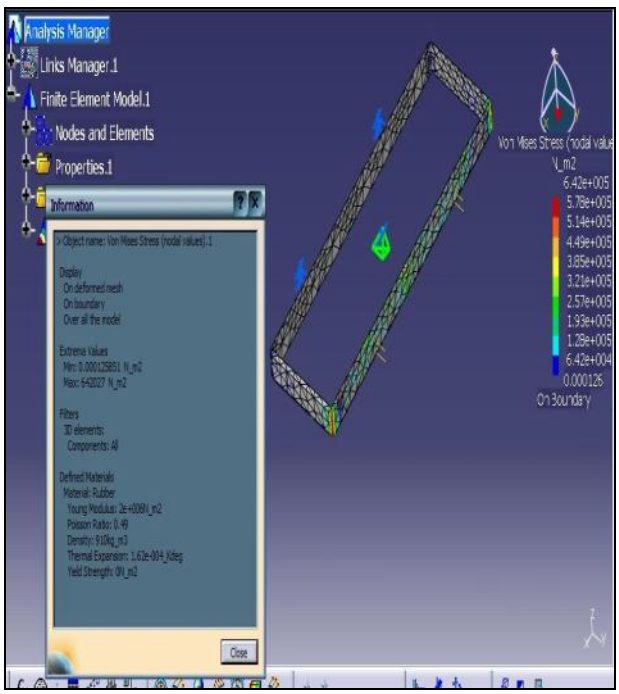

Figure 4: Analysis with 5 N load

the poison ratio is 0.49 and the density is 910 kg/m^3. The cushion has been deformed mesh when two different loads such as 3 N and 5 N are applied. The minimum values have been obtained as $7.551x10^{-5}$ N/m^2, and $0.000126x10^{-6}$ N/m^2 for 3 N and 5 N loads respectively. Similarly the maximum values have been obtained as $3.852x10^5$N/m^2 and $6.42027x10^5$N/m^2 for the two different loads respectively.

4. CONCLUSIONS

Based on the mathematical model and simulation data, it can be concluded that vehicle ground pressure could be made 7kN/m^2 by adding flexible air cushion with track ground contact area and thus optimal load distribution ratio can be obtained which results in minimum total power consumption. From the filed demonstration, it is observed that the ground contact area of the vehicle without air cushion cannot help the vehicle to float on the soft terrain. But the vehicle using air cushion can make the vehicle lifting the ground by eliminating the resistances.

ACKNOWLEDGEMENTS

The authors are grateful for the support provided by financial assistance from the University Industry Selangor, and faculty of Engineering for the overall facilities.

REFERENCES

[1] Ooi, H. S., Theoretical investigation on the tractive performance of MALTRAK on soft padi soil, MARDI, Report No. 116, 1993.
[2] Yahya, A, Jaafar, M.S., and Arbi, K., Mechanical infield collection of oil palm fresh fruit bunches, *Fruit, Nut and Vegetable Production Engineering*, Vol. 1 (1997), pp. 317-326.
[3] Luo, Z., Yu, F., and Chen, B.C., Design of a novel semi-tracked air-cushion vehicle for soft terrain, *Int. Journal of vehicle Design*, Vol. 31 (2003), No. 1, p. 112-123.
[4] Ataur, R., Azmi, Y., Zohaide, B., Ahmad, D., and Wan, I., Mechanical properties in relation to mobility of Sepang peat terrain in Malaysia, *Journal of Terramechanics*, Vol.41 (2004), No.1, pp.25-40.
[5] Ataur. R., Mohiuddin, A.K.M., and Altab. H., Effectiveness of the developed instrumentation system on the vehicle tractive performance measurement, *International Journal of Mechanical and Materials Engineering*, Vol 2 (2007), No. 2, 189-199.
[6] Wong, J.Y., Optimization of design parameters of rigid-link track systems using an advanced computer-aided method, Proc. Institution of Mechanical Engineers, Part D, *Journal of Automobile Engineering*, Vol. 212 (1998), No. D3, pp. 153-167.
[7] Yong, R.N, Fattah, E.A, and Skiadas, N., Vehicle traction mechanics. Developments in Agricultural Engineering, *Elsevier science*, Amsterdam, Netherlands, Vol.3 (1984), pp.234-248.
[8] Okello, J.A., Watany, M., and Crolla, D.A., Theoretical and Experimental Investigation of Rubber Track Performance Models, *Journal of Agricultural Engineering Res.*Vol. 69 (1998), pp.15-24.
[9] Wong, J. Y., Theory of Ground Vehicles, John Wiley and Sons, Inc. pp 295-323, 2001.

Proceedings of the 4th BSME-ASME International Conference on Thermal Engineering
27-29 December, 2008, Dhaka, Bangladesh

CONVECTIVE HEAT TRANSFER CHARACTERISTICS OF SISAL-WATER NANOFLUID IN A SHELL AND COIL HEAT EXCHANGER

K.P. Kumar[a,1], D.N. Rao [b], V. Murali krishna[c,*], K.V.N. Srinivasa Rao[a,2]

[a]Dept. of Mechanical Engineering, Vignan's Engineering College, Vadlamudi, Guntur –522 213, India
[b]Dept. of Mechanical Engineering., college of Engineering, Andhra University, Visakhapatnam-530 003, India
[c]Dept. of Mechanical Engineering, Vignan's Institute of Information Technology, Visakhapatnam, India
***** Corresponding author, E-mail: murvmk@yahoo.com, [1]E-mail: phani_vec@rediffmail.com

ABSTRACT

Enhancement of convective heat transfer has been the topic of major interest in the design of thermal equipment operating at different system conditions. In very recent literature, one can find that substantial enhancement in heat transfer can be achieved by including low volumetric concentration of nanoparticles of different magnitudes in the flow medium. The research has been focused on the preparation of nanofluids using metal and metal oxide nanoparticles. However the usage of biodegradable nanofibres to prepare nanofluids is yet to be explored. In the present experimental study biodegradable nanofibres are produced from natural sisal fibres. The biodegradable nanofluid is prepared by dispersion of nanofibres in the base medium of water. The experiments are conducted in a shell and coil heat exchanger with agitator to study the heat transfer rates of nanofluid stored in a shell. The heat transfer coefficients of sisal-water nanofluid at different nanofibre volume fractions are obtained from experiments for different mass flow rates of water flowing through a coil. The experimental results show the increase in heat transfer coefficient with the increase in volume fraction of nanofibre in base fluid.

KEY WORDS: *Sisal-water nanofluid, shell and coil heat exchanger, Nanofibres.*

1. INTRODUCTION

Heat transfer through a fluid medium finds many engineering applications such as heat exchangers, refrigeration, automobiles and power plants. Heat transfer in fluids is essentially through convection. However heat transfer coefficients depend on thermal conductivity of the fluid. To improve the thermal conductivity of a fluid, suspension of solid particles is an effective strategy as thermal conductivity of solids is greater than that of fluids. However the milli and micro sized particles are prone to sedimentation and clogging in micro channels. In contrast, nanofluid is stable colloidal suspension of a low volume fraction of solid particles of nano size, dispersed in conventional heat transfer fluid, which may offer an enhancement of fluid thermal conductivity without sedimentation and clogging problems.

Pak and Cho [1] investigated experimentally the turbulent friction and heat transfer behaviors of dispersed fluids (Al_2O_3 and TiO_2 particles suspended in water) in a circular pipe. Lee et al. [2] observed enhancement of thermal conductivity of nanofluids using CuO and Al_2O_3 nanoparticles with water and ethylene glycol compared to base fluids. The thermal conductivities of nanofluids with CuO and Al_2O_3 nanoparticles have been determined experimentally using steady-state parallel-plate technique by Wang et al. [3], for different

base fluids such as water, ethylene glycol and engine oil. The thermal conductivity of these nanofluids increased with increasing volume fraction of the nanoparticles. Xuan and Li [4] studied the augmentation of thermal conductivity of Cu-water nanofluid for different volume fractions of Cu nanoparticles. Xuan and Roetzel [5] concluded from their findings that the heat transfer enhancement is due to increase in thermal conductivity or due to thermal dispersion caused by random motion of the particles coupled with enhanced thermal conductivity. Das et al. [6] investigated the variation of thermal conductivity of nanofluids (Al_2O_3-water and CuO-water) with temperature using temperature oscillation technique. They observed an increase in thermal conductivity with temperature. Yang et al. [7] measured experimentally the convective heat transfer coefficients of several nanoparticle-in-liquid dispersions under laminar flow in a horizontal tube heat exchanger. Koo and Kleinstreuer [8] showed that the Brownian motion has more impact on the thermal properties of nanofluid than thermo-phoresis. Herish et al. [9] have conducted experiment to determine the thermal conductivity of Al_2O_3 -water nanofluid during forced convection in laminar flow through a circular tube with constant wall temperature. Recently Zhang et al. [10] measured the thermal conductivity and thermal diffusivity of Au-toluene, Al_2O_3-water, TiO_2-water, CuO-water and carbon nanotubes-water nanofluids using the transient short-hot-wire technique. Even though a considerable amount of work focusing on the metal nanofluids is available, use of nanofluid using natural nanofibres is not reported in the literature. The natural fibres are available in abundance, form a renewable resource such as jute, bamboo, coir, sisal, pineapple and these are also biodegradable. The sisal-water nanofluid is prepared by dispersing the sisal nanofibres in the distilled water. Hence in view of the importance of the problem experiments are conducted to find the heat transfer coefficient of sisal-water nanofluid in a shell and coil heat exchanger.

2. PREPARATION AND CHARACTERIZATION OF NANOFIBRES

The sisal nanofibres are prepared in two steps. In the first step the alkali treated sisal fibres are chopped into small lengths of about 10 mm and fed to D.P.Pulveriser, which runs at a speed of 6000 rpm. The fibres are collected in the form of whiskers from the D.P.Pulveriser. Pulverizing is followed by ball milling for about 140 hours at 60 r.p.m with heavy weight aluminum balls in M.S.vessel to realize them in the form of nanofibres. The obtained nanofibres are characterized by Transmission electron microscope (TEM). Fig.1 shows the Transmission Electron Microscope (TEM) photograph of sisal nanofibres. From the photograph it may be observed that the particles are having spherical shape and they are approximately 12 nm in diameter.

3. EXPERIMENTAL SETUP

The tube coils are one of the best methods to provide the turbulence and the effective heat transfer rates with minimum space. Hence in the present study a shell and coil heat exchanger is fabricated to study the enhancement of heat transfer rate with the dispersion of nanofibres in base fluid stored in a shell. The schematic experimental setup is shown in Fig. 2. Helical coils of inner diameter of 200mm made of copper tube of 8mm inner diameter are placed in a shell. The electrical heater is fitted to vessel to heat the nanofluid stored in the shell. The agitator is used to stir the nanofluid continuously. The agitator is driven by an electric motor. Before measuring the convective heat transfer coefficient of nanofluid, the reliability and accuracy of the experimental system are estimated by using water as the working fluid. Distilled water is filled in the shell to about 85% of its capacity. The agitator stirs water continuously. The inlet end of the coil is connected to water supply line and flow

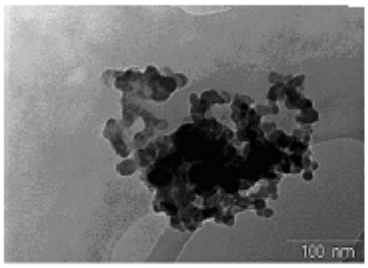

Fig. 1. TEM photograph of sisal fibers

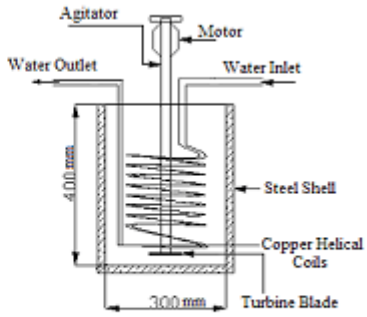

Fig. 2. Schematic layout of experimental setup

regulator is used to adjust the flow rate of the water flowing through coil. Pt-100 sensors of 0.1°C resolution are used to measure the inlet and outlet temperatures of the water flowing through the coil, and water stored in the vessel. Water in the vessel is heated to a desired temperature using the electric heater. The temperature of water in the vessel is maintained constant by using the thermostat. After attaining the steady state the inlet and outlet temperatures, and mass flow rates of water flowing through coil are measured. The mass flow rates are measured using a calibrated measuring flask and digital stop clock of 0.01 seconds accuracy. The experimental overall heat transfer coefficient ($U_{o,e}$) is determined from the relation given below.

$$U_{o,e} = \frac{\dot{Q}}{A_o \Delta T_{LMTD}} = \frac{\dot{m} C_p (T_{co} - T_{ci})}{A_o \Delta T_{LMTD}} \qquad (1)$$

The theoretical overall heat transfer ($U_{o,th}$) is obtained from the following equation.

$$\frac{1}{U_{o,th}} = \left(\frac{1}{h_{i,th}}\right)\left(\frac{A_o}{A_i}\right) + \frac{1}{h_{o,th}} \qquad (2)$$

The theoretical outside heat transfer coefficient ($h_{o,th}$) is calculated from the correlation given by Oldshue and Gretton [11].

$$\frac{h_{o,th} D_o}{K} = 0.17\left(\frac{D_a^2 N \rho}{\mu}\right)^{0.67} \times \left(\frac{C_p \mu}{K}\right)^{0.37} \times \left(\frac{D_a}{D_J}\right) \times \left(\frac{D_o}{D_J}\right)^{0.5} \qquad (3)$$

The theoretical inside heat transfer co-efficient ($h_{i,th}$) is calculated using the following equation (Incropera and DeWitt [12]).

$$\frac{f}{8} = \frac{Nu\, Pr^{2/3}}{Re\, Pr} \quad \text{where } Nu = \frac{h_{i,th} d_i}{k} \text{ and } Re = \frac{4\dot{m}}{\pi d_i \mu} \qquad (4)$$

In the above equation the friction factor 'f' is obtained from Moody diagram [13]. The properties of water are calculated by using the mean value of the temperatures of water at the inlet and outlet of the coil.

Fig. 3 shows the comparison of the experimental ($U_{o,e}$) and theoretical ($U_{o,th}$) overall heat transfer coefficients at different Reynolds numbers of water flowing through the coil. It can be found from Fig. 3 that the agreement between the experimental results and the calculated values for water is good. Uncertainty of the experimental data may result from the measuring errors of parameters such as heat flux, surface area and LMTD. The uncertainty of the experimental system is less than 4 percent. The uncertainty of the experimental system is evaluated using the following equation (Beckwith et al. [14]).

$$\frac{U_{U_o}}{U_o} = \sqrt{\left(\frac{U_{\dot{Q}}}{\dot{Q}}\right)^2 + \left(\frac{U_{A_o}}{A_o}\right)^2 + \left(\frac{U_{LMTD}}{LMTD}\right)^2} \qquad (5)$$

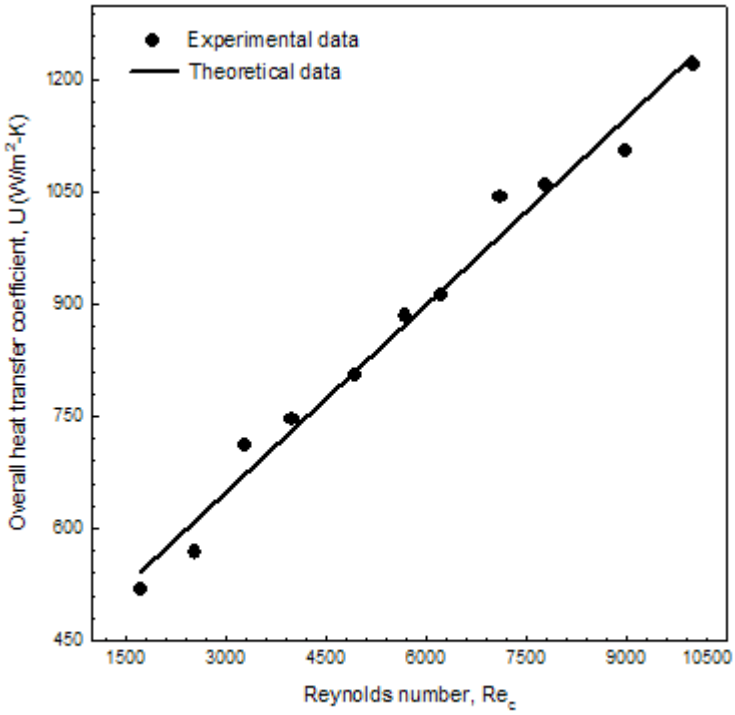

Fig. 3. Comparison of theoretical and experimental overall heat transfer coefficients of water

4. EXPERIMENTAL STUDY OF NANOFLUID

The sisal-water nanofluid is prepared by dispersing the sisal nanofibres in the distilled water stored in the vessel using the procedure given by Xuan and Li [4]. Uniform dispersion of nanofibres in the base fluid finds vital role in the heat transfer applications. Hence to know the rate of settlement of the sisal nanofibres in water, the required volume of nanofibres are mixed in the chemical measuring flask with distilled water and ultrasonic vibrations are used for 12 hours. Settlement time of nanofibres is observed at different intervals, which indicates the dispersion rate. After successful dispersion of 0.5% volume fraction biodegradable sisal nanofibres in water using ultrasonic vibrations about 12 hours, no sedimentation is observed for another 12 hours and thereafter a minor sedimentation is observed with 2% to 3% (by volume) suspensions for next 12 hours.

The sisal-water nanofluids of different volume fractions of sisal nanofibre particles (ranging from 0.05 to 0.5%) are prepared. The experiments are conducted on the same experimental setup to investigate the enhancement in heat transfer with nanofluid for different flow rates of water flowing through coil. The experiments are also performed for different volume fractions of nanofibre particles ranging from 0.05 to 0.5% in base fluid for three different mass flow rates (Re = 1700, 5000 and 10000) of cold fluid flowing through the coil.

5. RESULTS AND DISCUSSIONS

Fig. 4 shows the effect of Reynolds number of cold fluid flowing through the coil on overall heat transfer coefficient for different nanofibres concentrations in base fluid stored in the vessel. It can be observed from curves 1 and 4 of Fig.4, that the overall heat transfer coefficient is increased more than 35 percent with the volume fraction 0.5 percent (curve 1) of nanofibre particles compared with water (curve 4). The increase in heat transfer coefficient is due to increase in thermal conductivity of water with the addition of nanofibres, and also due to increase in heat transfer to the cold fluid due to random motion of nanofibres

suspended in water and availability of larger surface area with nanosized fibres. The experimental results also indicate that the heat transfer coefficient of a sisal-water nanofluid increases with the increase in volume fraction of nanofibre particles in base fluid. The curves1, 2 and 3 of the same figure show the same trend i.e., the heat transfer to the cold fluid increases with the increase in volume fraction of nanofibres in the base fluid. The volume fraction of the nanofibre particles increases from 0.1 percent to 0.5 percent (for example) the heat transfer coefficient is increased approximately by 20 percent (maximum) at the same Reynolds number. As expected, it can be observed from Fig. 4 the heat transfer coefficient of the nanofluid increases with the mass flow rate of the cold fluid.

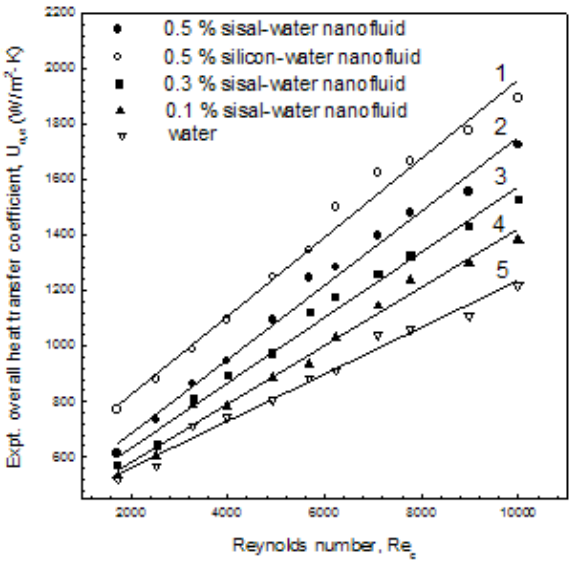

Fig. 4. Effect of mass flow rate of cold fluid on overall heat transfer coefficient

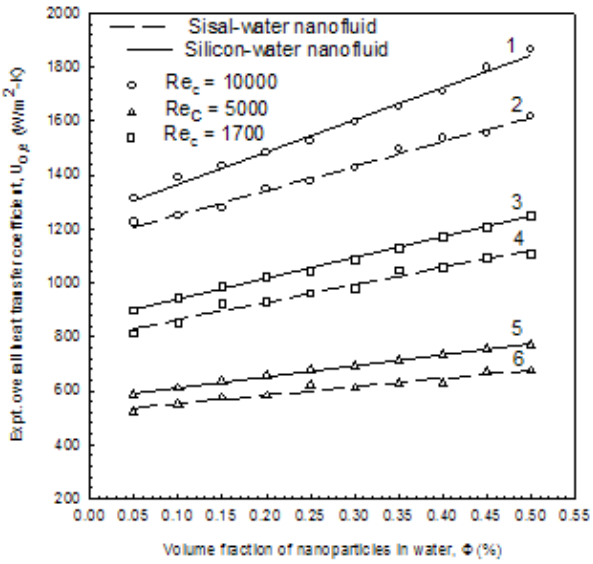

Fig. 5. Variation of overall heat transfer coefficient with volume fraction of nanofibers

The experiments are also conducted by varying the volume fraction of sisal nanofibres in the water from 0.05 to 0.5% (increment of 0.05%) for laminar and turbulent flows of cold water. Fig. 5 shows the variation of overall heat transfer coefficient with the volume fraction of nanofibres in water for three different Reynolds numbers (1700, 5000 and 10000) of cold fluid flowing through the coil. Fig. 5 shows an improvement in the rate of heat transfer to the cold fluid due to the addition of nanofibres even at very low concentrations. As the concentration of nanofibres in the water increases, a further increase in the heat transfer rate is observed. In turbulent flow i.e., curves 1 and 2 of Fig. 5, a steep increase in heat transfer coefficient is observed with an increase in volume fraction of nanofibres due to turbulence imparted to the nanofibres suspended in water. The curve 3 of the same figure indicates an increase in heat transfer to the cold fluid flowing in laminar flow with the increase in concentration of sisal-water nanofluid.

6. CONCLUSIONS

Heat transfer rates of sisal-water nanofluids are enhanced compared to water. The overall heat transfer coefficient is increased more than 35 % for the nanofluid with the volume fraction 0.5 percent of nanofibre particles compared with water. Sisal fibres are abundantly available, cheap and the production cost of nanosisal fibre particles is less. Also the sisal nanofibres are biodegradable, echo friendly and not necessary to recycle the nanofibre particles like metal nanoparticles. Hence metallic nanoparticles can be replaced with natural sisal nanoparticles in low temperature heat transfer applications as a coolant.

7. NOMENCLATURE

A	surface area of the coil, m^2	D_o	outer dia. of coil, m
D_a	agitator diameter, m	D_j	inner dia.of shell, m
C_p	specific heat of fluid, J kg^{-1} K^{-1}	f	friction factor
h	convective heat transfer coefficient, W m^{-2} K^{-1}	N	speed of agitator, rpm
K	thermal conductivity, W m^{-1} K^{-1}	l	length of helical coil, m
$\dot{m}_c$	mass flow rate of coil fluid (water), kg s^{-1}	T	temperature, K
Nu	Nusselt number	Re	Reynolds number
Pr	Prandtl number	d_i	inner dia. of coil, m
U	overall heat transfer coefficient, W m^{-2} K^{-1}	μ	viscosity, kg $m^{-1}s^{-1}$
ΔT_M	logarithmic mean temperature difference,	ρ	density, kg m^{-3}
ϕ	volume fraction of nanofibres, %		

8. REFERENCES

[1] Pak B., Cho Y., Hydrodynamic and heat transfer study of dispersed fluids with sub-micron metallic oxide particles, Experimental Heat Transfer, 11 (1998) 151-170.

[2] Lee S, Choi S.U.S, Li S, Eastman J.A., Measuring thermal conductivity of fluids containing oxide nanoparticles. ASME J Heat Transfer, 121 (1999) 280–289.

[3] Wang X, Xu X, Choi S.U.S., Thermal conductivity of nanoparticle–fluid mixture, J Therm Phys Heat Transfer, 13 (1999) 474–80.

[4] Xuan Y, Li Q, Heat transfer enhancement of nanofluids, Int J Heat Fluid Flow 21 (2000) 58–64.

[5] Xuan Y, Roetzel W, Conceptions for heat transfer correlation of nanofluids, Int. J. Heat and Mass Transfer, 43 (2000) 3701-3707.

[6] Das S.K, Putra N, Thiesen P, Roetzel W., Temperature dependence of thermal conductivity enhancement for nanofluids, ASME J Heat Transfer 125 (2003) 567–574.

[7] Yang Y, Zhang Z.G., Grukle A.K., Anderson W.B., Wu G., Heat transfer properties of nanoparticle-in-fluid dispersions (nanofluids) in laminar flow, Int. J. Heat and Mass Transfer, 48 (2005) 1107-1116.

[8] Koo J, Kleinstreuer C., Impact analysis of nanoparticle motion mechanisms on the thermal conductivity of nanofluids, Int. Comm. Heat Mass Transfer, 32 (2005) 1111–1118.

[9] Heris S. Z, Esfahany M.N., Etemad S. Gh., Experimental investigation of convective heat transfer of Al_2O_3 / water nanofluid in circular tube, Int. J. Heat Fluid Flow 28 (2007) 203-210.

[10] Zhang X, Gu H, Fujii M, Effective thermal conductivity and thermal diffusivity of nanofluids containing spherical and cylindrical nanoparticles, Expt. Thermal Fluid Sciences, 31 (2007) 593-599.

[11] Oldshue J.Y., Gretton A.T., Helical coil heat transfer in mixing vessels, Chem. Eng. Prog, 50(1954) 615-621.

[12] Incropera, F.P. and DeWitt, D.P., Fundamentals of Heat and Mass Transfer, 5th edition, John Wiley & sons (Asia) Pvt. Ltd, New Delhi (2007) P. 491.

[13] Moody, L. F., Trans. ASME, vol. 66, (1944) p. 671.

[14] Beckwith, T.G., Marangoni, R.D. and Leinhard. V. J.H., Mechanical Measurements, 5th edition, Addison-Wesley publishing company, New York, 2006.

Proceedings of the 4th BSME-ASME International Conference on Thermal Engineering
27-29 December, 2008, Dhaka, Bangladesh

AERODYNAMIC TESTING METHODOLOGY FOR SPORTS GARMENTS

Harun Chowdhury[1], Firoz Alam[1], David Mainwaring[2], Aleksandar Subic[1], Margaret Tate[2] and Dorothy Forster[2]

[1]School of Aerospace, Mechanical and Manufacturing Engineering, [2]School of Applied Sciences
RMIT University, Melbourne, Australia

E-mail: harun.chowdhury@rmit.edu.au

ABSTRACT

The material characteristics of textiles used in elite sports garments have been shown to exhibit a significant influence on both the sporting performance as well as their aesthetics, and particularly in those sports where aerodynamic resistance and its associated energy expenditure impact on winning times. This project examines standard cylindrical arrangements in wind tunnel environments that can provide precise data on aerodynamic drag and lift which can be correlated to fabric surface textures, material properties and air permeability.

Key words: *Wind tunnel testing, drag, aerodynamic properties, fabric.*

1. INTRODUCTION

The suitability of materials for sports applications, including textiles for sports garments, like materials for all applications must meet a range of performance parameters depending on the specific requirements imposed by any one application. Strangwood [1] points out that the close interplay of design and sports materials brought about by engineering modelling is only as good as the data on which it is based. Technological innovation, in both design and materials, has played a significant role in sport achieving its current standing in both absolute performance and its aesthetics. In sports garments, two examples that clearly exemplify design and materials are the graduated compression garments and the swimming bodysuits.

Aerodynamic properties play a significant role in the garments across a wide range of sports including cycling, speed skating, down hill skiing, ski jumping, bobsleigh and sprint running. Considerations in this aerodynamic performance include the textile weave or knit, seam and fastener placement and air permeability. Elite competition usually involves very short winning time margins in events that often have much longer timescales, making aerodynamic resistance and its associated energy loss during the event significant in the outcome. In fact, a two fold increase in athlete velocity results in an eight fold increase in the drag force needing to be overcome [2]. There have been a series of research studies over the last two decades identifying the reduction of aerodynamic drag in sports garments [e.g. 3-6].

Brownlie [4], carrying out systematic wind tunnel studies of drag and flow transitions utilizing both mannequins with athletic apparel and cloth covered cylinder, showed that cylinders with three types of cloth experienced significantly less drag than bare cylinder and earlier onsets of the flow transition which could have been attributed to surface roughness, although neither the cylinder and nor the mannequin with non-porous fabric underwent such a flow transition.

The aerodynamic evaluation of surface coating materials such as textiles, a cylinder provides a readily available generic standard geometry if established with the correct experimental arrangement. Generally the standard cylinder in this textile testing consists of three segments of cylinder parts: non-active top and bottom sections and an active middle section, where the top and bottom sections are used to minimise the aerodynamic influence on the active middle section. However, it is not apparent what effect of the non-active top and bottom sections of the cylinder have on the aerodynamic properties of the central active section. Therefore, the primary objective of this paper is to design and develop standard cylinder testing protocols and also evaluate the effects of top and bottom sections on the middle section of the cylinder.

2. TESTING METHODOLOGY AND EXPERIMENTAL PROCEDURE

2.1 Description of Standard Cylinder and Experimental Arrangement

In order to obtain generic aerodynamic properties of a range of sports textiles experimentally, a 110 mm diameter cylinder was made. The cylinder was made of PVC tubing and made solid using a filler to make it structurally rigid. The cylinder has three sections: active section on the middle, two non-active or passive sections (top and bottom sections). The middle section is vertically supported on a six component force sensor using a threaded strut. The non-active bottom section was secured to the wind tunnel floor while the top section was secured with the floor using L-shaped bracket (Figure 1) such that the top and bottom sections had no physical contact with the middle active section, with 5 mm gaps maintained between the sections. In order to quantify these effects of top and bottom sections on aerodynamic properties of active middle section, the active section was tested in following configurations:

a) Active section with top and bottom sections
b) Active section with bottom non-active section only (no top section)
c) Active section with top non active section only (no bottom section)
d) Active section only (no top and bottom non-active sections)

All these testing configurations are shown in Figure 1, 2, 3, 4.

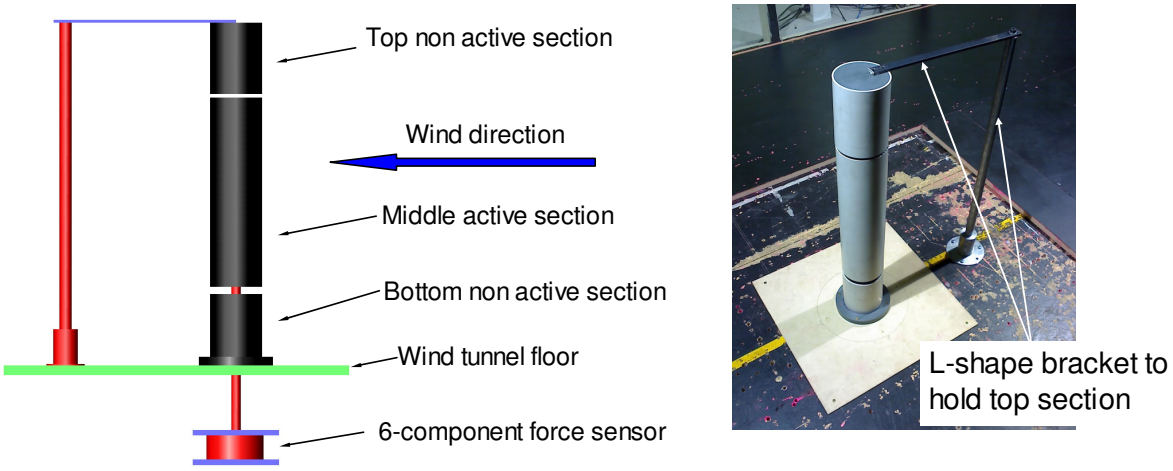

(a) Schematic CAD model (b) Cylinder in Wind Tunnel

Figure 1: Active middle section with non-active top and bottom sections

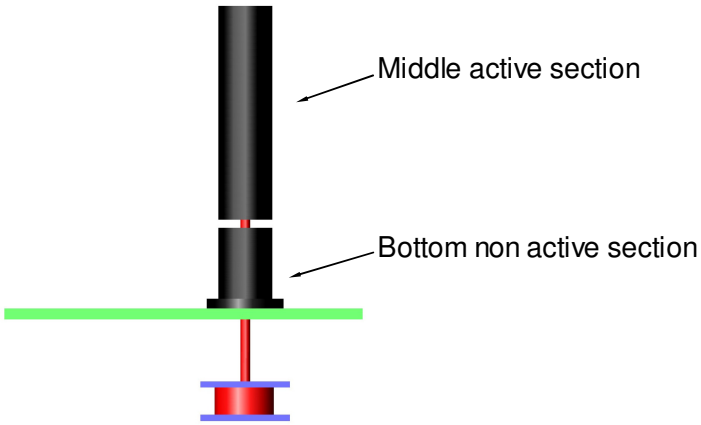

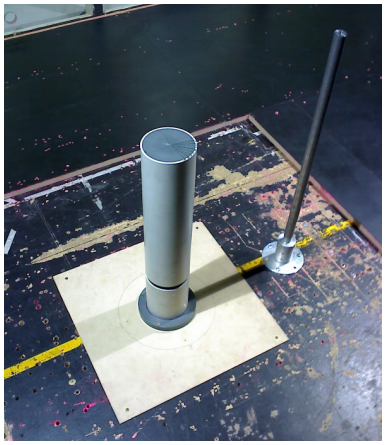

(a) Schematic CAD model (b) Cylinder in Wind Tunnel

Figure 2: Active middle section with non-active bottom section

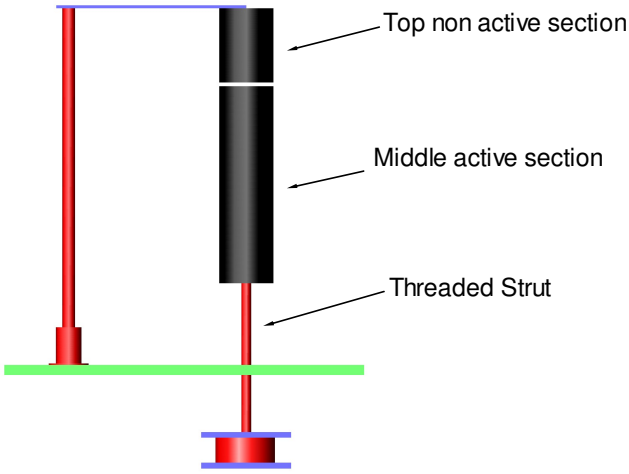

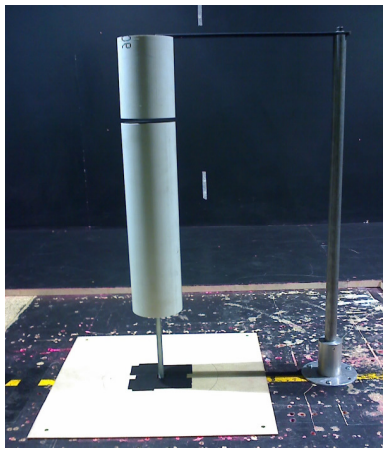

(a) Schematic CAD model (b) Cylinder in Wind Tunnel

Figure 3: Active middle section with non-active top section

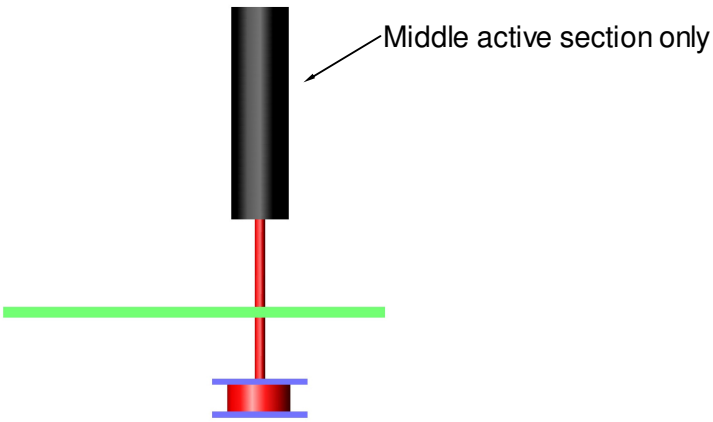

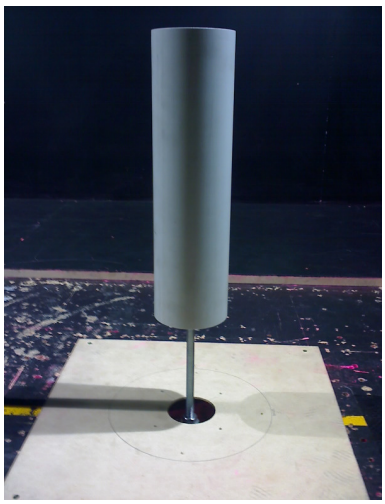

(a) Schematic CAD model (b) Cylinder in Wind Tunnel

Figure 4: Active middle section only (no top and bottom sections)

2.2 Wind Tunnel Facility

The RMIT Wind Tunnel used to measure the aerodynamic properties of standard cylinder with various configurations consisted of a closed return circuit wind tunnel with a maximum speed of approximately 150 km/h. The rectangular test section dimensions are 3 m (wide) x 2 m (high) x 9 m (long) equipped with a turntable to yaw the sample under test. A plan view of the tunnel is shown in Figure 5. The tunnel was calibrated before conducting the experiments with the tunnel air speed measured with a modified NPL ellipsoidal head Pitot-static tube (located at the entry of the test section) and connected to a MKS Baratron pressure sensor through flexible tubing. The mounting strut (sting) holding the cylinder was mounted on a six component force sensor (type JR-3), and the purpose made computer software was used to determine all 6 forces and moments (drag, side and lift forces, and yaw, pitch and roll moments) and their non-dimensional coefficients [2].

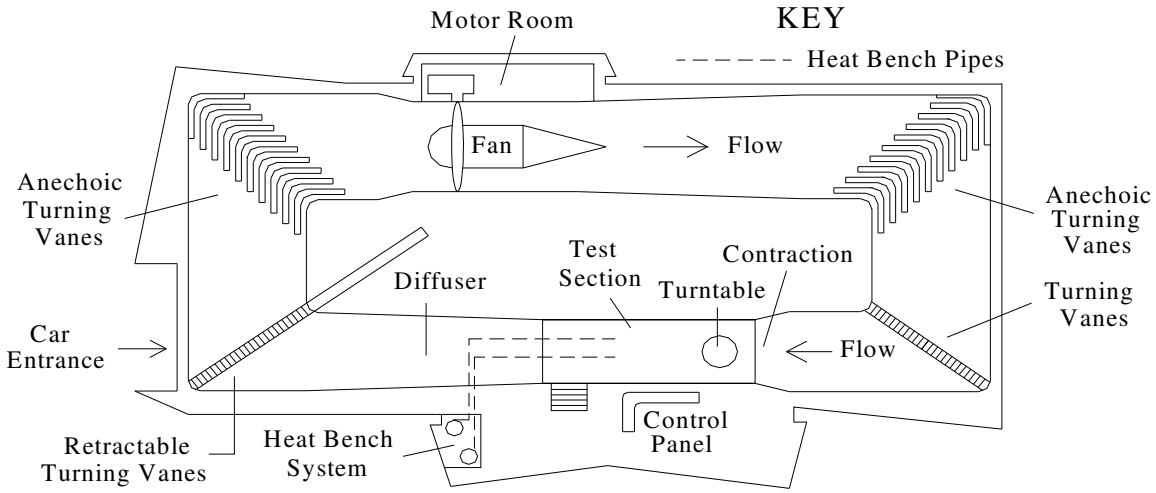

Figure 5: A plan view of RMIT University Wind Tunnel, Alam et al. [2]

Figure 6: Cylinder with all three sections in the test section of RMIT Wind Tunnel

3. RESULTS AND DISCUSSION

Drag force (F_D) data as a function of speed (V) from wind tunnel tests characterising this experimental arrangement is shown in Figure 7 for the different configurations. At low speeds with the bare cylinder, all configurations are similar, but at higher speeds (from 90 to 120 km/h) the values become different because of the transition from laminar to turbulent flow. Figure 8 shows the data in terms of the Reynolds numbers (Re) vs. coefficient of drag (C_D). It is clear that at low speed C_D is highest for the standard configuration without the top section than any other configuration, since the wind flow is not uniform around the central active section. This data shows that both the top and bottom sections must be utilized to achieve this uniformity of flow about the active section.

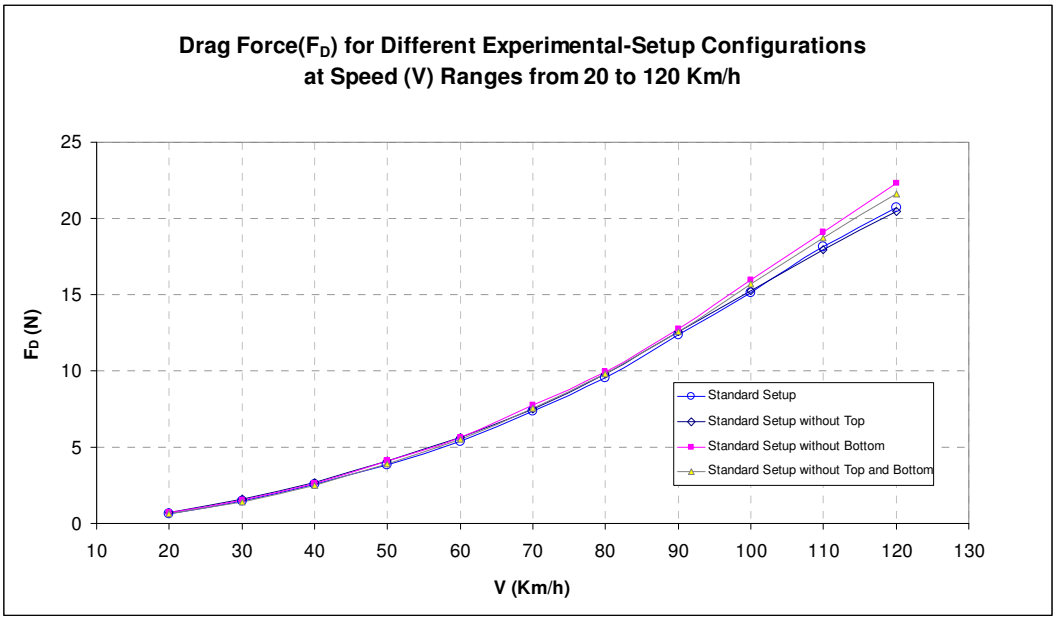

Figure 7: Drag force – velocity relationship for different arrangements without any sleeve

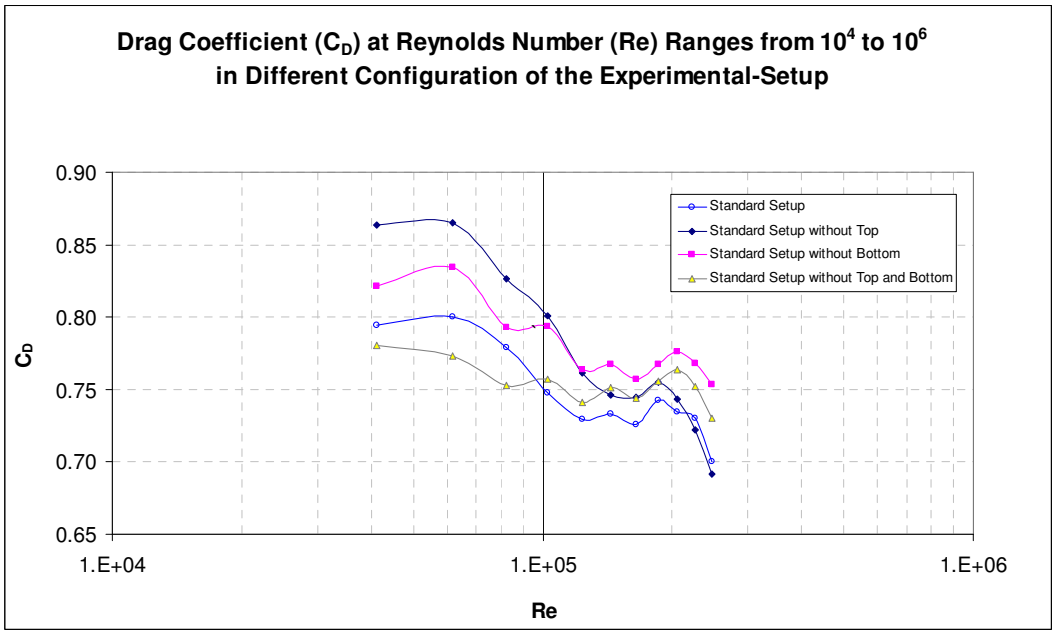

Figure 8: Reynolds number – drag coefficient for different arrangements without any sleeve

4. CONCLUSIONS

It is well recognised that aerodynamic properties play a significant role in sports garments. Here, we show the instrumental arrangement assembled to study the aerodynamic drag of sports textiles in a controlled manner that can be correlated to key material parameters such as surface texture, deformation, and air permeability.

ACKNOWLEDGEMENTS

The authors would like to express their sincerest thanks to Mr Patrick Wilkins and Mr Gilbert Atkins, School of Aerospace, Mechanical and Manufacturing Engineering, RMIT University for their technical assistance with the experimental set up in RMIT Wind Tunnel.

REFERENCES

[1] Strangwood, M., *In Materials in Sports Equipment*, Vol. 2, Ed. A. Subic, Woodhead Publishing, Ltd. Cambridge UK, pp. 3-33, 2007

[2] Gross, A., Kyle, C., Malewicki, D. *Sci. American* 249: 142-152, 1983

[3] Kyle, C.R., Caiozzo V. *Medicine and Science in Sports and Exercise* 18: 509-515, 1986

[4] Brownlie, L.W., Aerodynamic Characteristics of Sports Apparel, PhD Thesis, Simon Fraser University, British Columbia, Canada, 1992

[5] Brownlie, L.W., Kyle, C.R., Harber, E., Macdonald, R., Shorten, M.R., In *The Engineering of Sport 5*, Vol. 1, Ed. M. Hubbard, R.D. Mehta, J.M. Pallis, ISEA, Sheffield, UK, pp 90-96, 2004

[6] Kyle, C.R., Brownlie, L.W., Harber, E., MacDonald, R., Norstrom, M., In *The Engineering of Sport 5*, Vol. 1, Ed. M. Hubbard, R.D. Mehta, J.M. Pallis, ISEA, Sheffield, UK, pp 118-124, 2004

[7] Alam, F., Subic, A., Watkins, S., Naser, J. and Rasul, M. G., An Experimental and Computational Study of Aerodynamic Properties of Rugby Balls, *WSEAS Transactions on Fluid Mechanics*, Vol. 3 (3), pp 279-286, 2008

Proceedings of the 4th BSME-ASME International Conference on Thermal Engineering 27-29 December, 2008, Dhaka, Bangladesh

INTEGRATED MECHANICS FOR DESIGN OF THE HYBRID ELECTRICAL AIR-CUSHION TRACK VEHICLE FOR SWAMP PEAT

Ataur Rahman[a], Altab Hossain[b,*], A.K.M. Mohiuddin[a]

[a] Department of Mechanical Engineering, International Islamic University Malaysia, Malaysia
[b] Department of Mechanical Engineering, Faculty of Engineering, University Industry Selangor, Malaysia

ABSTRACT

This paper presents an integrated mechanics for the design of hybrid electrical air-cushion tracked vehicle (HETAV). Mechanics are incorporated with accounting the kinematics and dynamics behaviors of the vehicle tracked and air-cushion system. The air-cushion of HETAV is protected with a novel-design auto-adjusting supporting (AAS) system which can adjust automatically with absorbing the horizontal and vertical displacement of the air-cushion system. Simulated tractive effort has shown the requirement to develop an additional thrust to overcome the total motion resistance of the vehicle. A propeller is equipped with the vehicle to develop additional thrust for overcoming the dragging motion resistance. The performance of the HETAV is defined by traction and motion resistance. The simulation results show that the vehicle load distribution to the air-cushion system would not be too high since the power consumption by the air-cushion drag motion resistance is affected significantly on the total power requirement as well as the propeller develops an additional thrust of 0.2 kN while the track system develops only 1.674 kN for the vehicle loading condition of 2.04 kN.

Keywords: *Hybrid vehicle – Air cushion - Auto-adjusting-supporting system - Propeller.*

1. INTRODUCTION

The small scale HETAV design and development has been performed for justifying the introduction of a full scale similar vehicle on the low bearing capacity swamp peat terrain in Malaysia. The design of the vehicle has been achieved with developing the mechanics which is formulated with understanding the terrain nature, analyzing the mechanics of track-terrain and AAS-terrain interaction. The integrated mechanics is mainly developed with analyzing the mechanics of track-terrain and AAS-terrain interaction and partially simplifying the recommended mathematical models of the author's ref. [1-5]. The solutions to this set of equations define the vehicle sinkage, slippage, entry and exit angle of the track. Based on the set of equations, the vehicle ground pressure distribution, dynamic load transfer, motion resistance, and tractive effort are simulated. The propulsion system of the vehicle is comprised of track and air-cushion system. The track mechanism is used as the driving system to overcome the rolling motion resistance and the air cushion system is used to increase the floatation capacity of the

* Corresponding author: *E-mail address:* altab75@unisel.edu.my; Tel: 60-0169128403

vehicle. The driving force is provided to each of the track by an individual DC motor. The air-cushion system of this vehicle was designed in such a way that it would not slid on the terrain all the while with the vehicle movement. The additional thrust is provided to the vehicle by using a propeller for overcoming the drag resistance of the air-cushion system. As the terrain is unprepared and different types of decomposed materials are on the terrain, the air-cushion is protected by a novel design protecting system. It can be adjusted automatically by absorbing its longitudinal displacement with two horizontally attached shock absorbers and vertical displacement with four vertically attached springs. The air-cushion system makes the vehicle ground contact pressure 7 kN/m^2. The power transmission system of the vehicle is shown in Fig.1. The magnetic pick-up sensor is used in this study to measure the vehicle theoretical speed.

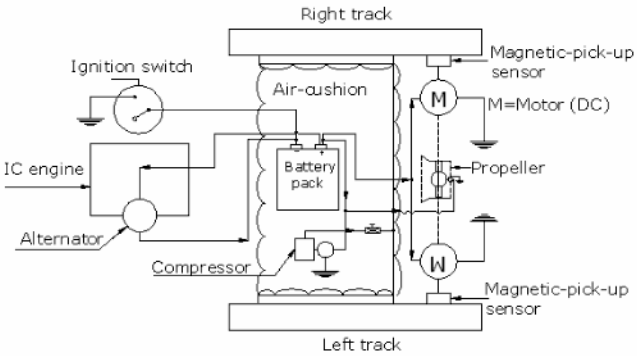

Figure 1: Vehicle power transmission system

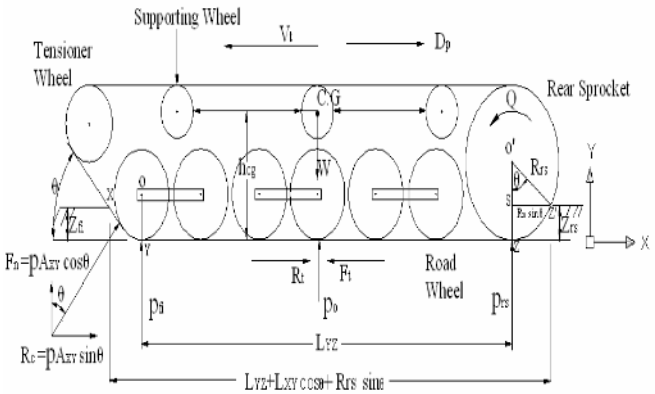

Figure 2: Forces acting on track system

2. METHODOLOGY

2.1 Mechanics of Air-Cushion Track Vehicle

Mathematical model is formulated with understanding the terrain nature, analyzing the mechanics of track-terrain interaction, and by simplifying the mathematical models of the author's ref. [4-11]. Based on the set of equations, the vehicle ground pressure distribution, dynamic load transfer, motion resistance, and tractive effort are simulated. The tractive effort and motion resistance of the vehicle are formulated based on two sinkage conditions: (i) $0 \le z \le 5cm$ and (ii) $z \ge 5cm$. A rubber track vehicle of total weight *W*, track size including track ground contact length *L*, width *B*, rear sprocket R_{rs}, and road-wheel R_r, and height of the center of gravity h_{cg} is traversing under traction on a swamp peat terrain at a constant speed of v_t with driving torque *Q* at the rear sprocket as shown in Fig.2.

A. Traction Force

The tractive effort (traction) equation for the bottom of the vehicle's track ground contact part on peat terrain is computed by simplifying the equation of ref. [6]:

(i) For sinkage, $0 \le z \le 50\ mm$

$$F_b = (A_t c + (W_t)\tan\varphi)\left[\frac{K_w}{iL}e^1 - \left(1+\frac{K_w}{iL}\right)\exp\left(1-\frac{iL}{K_w}\right)\right] \text{ where, } A_t = 2(L_{YZ})(B), L = L_{YZ} \quad (1)$$

In Equation (1), F_b is traction that develop at the bottom part of the track in kN, *L* is the ground contact part of the track in m, A_t is the area of the track ground contact length in m^2, W_t is the vehicle load supported by the track system in kN, c is the cohesiveness in kN/m^2, φ is the

terrain internal friction angle in degree, K_w is the shear deformation modulus in m, i is the slippage of the vehicle in percentage, and B is the width of the track in m.

(ii) For sinkage, $z \geq 5cm$

When the vehicle sinkage is 50mm or more, the cushion-system of the vehicle will be in contact with the terrain. Therefore, the additional thrust of the vehicle will be needed to develop in order to overcome the dragging motion resistance of the vehicle. The traction of the vehicle is calculated by using the recommended equation of ref. [4] and ref. [8]:

$$F_t = \left(A_t c + W_t \tan\varphi\right)\left[\frac{K_w}{iL}e^1 - \left(1+\frac{K_w}{iL}\right)\exp\left(1-\frac{iL}{K_w}\right)\right] + F_{tac(add)} \qquad (2)$$

where, $A_t = \left(L_{XY}\cos\theta + L_{YZ} + R_{rs}\sin\theta\right)(B)$, $L = \left(L_{XY}\cos\theta + L_{YZ} + R_{rs}\sin\theta\right)$ and $L_{XY} = \frac{z}{\sin\theta}$

In Equation (2), $F_{tac(add)}$ is the additional tractive effort developed by the propeller in kN, and θ is angle between the track of 1st road-wheel to tensioned wheel and the ground in degree. Figure 3 shows the novel-design air-cushion protecting system. It is made in such a way that its

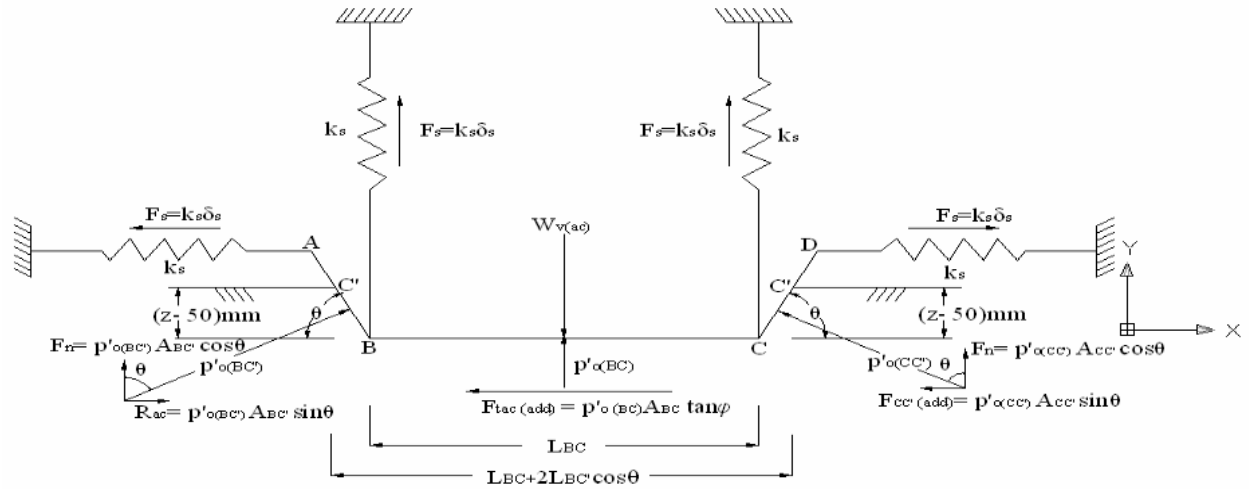

Figure 3: Air-cushion support system

weight does not affect on the vehicle's ground contact pressure and its vertical and longitudinal displacement don't affect the air-cushion inflation pressure as well. It is used to protect the air-cushion system from the external threat by adjusting its displacement automatically. Load transferring of the vehicle to the air-cushion system starts once the vehicle gets its sinkage 50 mm or more. The load transfer of the vehicle to the air-cushion system could be formulated as:

$$W_{v(ac)} = \left(p' - p\right)\left(A_{BC}\right) = \left(p'_0\right)\left(A_{BC}\right) \qquad (3)$$

(i) For sinkage, $z = 0.0mm$

$$W_{v(ac)} = \left[p' - \left(k_p z_{acs} + \frac{4}{D_{hac}} m_m z_{acs}^{\ 2}\right)\right]\left(A_{BC}\right) \qquad (4)$$

where, $z_{acs} = \dfrac{-\left(\dfrac{k_p D_{acs}}{4m_m}\right) \pm \sqrt{\left[\left(\dfrac{k_p D_{acs}}{4m_m}\right)^2 + \dfrac{D_{acs}}{m_m} p_0'\right]}}{2}$ and $D_{acs} = \dfrac{4(B_{acs})(L_{BC})}{2(L_{BC} + B_{acs})}$

(ii) For sinkage, $z \geq 50mm$

$$W_{v(ac)} = \left[p' - \left(k_p z_{acs} + \frac{4}{D_{hac}} m_m z_{acs}^{\ 2} \right) \right] (A_{BC} + 2A_{BC'} \cos\theta) \qquad (5)$$

where, $z_{acs} = \dfrac{-\left(\dfrac{k_p D_{acs}}{4m_m}\right) \pm \sqrt{\left[\left(\dfrac{k_p D_{acs}}{4m_m}\right)^2 + \dfrac{D_{acs}}{m_m} p_0'\right]}}{2}$ and $D_{acs} = \dfrac{4(B_{acs})(L_{BC} + 2L_{BC'}\cos\theta)}{2(L_{BC} + 2L_{BC'}\cos\theta + B_{acs})}$

In Equation (3), p_o' is the ground nominal pressure which could exist due to the transfer load of the vehicle to the air-cushion system in kN/m^2, p' is the vehicle ground contact pressure in kN/m^2, and A_{BC} is the contact area of the air-cushion support system as shown in Fig.3. The additional tractive effort of the vehicle at the air-cushion system could be calculated as follows:

(i) For $z = 50\,mm$: $F_{tac(add)} = p_o' A_{BC} \tan\phi$ (6)

(ii) For $z > 50\,mm$: $F_{tac(add)} = p_o' A_{AB} (\sin\theta) + p_o' A_{BC} \tan\phi$ (7)

B. Additional Thrust

Additional thrust that has needed the vehicle to overcome the dragging motion resistance is developed by using a propeller as shown in Figure 4. The *vector diagram* as shown in Figure 4 is

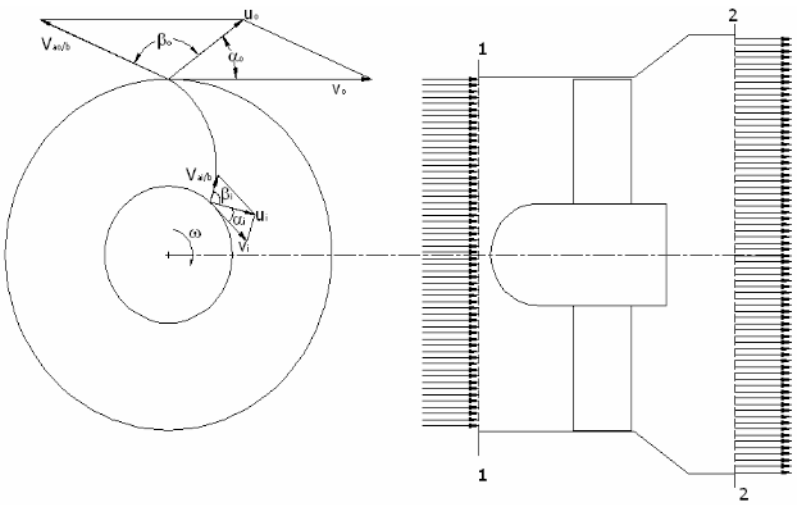

Figure 4: Propeller for the vehicle

used in analyzing the propeller geometry and its relationship to the flow of air. The subscripts *i* and *o* are used, respectively, for the inlet and exit flow conditions, *v* represents the peripheral

velocity of the impeller, $V_{a/b}$ represents the air velocity relative to the propeller blade, and u is the absolute air velocity air (a vector sum of v and $V_{a/b}$), α is the angle between absolute and peripheral velocity in degree and β is the blade angle. The input power to the propeller can be computed as [9]:

$$P_i = T\omega = \rho Q\omega(r_o u_o \cos\alpha_o - r_i u_i \cos\alpha_i) \tag{8}$$

where, ω is the angular velocity of the impeller in rad/sec.

The total energy head that the propeller imparts to the air is

$$H_P = \frac{u_o^2 - u_i^2}{2g} + \frac{p_0 - p_i}{\gamma} \tag{9}$$

The output power: $P_o = \gamma Q H_P = (\gamma Q)\left[\frac{u_o{}^2 - u_i{}^2}{2g} + \frac{p_0 - p_i}{\gamma}\right]$ (10)

where, $\gamma = \rho g$. In Equation (10), ρ is the density of air in kg/m^3, p_i is the pressure of air in kN/m^2 and u_i is the velocity of air in m/s, p_0 is the pressure of air in kN/m^2 and u_0 is the velocity of air in m/s at the section 1-1 and 2-2 of the propeller, respectively.

Thrust developed by the propeller: $F_{propeller} = (p_{22}A_{22} - p_{11}A_{11}) = F_{ac(add)}$ (11)

In Equation (11), the p_{11} and p_{22} are the pressure of section (1-1) and section (2-2), respectively, while, A_{11} and A_{22} are the area of the sections (1-1) and section (2-2).

C. Motion Resistance

The motion resistance of the vehicle is considered: (i) terrain compaction and zero dragging motion resistance when the vehicle sinkage is less than 50 mm; (ii) terrain compaction and dragging of the air-cushion when the vehicle sinkage is 50 mm or more. The motion resistance of the vehicle could be computed as follows:

(i) For sinkage, $z = 0.0\,mm$: $R_c = 2(p)(B)(L_{YZ})\tan\varphi$ (12)

where, $p = \left(k_p z + \frac{4}{D_{ht}} m_m z^2\right)$, $z = \frac{-\left(\frac{k_p D_{ht}}{4m_m}\right) \pm \sqrt{\left[\left(\frac{k_p D_{ht}}{4m_m}\right)^2 + \frac{D_{ht}}{m_m} p'\right]}}{2}$, $D_{ht} = \frac{4BL_{YZ}}{2(L_{YZ} + B)}$, $p' = \frac{W}{(L_{YZ})(2B)}$

(ii) For sinkage, $z = 50\,mm$: $R_c = (2)(B)(L_{YZ} + L_{XY}\cos\theta + R_{rs}\sin\theta)(p\tan\phi) + p_0' A_{BC}\tan\phi$ (13)

The pressure p could be computed by using the following equation of ref. [6]:

$p = \left(k_p z + \frac{4}{D_{ht}} m_m z^2\right)$ where, $D_{ht} = \frac{(4)(B)(L_{YZ} + L_{XY}\cos\theta + R_{rs}\sin\theta)}{2(L_{YZ} + L_{XY}\cos\theta + R_{rs}\sin\theta + B)}$, $p' = \frac{W}{(L_{YZ} + L_{XY}\cos\theta + R_{rs}\sin\theta)(2B)}$

(iii) For vehicle sinkage, $z > 50\,mm$:

$R_c = (2)(B)(L_{YZ} + L_{XY}\cos\theta + R_{rs}\sin\theta)(p)\tan\phi + p_o' A_{CD}(\sin\theta) + p_o' A_{BC}\tan\phi$ (14)

2.2 Simulation

The HETAV is mainly design for carrying 5.88 kN on the swamp peat terrain. But, the loading conditions of the vehicle during testing are considered 1.02 and 2.04 kN as the vehicle tested on the terrain is worst than the swamp peat terrain. The bearing capacity of swamp peat in Malaysia is considered 7kN/m² based on the report of ref. [11] and surface mat thickness 50 mm have been considered in this study. The vehicle loading conditions of 1.02 kN, and 2.04 kN and the traveling speed of 12 km/h are considered in this study. The simulation on the vehicle design parameters and performance are conducted by using the MATLAB and MS Excel.

3. RESULTS AND DISCUSSIONS

Figure 6 shows the relationship between the vehicle tractive effort and motion resistance. Result shows that the vehicle will be able to traverse on the terrain if the vehicle terrain compaction motion resistance remains within the shaded area. In this study the vehicle with total contact area 1.052 m^2 including 0.544 m^2 of air-cushion area has been optimized based on the bearing capacity of the terrain. Therefore, the track system only is able to develop 0.75 kN while the additional 0.15 kN tractive effort has needed to develop by the propeller in order to traverse

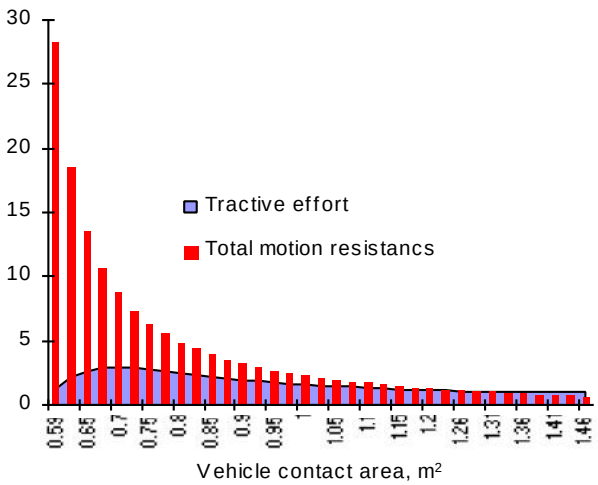

Figure 6: Relationship of the force and the motion resistance with contact area

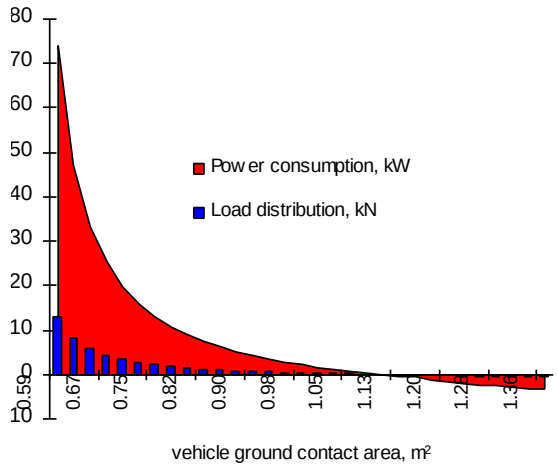

Figure 7: Relationship of the power consumption and load distribution with area

the vehicle on the peat terrain with overcoming the motion resistance. Figure 7 shows that the load distribution to the air-cushion system is decreased linearly with increasing the track ground contact area. The vehicle with ground contact area of 1.052 m^2 has distributed load of 0.45 kN and power consumption by the propeller of 1.02 kW. The vehicle travelling length of 200 m over the swamp peat terrain are considered for the simulation of vehicle ground contact pressure (VGP), traction, and load distribution. Air-cushion system is attached with the vehicle in order to maintain the vehicle sinkage and ground contact pressure. The vehicle is designed in such a way that it can travel on the moderate type of peat terrain with the help of tracked system by overcoming the motion resistance as the tracked total ground contact area is optimized based on

the minimum motion resistance exist on the tracked system, bearing capacity of the moderate terrain of 12kN/m^2, and maximum traction developed by the tracked system both in straight and turning motion. In this study, the simulation has been conducted for the vehicle on 200m traveling distance swamp peat terrain.

4. CONCLUSIONS

The air cushion is activated when the vehicle sinkage is closed to 0.05 m. Based on the simulation result it can be concluded that the vehicle load distribution to the air-cushion system would not be too much as the power consumption by the air-cushion drag motion resistance is affected significantly on the total power requirement of the vehicle which could be supported from the conclusion of ref. [7]. Other than that the power of the battery pack is too limited. The vehicle must have needed to develop additional thrust at least 0.2 kN as the vehicle track ground contact area is optimised by 0.505 m^2. Air-cushion system of the vehicle makes the vehicle ground contact pressure less than 7kN/m^2 with partially supporting the vehicle load. The propeller must have to manage an additional thrust of 0.20 kN while the track system develops only 1.674 kN for the vehicle loading condition 2.04 kN.

REFERENCES

[1] Ooi, H.S., Design and development of peat prototype track type tractor, *MARDI*, Report no.184, 1996.

[2] Shuib, A. and Hitam, A., Wakfoot the FFB evacuation vehicle. PORIM Information Series, *Palm Oil Research Institute of Malaysia. PORIM* TT No. 20, Pamphlet, 1998.

[3] Yahya, A., Jaafar, M.S., and Aribi, K., Mechanical infield collection of oil palm fresh fruit bunches, *Fruit, Nut, and vegetable production engineering*, Vol.1 (1997), p.317-326.

[4] Ataur, R., Azmi, Y., Zohadie, M., Ahmad, D and Ishak, W., Design and Development of a Segmented Rubber Tracked Vehicle for Sepang Peat Terrain in Malaysia, *Int. J. of Heavy Vehicle Systems*, Inderscience, UK, Vol.12 (2005), No.3, p.239-267.

[5] Bodin, A., Development of a tracked vehicle to study the influence of vehicle parameters on tractive performance in soft terrain, *Journal of Terramechanics*, Vol. 36 (1999), p.167-181.

[6] Wong J.Y., Theory of Ground Vehicles. John Wiley and Sons, Inc., 2001.

[7] Luo, Z., Yu, F., and Chen, B.C., Design of a novel semi-tracked air-cushion vehicle for soft terrain, *Int. Journal of vehicle Design*, Vol. 31 (2003), No. 1, p. 112-123.

[8] Okello, J.A., Watany, M., and Crolla, D.A., Theoretical and Experimental Investigation of Rubber Track Performance Models, *Journal of Agricultural Engineering Res.* Vol. 69 (1998), p.15-24.

[9] Ned, H.C., and Robert, J.H., Fundamental of Hydraulic Engineering System, Third Edition, Prentice-Hall International (UK) Ltd., London, 1996.

[10] Wong, J. Y. J., Radforth, R., and Preston-Thomas, J., Some futher studies on the mechanical properties of muskeg in relation to vehicle mobility, *Journal of Terramechanics*, 19(2) (1982), p.107-127.

[11] Ataur, R, Azmi, Y, and A K M Mohiuddin, Mobility investigation of a designed and developed segmented rubber track vehicle for sepang peat terrain in Malaysia, *Journal of Automobile Engineering*. Proceedings of IMech E Part D, Vol.221 (2007) (D7), p.789-800.

Proceedings of the 4th BSME-ASME International Conference on Thermal Engineering
27-29 December, 2008, Dhaka, Bangladesh

EFFECT OF WORKING FLUIDS AND EVAPORATOR GEOMETRY ON THE PERFORMANCE OF THERMOLOOP

Md. Ashraful Islam, Rayhan Ahmed, Sharif Md. Yousuf Bhuiyan
Department of Mechanical Engineering, BUET, Dhaka, Bangladesh
aislam@me.buet.ac.bd

Alam Mohammed
Alam Thermal Solutions Inc., USA
malam@alamthermal.com

ABSTRACT

Thermoloop, a highly promising electronic cooling system, is a pulsated two-phase thermosyphon (PTPT) comprising of evaporator, condenser, a liquid reservoir and two non return valves with associated tubing and fittings. This research is experimented on this thermoloop device to determine effects of working fluids and evaporator geometry on its performance. The performance of the thermoloop device was tested for Methanol, Ethanol and Water by varying the heat input and evaporator geometry. During the experiments the evaporator was kept filled and the condenser was cooled by a fan. For each heat input, evaporator wall temperatures, condenser inlet and outlet temperatures, liquid height at the reservoir have been recorded. From the data presentation and subsequent analysis it is found that the cycle time (time necessary to return the liquid back into the evaporator after first being evaporated in the evaporator, then condensed in the condenser and then reserved in a reservoir, which occurs in a periodic manner) limits the condenser performance and hence limits the performance of thermoloop. For a particular evaporator working with a specific fluid, the cycle time decreases with the increase in heat input, which causes a high mass flow rate through the device components. From experiments with different fluids, it is found that the cycle time depends on fluid properties viz. density, heat capacity, Latent heat of vaporization, surface tension, etc. From the experimental data a correlation has been proposed in this study to predict the cycle time for the thermoloop device.

Keyword: Thermoloop, Cycle time, two-phase thermosyphon.

1. INTRODUCTION

At present, while the world is looking for miniaturized electronic components with high higher power density, the high heat flux becomes one of the major concerning subjects. Major fields of thermal energy transfer include cooling of semiconductor devices, fuel-cells, electrical and electronic devices, air conditioning, solar energy collection, motor and engine cooling, manufacturing processes heat recovery and thermal management in outer-space structures, etc. All applications mentioned above look for a common requirement, which is to facilitate and control thermal energy transportation at higher heat flux level over longer distance while maintaining a moderate device temperature. Due to the size and design complexity, single phase liquid cooling is almost inconceivable in these cases. Considering all known phase-change heat transfer devices [1-3], the motive power behind the condensate

return has been derived mainly by one of two natural forces: gravity, used in thermosyphon and force of capillary action used in heat pipe. The thermosyphon is fully dependent on gravity and the major constraint of heat pipe is the relative weakness of capillary force, which can pull condensate through capillary passageway only very slowly, limiting the rate of thermal energy transfer. Thermoloop [4], a new concept to two-phase loop thermosyphon cooling system works independent on gravity or capillary action or any other external pumping system and can transfer thermal energy over a long distance, is a highly promising electronic cooling system with simple design dealing with very high heat requirements for electronic cooling.

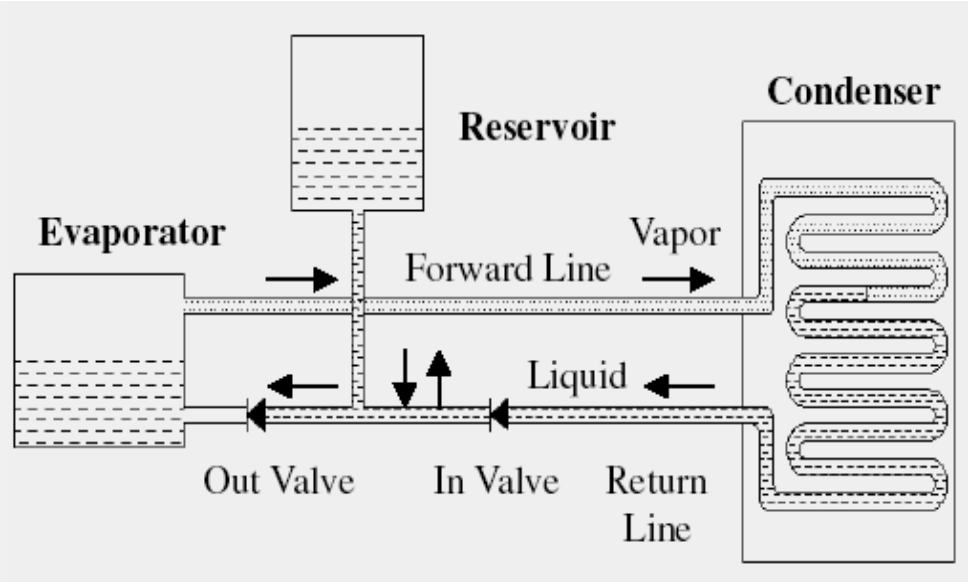

Figure 1: A Schematic of the thermoloop device

Unlike heat pipe or thermosyphon, the thermoloop device has two self-regulated flow controller (check valves) and an adjustable reservoir in addition to evaporator and condenser as shown in Fig. 1. Thermoloop device starts working automatically when the temperature at the evaporator wall slightly exceeds the boiling point of the working fluid. The device works periodically in two sequential and repeating states-Vapors Transfer State and Condensate Return State. With the help of flow controller and adjustable reservoir, this device can produce much stronger vapor transport and condensate return force, and therefore, enables very high heat flux capacity. Both states continue to repeat as long as the device is in operation. The device will automatically adjust its functionality (cycle frequency, volume occupied by vapor, rate of heat absorption and rate of heat dissipation) depending on the thermal load at evaporator, and the heat removal rate from condenser. In some previous studies [4-6] presenting key performance parameters and the effect of condenser convection on the performance of thermoloop device, the working principle of thermoloop device has been clearly described.

Day by day the loop thermosyphon becomes most favorable to researchers [7-12]. In this present study, experiments were performed for different fluids varying the heat input and evaporator geometry to determine the effects of working fluid and volume of fluid on the heat transfer performance of thermoloop such as cycle time, temperature of the evaporator, condenser inlet and outlet temperatures. The condenser convection was forced convection and kept unchanged for every experiment.

2. EXPERIMENT

A photograph of the experimental set-up used in this study is given in Fig. 2. For the thermo loop, two rectangular evaporators were used called prototype-1 & prototype-2. Prototype-1, made of Aluminum of outside dimensions 72.5mm× 60mm× 20mm, has an inside volume of 75 cc. and Prototype-2, made of copper of outside dimension of 77mm×65mm×8mm, has an inside volume of 25 cc. The internal surface of the both evaporator were grooved to facilitate the boiling enhancement. A condenser was made of externally fined copper tubes and was cooled by a fan. The outer tube diameter of the condenser coil was 7.3 mm. Total length of the coil was 1600 mm. The water capacity of the condenser was 25 cc. There were two flow control valves placed on either side of the adjustable reservoir at a distance of 5 cm each.

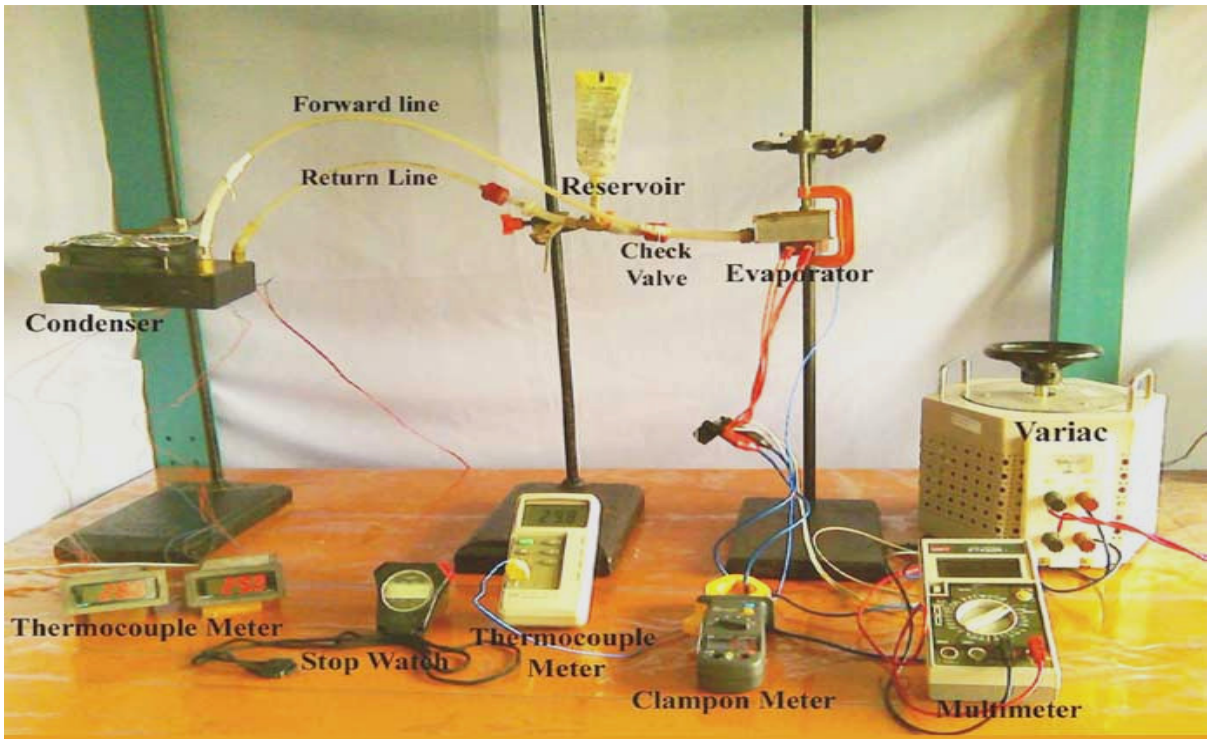

Figure 2: Front View of the experimental set up

The forward and return tubes both had an outside diameter of 6.35 mm (1/4 inch) and were 0.04 inch thick. The forward and return lines had the same total length, each being 56 cm long. A flexible cylindrical type reservoir with the size (maximum Dia.) 40 × 100 (length) mm^3 was connected in the return line at a distance of 40 cm from the condenser. The reservoir was closed type with inside volume $100cm^3$. The pressure drop across the check valve was 60mm of H_2O. The experiments were performed by Methanol, Ethanol and Water as the working fluid. The working fluids were injected using a syringe and the forward and return lines, and the condenser was completely filled. The fill ratio of the evaporator was 100% for different working fluids and Prototypes. Considerable care was taken to eliminate the formation of bubble or gas pockets in the forward and return lines and also in the condenser. Two cylindrical AC heaters, each of 200 watts were connected in parallel to the bottom of the evaporator. The heaters were connected using thermal interface material (Thermopile ®) to improve the thermal contact. Thermal load was varied by a variac. All the tests were carried out by placing the device horizontally (i.e. keeping the evaporator and condenser at the same level of elevation). A forced draft axial fan (average air velocity 4.75 m/s) was attached to the condenser for the forced convection condition. All the tests were

performed at an ambient temperature of 28 ± 2 ^{o}C. Thermocouple (K-type) was connected to evaporator and T-type thermocouples were connected to condenser inlet and outlet to measure the temperatures. During the experiment, for a heat input the temperature of the evaporator and condenser were recorded at a regular interval of 10 sec. For each fluid temperature of the evaporator, condenser inlet and condenser outlet were recorded for different heat inputs. Temperatures were also recorded changing the prototype. For different heat inputs the condenser outlet temperatures were considerer almost constant.

3. RESULTS AND DISCUSSION

In the present investigation, evaporator temperatures, condenser inlet and outlet temperatures were measured for different working fluids (Methanol, Ethanol and Water) and for different prototype by varying heat input. Mass flow rate from evaporator were also measured for different heat inputs. All the experiments were carried out keeping the evaporator fully filled and condenser convection condition at forced convection. The different heat inputs were 135W, 170W, 198W, 209W, 240W, 252W, 286W and 299W. Figure 3 illustrates the variation of temperatures with time for a heat input of 252 W. The temperature of the evaporator was observed to increase linearly with time up to the boiling point of the liquid, then became steady as boiling started. In the 1st cycle, temperature of evaporator rises from ambient temperature to the boiling point of the fluid and after the completion of the 1st cycle temperature of the evaporator drops 15-20^{o}C below the boiling point of the fluid and then again rises to the boiling point in the 2nd cycle. In the steady state condition minimum temperature of the evaporator (15-20^{o}C below the boiling point) is fully dependent on the condenser outlet temperature.

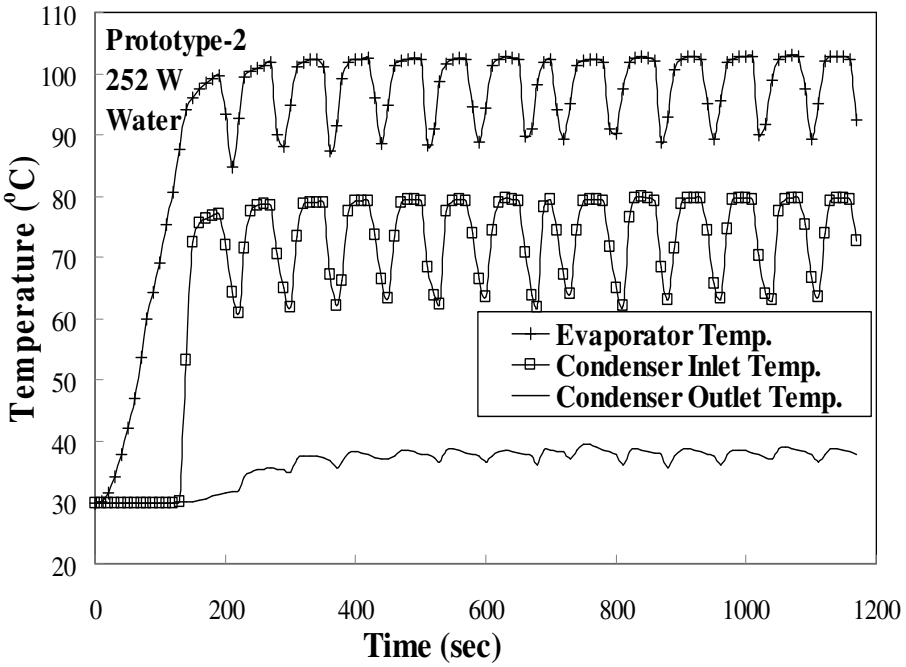

Figure 3: Variation of evaporator wall temperature, Condenser inlet and outlet temperatures with time

.

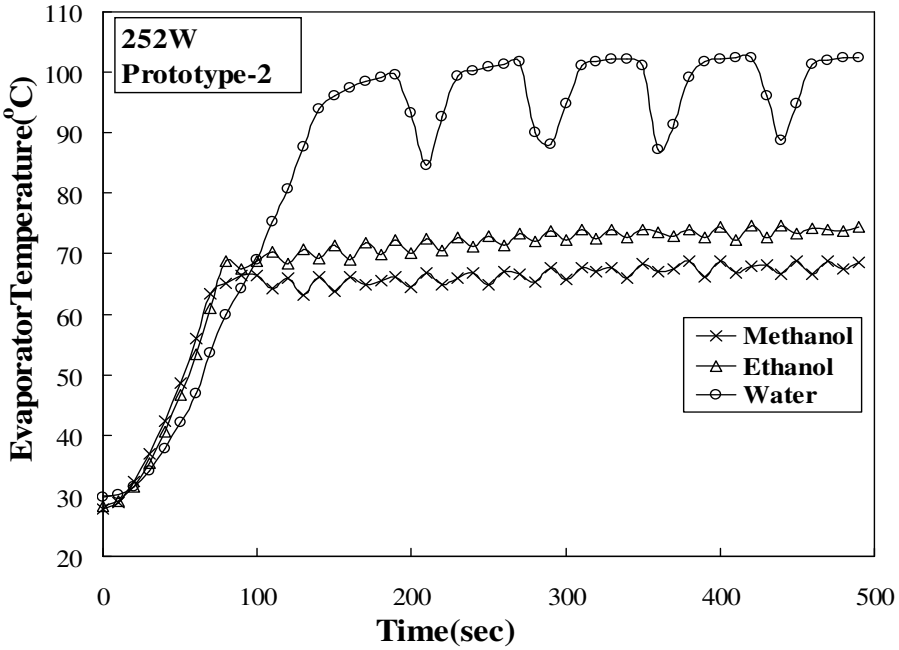

Figure 4: Variation of evaporator wall temperature with time for different working fluids

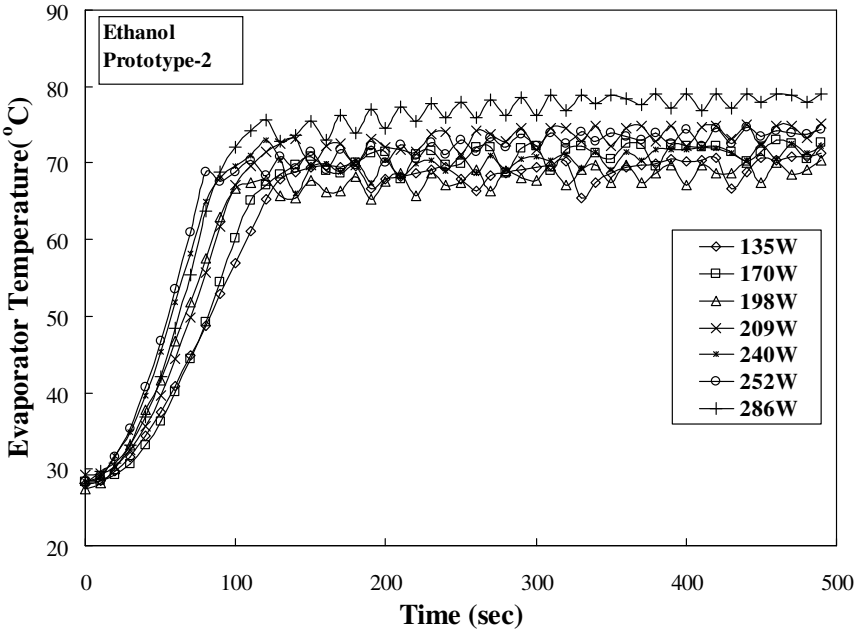

Figure 5: Variation of evaporator wall temperature with time for different heat inputs

3.1 Maximum Temperature of the Evaporator Surface

Figure 4 shows how the evaporator temperature varies with time for different working fluids for a particular heat input. From this study it is observed that the maximum temperature of the evaporator is greatly dependent on the boiling point of that fluid. The maximum temperature of the evaporator increases with the increase in boiling point of fluid.

Figure 5 exhibits the variation maximum temperature of evaporator for different heat inputs. It was observed that maximum temperature of the evaporator is independent on the volume of fluid and heat input. And the allowable range of heat input is fully dependent on the condenser capacity

3.2 Cycle Time

Figure 6 shows that for a particular fluid the cycle time decreases with the increase in heat input. In other words, less time is required to completely evaporate all the liquid for higher heat input. For the 1st cycle, the cycle completion time is maximum and in 2nd cycle it drastically reduces and after fluctuating in 3-5th cycle it becomes almost steady state from 6th cycle. Steady state cycle time decreases exponentially with the increase in heat input. Figure 7 exhibits how the steady-state cycle time varies with heat input for different fluids. For a small volume of fluid the state cycle time of methanol and ethanol are almost same and a clear distinction can be observed for large volume of fluid.

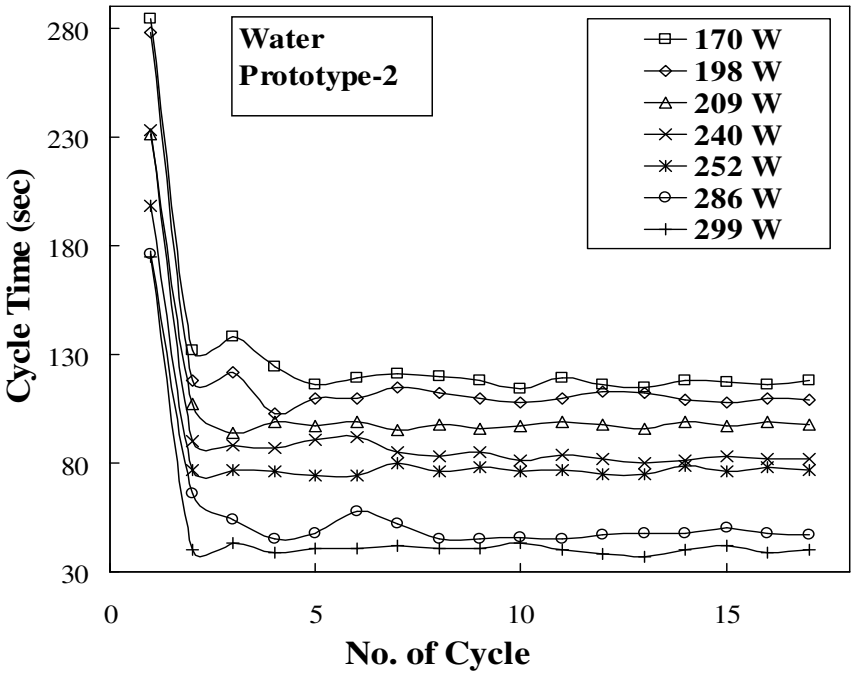

Figure 6: Variation of Cycle Time with No. of cycle for different heat inputs

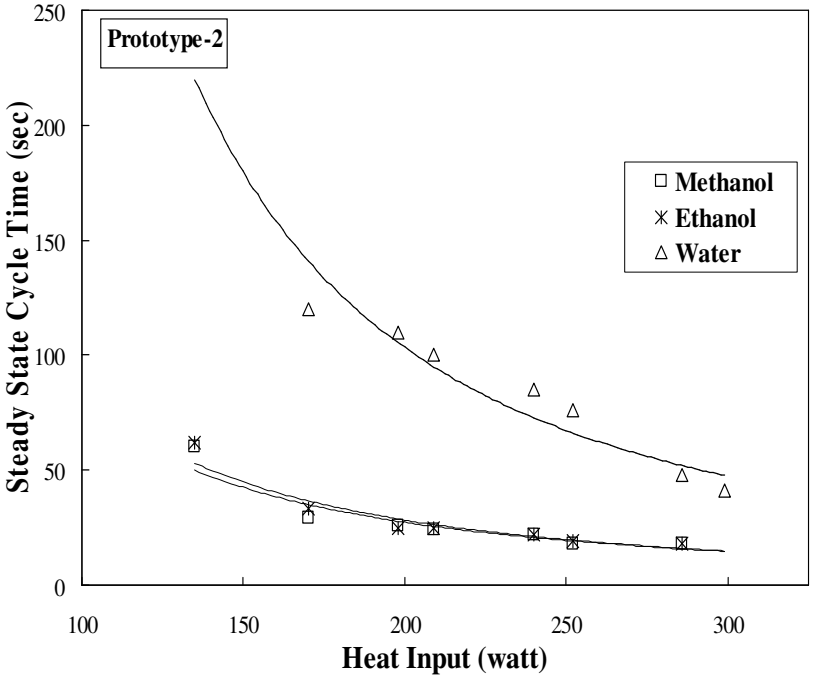

Figure 7: Variation of Cycle Time with heat input to the evaporator for different working fluids

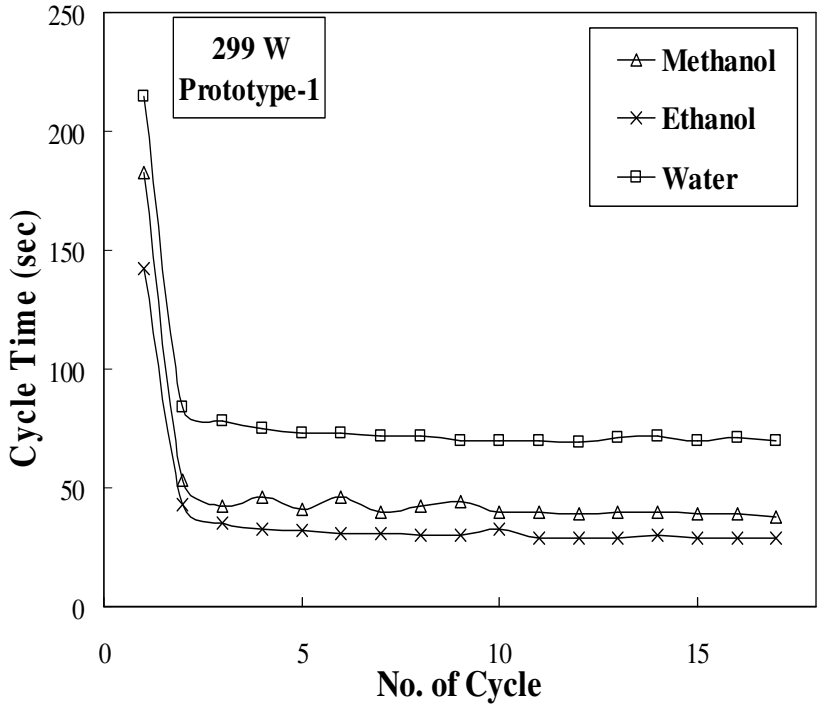

Figure 8: Variation of Cycle Time with No. of cycle for different working fluids

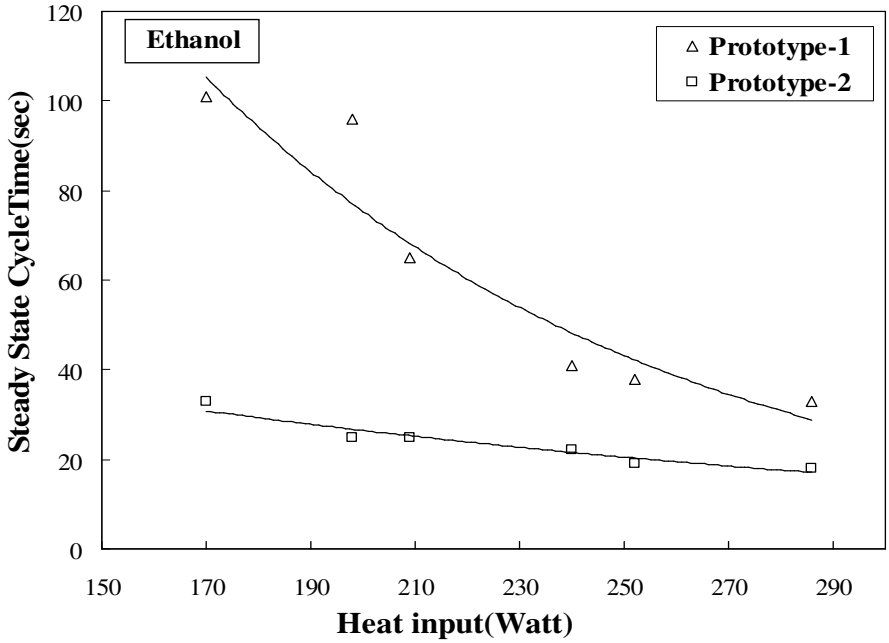

Figure 9: Variation of Steady State Cycle Time with different heat input

The cycle completion time greatly depends on working fluid as shown in Fig. 8. It was observed that it does not depend on the boiling point of the fluid. But from this study it is observed that cycle time for water is grater than that for methanol, again grater than that for Ethanol. Figure 9 shows how the fluid volume effects on the cycle time. For larger volume of fluid (for prototype 1) the cycle time is more and for smaller volume (for prototype 2) it is less as expected. From the experimental results and observation, it is found that the cycle time depends on density, latent heat of vaporization, viscosity, surface tension, buoyancy and volume of fluid in the evaporator. An effort has been made to establish a relationship to predict the cycle time from the experimental data for different working fluids. Dimensional

analysis does not help in choosing a suitable dimensionless group the cycle time. Following dependent variable (whose unit is that of heat flux, W/m^2) has been tentatively chosen to correlate cycle time with heat input, while Q/S has been taken as independent variable.

$$\frac{\rho_v H_{fg}\sqrt{\frac{\sigma}{g(\rho_l-\rho_v)}}}{t_c}$$

Where, t_c is the steady-state cycle time [s], ρ_l and ρ_v are, respectively, liquid and vapor densities [kg/m^3], H_{fg} is latent heat of vaporization [kJ/kg], σ is the surface tension [N/m], g is gravitational acceleration [m/s^2], Q is heat input [kW] and S is the heated surface area of the evaporator[m^2]. For Prototype-1, all the data for cycle time for all working fluids have been plotted in Fig. 10. The solid line in the figure is the curve shown by Eq. (1) and the dotted lines indicates ±30% deviation limit. It can be concluded that Eq. (1) can predict almost all data for the present experimental conditions within ±30% accuracy.

$$\frac{\rho_v H_{fg}\sqrt{\frac{\sigma}{g(\rho_l-\rho_v)}}}{t_c} = 0.47\frac{Q}{S} - 30.83 \qquad (1)$$

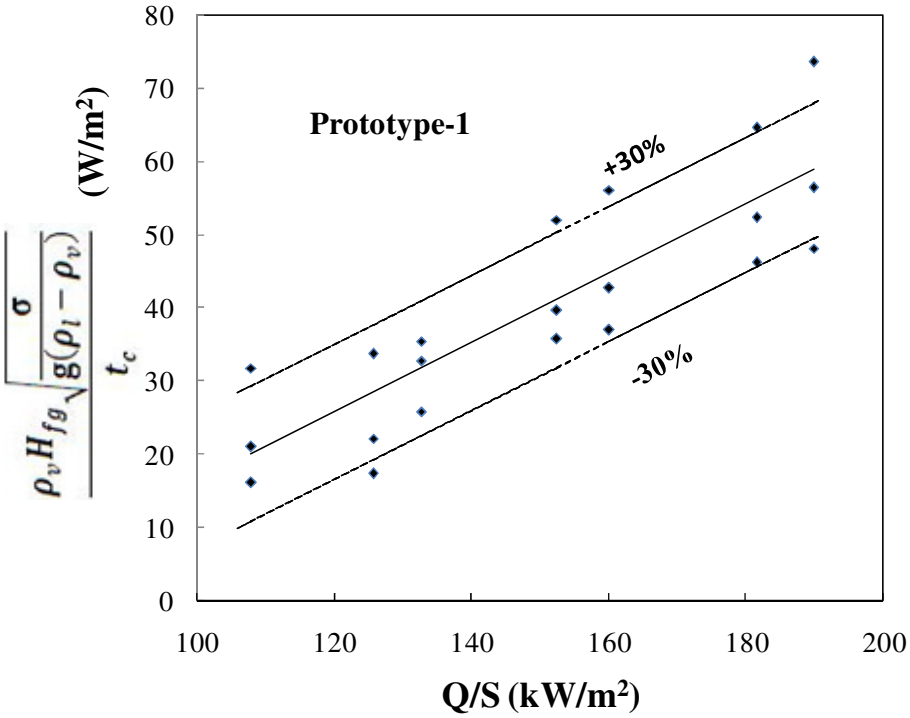

Figure 10: Performance of the correlation (1)

4. CONCLUSION

The experimental results on the thermoloop device have been presented by the variation of working fluids in the evaporator with 100% fill ratio, and by the variation of evaporator geometry. From the presentation of experimental data and their subsequent analysis, following conclusions are drawn.

(i) The maximum temperature of the evaporator varies with the working fluid. For heat input 299 W the maximum temperature for water was 106^{o}C, for ethanol was 80^{o}C and for methanol was 68^{o}C. It was found independent on the evaporator geometry.

(ii) For a particular heat input, the initial cycle time was always higher than its steady-state value for all working fluids. For a heat input of about 250 W working with methanol, the initial cycle time was 188 s while its steady-state value was 58 s.

(iii) The steady state cycle time decreases with the increase of heat flux in the evaporator and greatly depends on the thermo-physical properties of the working fluid. The values of cycle time for different working fluids can be predicted well by Eq. (1).

ACKNOWLEDGEMENT

This material is based on the research sponsored by the Air Force Research Laboratory, under agreement number FA4869-08-1-4029. The U.S. Government is authorized to reproduce and distribute reprints for Governmental purposes notwithstanding any copyright notation thereon.

5. REFERENCES

1. Maydanik, Y.F., "Loop heat pipes- theory, experimental developments and application", KN-19, 13th International Heat Transfer Conference, 13-18 August, 2006, Sydney, Australia.
2. Kawaji, M., Nikkanen, K. and Lu, C.G., "Experimental study of performance of looped and unlooped pulsating heat pipes", EQP-34, 13th International Heat Transfer Conference, 13-18 August, 2006, Sydney, Australia.
3. Wang, S. and Nishio, S., "Heat transfer performance of a closed oscillating heat pipe", EQP-38, 13th International Heat Transfer Conference, 13-18 August, 2006, Sydney, Australia.
4. Alam, M., "Thermoloop heat transfer technology", 9th AIAA/ASME Joint Thermophysics and Heat Transfer Conference, 5-8 June 2006, San Francisco, California.
5. M. A. Rahman, M. A. Islam and A. Mohammed "Performance study of thermoloop: Effect of evaporator fill ratio and condenser condition", International Conference on Mechanical Engineering 2007 (ICME2007), 29- 31 December 2007, Dhaka, Bangladesh.
6. M. A. Islam, M. A. Rahman and A. Mohammed "Heat Transfer Performance Of A Pulsated Two-Phase Loop Thermosyphon", 2008 ASME International Mechanical Engineering Congress and Exposition, October 31-November 6, 2008, Boston, Massachusetts, USA.
7. Mortazavi, H. R., Tuma, P.E., "Indirect Thermosyphons for Cooling Electronic Devices", Electronics Cooling, Vol. 15, No. 1, February 2006.
8. Khrustalev D., "Loop Thermosyphon for Cooling of Electronics", Thermacore Inc. Notes 2002.
9. Palm, B., Tengbald, N., "Cooling of Electronics by Heat Pipes and Thermosyphons- A Review of Methods and Possibilities", Proceedings of ASME Nat. Heat Transfer Conference, Houston 1996.
10. Pal, A., Joshi, Y., Beitelmal, M. H., Patel, C. D., Wenger, T., "Design and Performance Evaluation of a Compact Thermosyphon", Proceedings of the United Engineering Foundation, Thermes, Santa Fe, New Mexico, January 2002.
11. Filippeschi, S., "On Periodic Two-Phase Thermosyphons Operating Against Gravity", International Journal of Thermal Sciences, Vol-45, pp. 124-137, 2006.
12. Fantozzi, F., Filippeschi, S. and Latrofa, E. M., "Upward and Downward Heat and Mass Transfer With Periodically Operating Loop Thermosyphons", Superlattices and Microstructures, Vol-35, pp. 339-351, 2004.

Proceedings of the 4th BSME-ASME International Conference on Thermal Engineering
27-29 December, 2008, Dhaka, Bangladesh

EFFECTS OF TOWERS ON AERODYNAMIC PERFORMANCE OF WINDMILL

Harun Chowdhury[1], Daniel Wood[1], Firoz Alam[1] and Md. Tazul Islam[2]

[1]School of Aerospace, Mechanical and Manufacturing Engineering, RMIT University, Melbourne, AUSTRALIA

[2]Department of Mechanical Engineering, Chittagong University of Engineering & Technology, BANGLADESH

E-mail: harun.chowdhury@rmit.edu.au

ABSTRACT

Wind mill is widely used to produce mechanical power for a range of applications including water pump. This type of wind mill is often called wind pump with a rotor with several blades, a mechanical drive to actuate the pump, a rotary or translatory pumping mechanism and a tower. The primary objective of this work was to study the effects of tower location and configuration on aerodynamic efficiency of a scaled model wind pump. The aerodynamic measurements were conducted in RMIT Industrial Wind Tunnel for a range of wind speeds and tower configurations. The results indicated that tower positions have little effects on aerodynamic efficiency of a wind mill. However, shroud around the impeller has significant impact on wind mill aerodynamic characteristics.

Keywords: *Wind mill, tower, rotor, blade, aerodynamic.*

1. INTRODUCTION

A wind turbine converts the wind power into electricity. On the other hand, a windmill usually converts the wind power into mechanical power. A series of studies have been conducted on wind turbines and their findings were reported in the public domain; however the vast majority of these studies were on 'Megawatt Towers' [1, 2, 3]. These towers have been developed with the aim of producing Megawatts of electricity in appropriate conditions, these are in contrast to experimental study of wind-mills that have had little recorded research or any evidence of progress made in the past decade.

Wind pumps are widely used for pumping water. It can provide a practical alternative to power generators in remote and isolated areas. The United States, India, Australia and South Africa have been utilising the benefits of wind pumps since long and it is hard to see them being replaced in the near future. They have become an indispensable tool for the rural landscape in many countries [5, 6].

Currently, wind turbines are being used increasingly in industrialized nations for the generation of 'green' power (electricity) and its sole benefit is the creation of energy without greenhouse gas emission during its working life. This is in contrast to a thermal power or nuclear power generator that is dependant on fossil energy and/or radioactive materials.

Recently, Germany has invested heavily to generate over 7600 MW power using wind turbines. It is he biggest feed-in wind power sources in Europe. Germany produces around

1327 MW yearly with approximately 18% of capacity. However, the minimum output was 8 MW at that period a rush for substitute power was required. In comparison, wind powered water pump for the agricultural use does not require grid power when no wind blows as long as the wind pump can continue its function on a regular basis. However, the wind turbines for grid power generation need a constant and reliable wind all the time.

2. WIND MILL DESIGN

Various types of wind turbines and wind mills have been designed and manufactured around the world. As far as wind turbines concern, it is widely believed that the Horizontal Axis Wind Turbine (HAWT) is better for converting wind energy to electrical or mechanical energy. It is not only the cheapest but also most efficient and robust. The other option is Vertical Axis Wind Turbine (VAWT) however it is more costly and less robust compared to HAWT.

There are two distinct types of wind mill widely used in domestic applications. They are: a) lift type, and b) drag type. The lift type tends to use an airfoil to create lift as the wind passes and therefore rotates due to the lift generated by the airfoil. In contrast, the drag type can use many types of shapes of blades but they all rely on the same principle, that the drag caused by the wind will create the movement which is used to generate useful work. Lift machines have proven to have a greater efficiency in general along with providing less noise and a more reliable life.

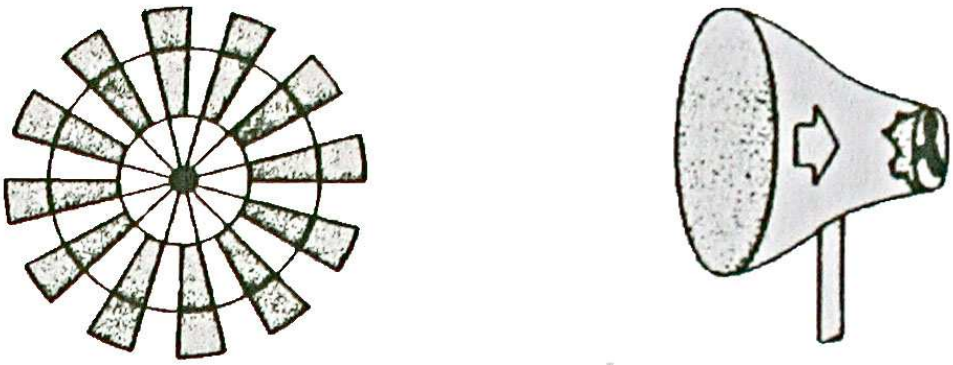

(a) US farm windmill (multi bladed) (b) Concentrator

Figure 1: Types of wind mills [5]

2.1 Wind Mill Design

To conduct aerodynamic measurements in RMIT Industrial Wind Tunnel, a scaled model of a multi bladed wind mill was designed and constructed based one a commercially available US farm type multi bladed Southern Cross wind turbine. The diameter of the rotor was 765 mm and the tower height was approximately 1000 mm which made the total height of 1500 mm. The dimensions were selected such that the airflow from the rotor and tower would not be disturbed by the walls of the wind tunnel. The dimension of RMIT Industrial Wind Tunnel is approximately 3000 mm (wide), 2000 mm (height) and 9000 mm (long). The shape of the blades required to give a low starting speed and high torque, but the most dictating feature

was that the blades needed to be simple to create and contain a consist twist, as to give an even rotating wake upon which to compare the effects of different experiments.

Through trial and error, the most easy and convenient construction material was found to be PVC drain pipe of 150 mm diameter. Eight (8) blades were cut out of almost identical proportions. This would help with both balance and maintaining a consistent wake for wind tunnel testing. Eight Blades were given greater start-up torque (lowest start up speed) to make sure that a good range of wind speeds was found in wind tunnel experimentation. Any more blades would have compromised the structural integrity of the central hub and at some speeds the blades could disturb or merge wakes. Figure 2 shows the manufactured scaled wind mill with 8 blades.

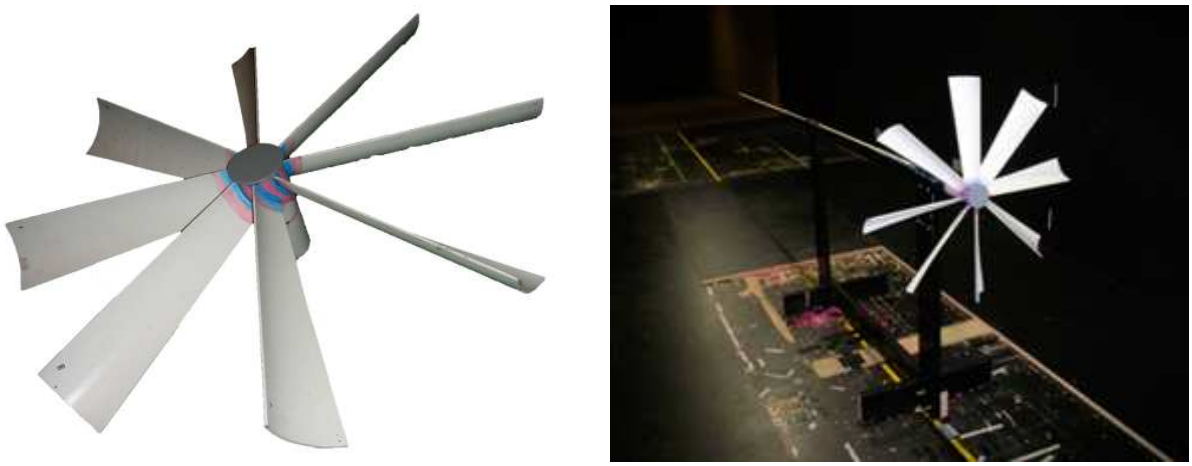

Figure 2: Model wind mill rotor with multi blades

2.2 Tower Design

There are three main tower designs commonly used for wind turbines and windmills. They are:

a) Guyed mast,
b) Lattice tower
c) Free standing tubular tower

These designs are shown in Figure 3.

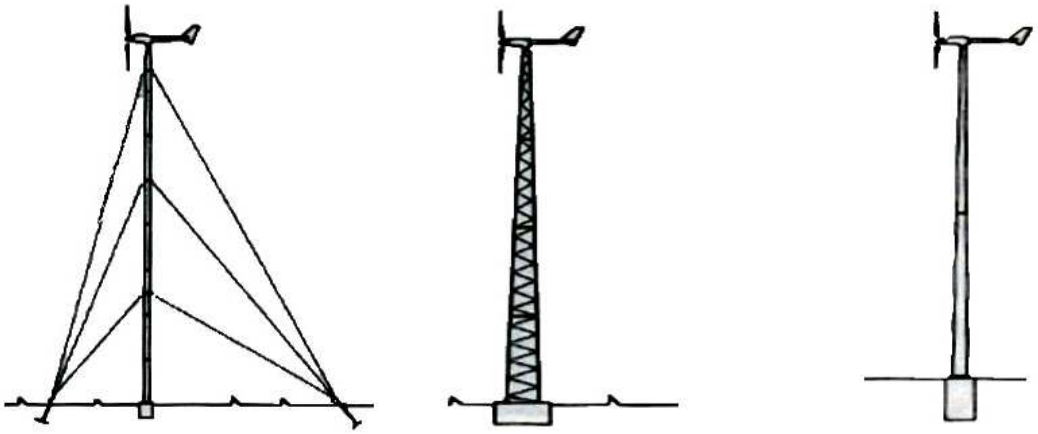

(a) Guyed mast (b) Lattice tower (c) Free standing tubular tower

Figure 3: Various Towers Design [2]

The Guyed mast design, as used on a great deal of micro turbines but not seen on conventional pumps, is cheap and easy to erect. The guyed mast requires regular maintenance and the cables need to be tensioned correctly and the anchors need to be checked for movement, along with any other basic wear issues. It can be lowered for maintenance to the rotor or other head parts.

In contrast, the Lattice tower design is used by Southern Cross on their windmills and provides a steel structure and allows mechanical power to pass down the centre of the tower via a pusher puller or rotating shaft. This structure although expensive requires little maintenance throughout its life and can be the strongest per weight of the available designs. It also provides a perfect base for a ladder to be climbed for head maintenance. The lattice can cause noise problems and create unwanted turbulence if the rotor is behind or near to the tower.

The Free standing tubular tower is used most often for the megawatt towers. It is very expensive to build but can be the strongest and heaviest. It provides the least noise and turbulence as well as needing only crack checking for maintenance. Although an exterior ladder is a disadvantage for both strength and turbulence.

It is no doubt that a mechanical driven pump would seem appropriate for a Lattice type structure unless a method of transferring power could be innovated which does not obstruct rotation with the Guyed. Whilst a Guyed post or Lattice type would seem the most appropriate for an electric wind turbine style of windmill, depending on durability and maintenance requirements.

3. EXPERIMENTAL SET UP IN RMIT INDUSTRIAL WIND TUNNEL

Two different towers namely lattice tower and free standing tubular tower were used in this study. Their positions were varied as shown in Figures 4 to 6.

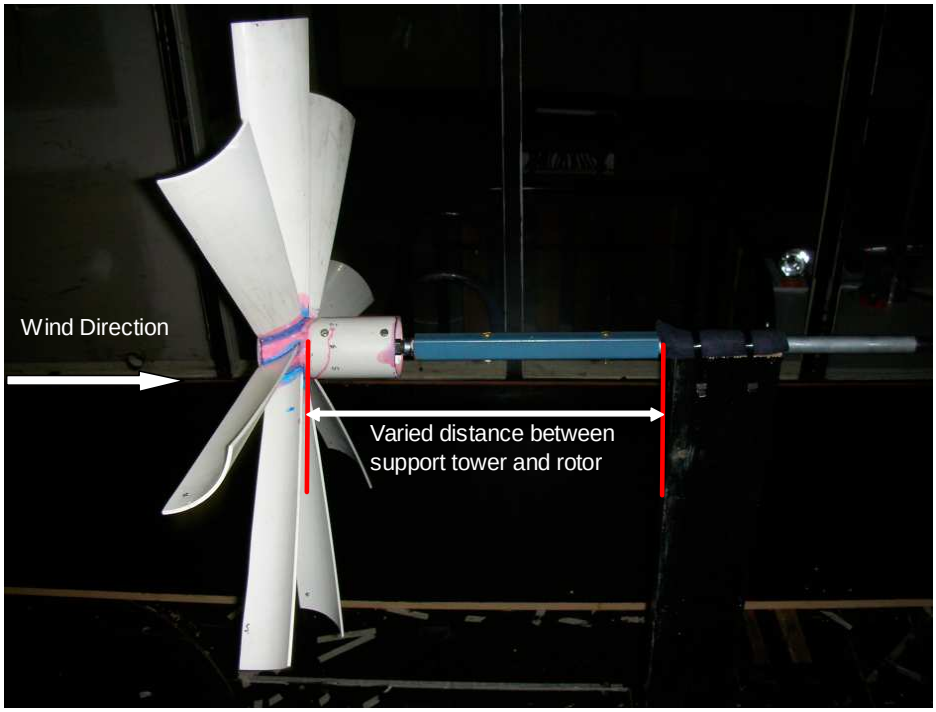

Figure 4: Rotor mount in RMIT Wind Tunnel

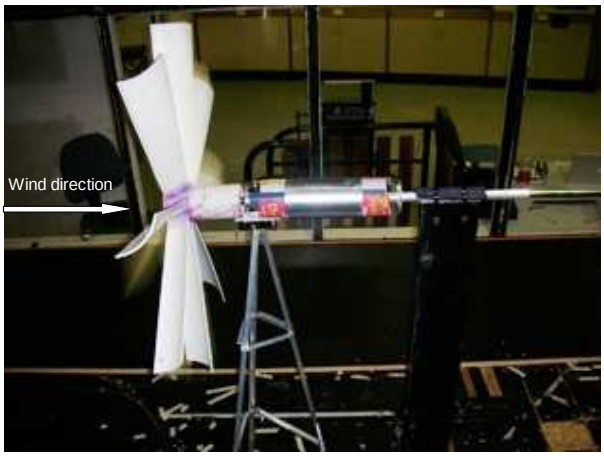

a) Scaffold Behind (100mm)

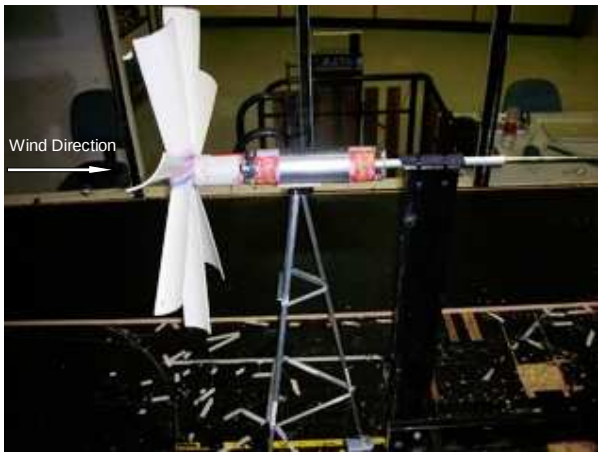

b) Scaffold Behind (200mm)

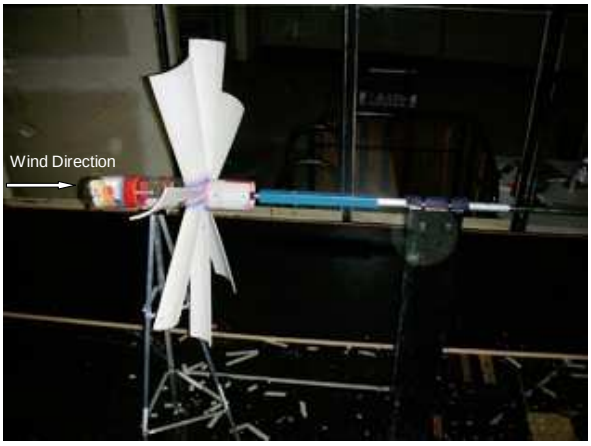

c) Scaffold Front (100mm)

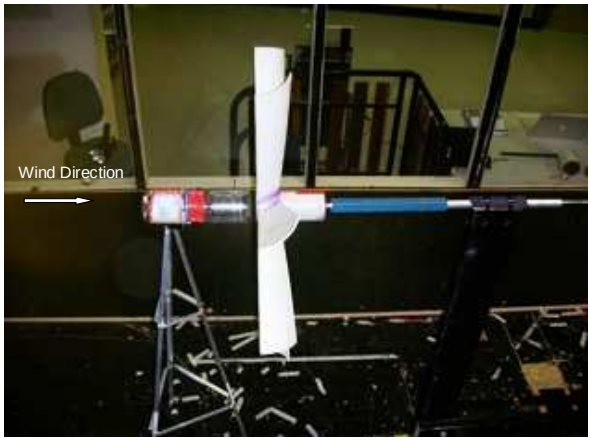

d) Scaffold Front (200mm)

Figure 5: Position variation of lattice tower

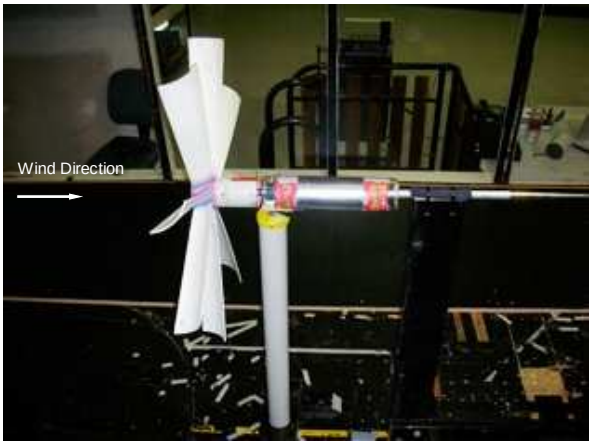

a) Post Behind (100mm)

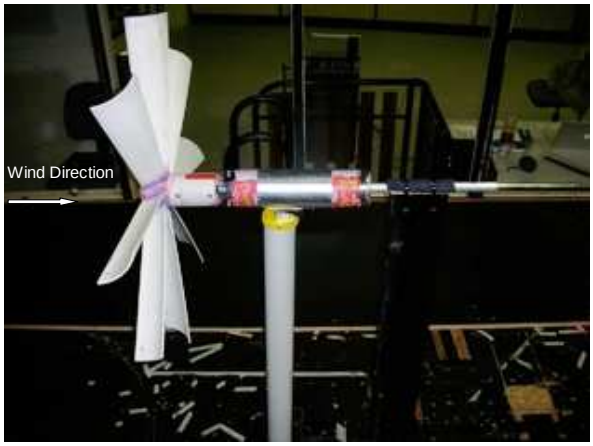

b) Post Behind (200mm)

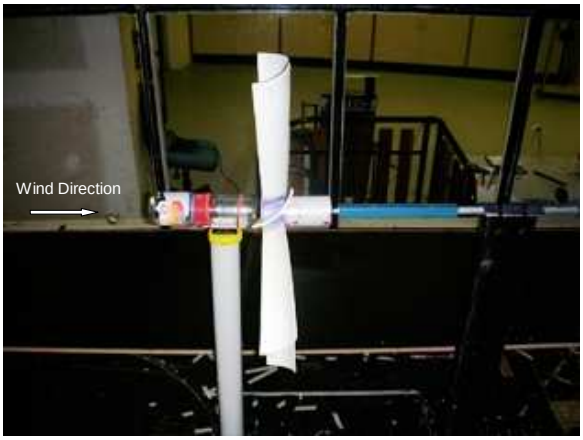

c) Post Front (100mm)

d) Post Front (200mm)

Figure 6: Position variation of tubular tower

In order to see the effects of shroud, two shrouds: one stationary and other rotary were made as shown in Figure 7.

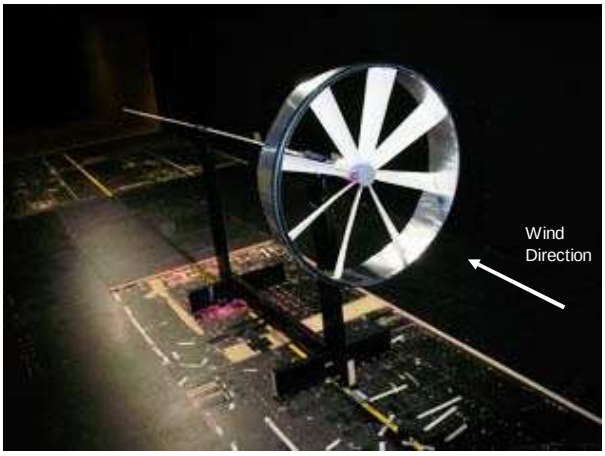

a) Rotating Shroud (Tower Distance 107mm)

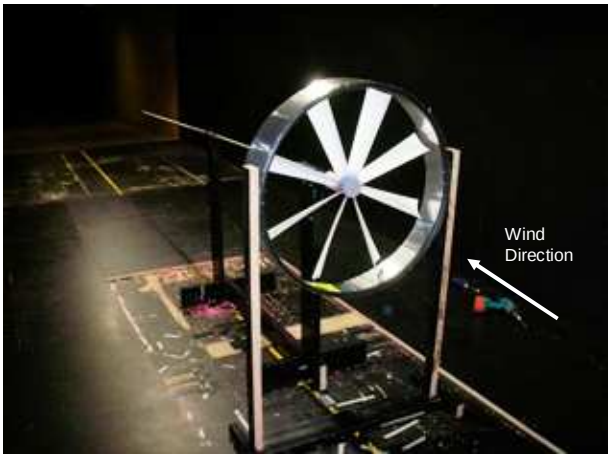

b) Stationary Shroud (Tower Distance 107mm)

Figure 7: Rotating and Stationary Shroud

4. RESULTS AND DISCUSSION

The rotational speed of rotor (determined by the electronic tachometer) as a function of the tunnel wind speed with 3 positions (locations) of the cylindrical tower is shown in Figure 8. It is evident that the position of tower immediately behind the rotor has some effect. However, with an increase of distance behind the rotor, no significant effect was noted (see Figure 8). At low speeds, the close proximity of cylindrical tower can reduce the rotor speeds up to 20 to 15 rpm (between 5 and 15 km/h) and on average of 10 rpm at higher speeds. The loss of the rotational speed of the rotor is believed to be due to the presence of the tower in the wake of the rotor.

Figure 9 illustrates the effects of scaffold type tower position behind the rotor on rotational speed of the rotor and the wind speed. As the scaffold allows passing air with minimum air resistance, the effects of location of the tower position are negligible as expected.

The effects of tower placements (locations) in the front and the rare of the rotor are shown in Figure 10. It indicates that there is no significant variation of rotor speeds due to the same distance location of both types of towers back and forth of the rotor. However, more investigations are needed to clarify the statement as it was believed that there could be some variations between the two towers.

Figure 11 shows the effects of stationary (fixed) and rotary (moving) shrouds which were used around the rotor blades. It is clearly evident that the moving shroud generates more aerodynamic interference on the airflow of the blades. As a result, a significant reduction of rotor speed was noted. The reduction is more with in an increase of tunnel wind speeds (see Figure 11).

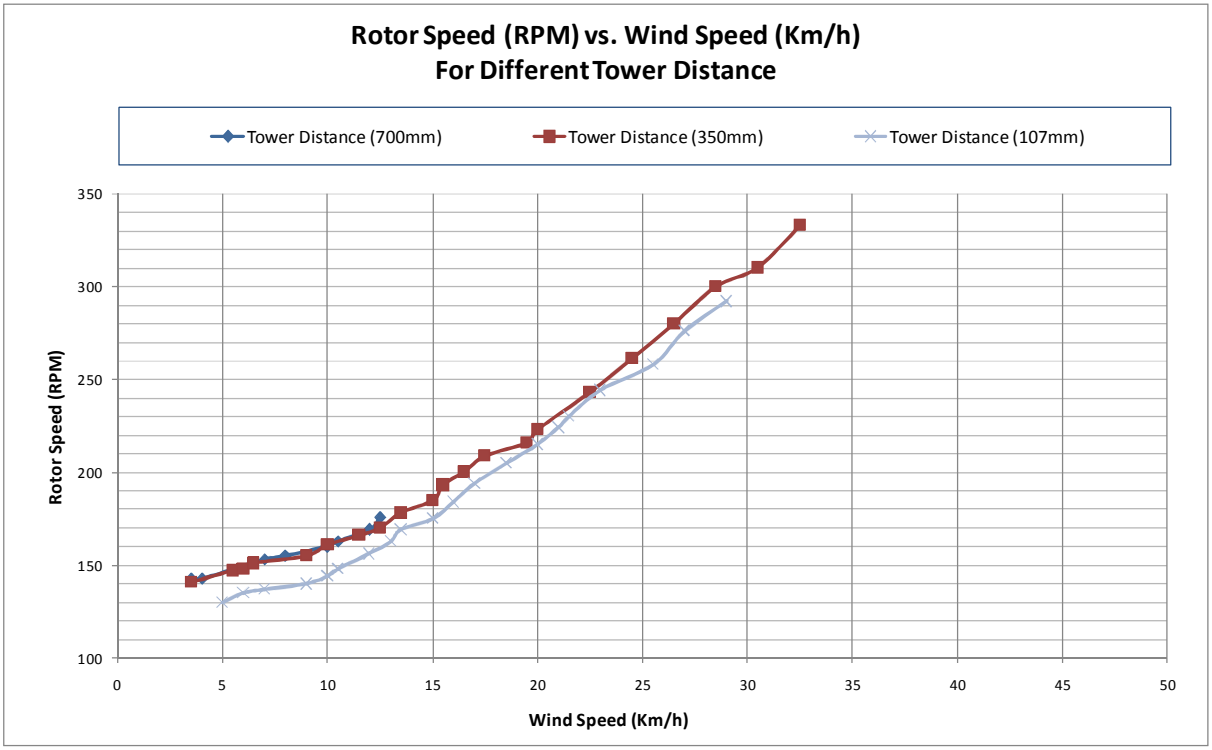

Figure 8: Rotor speed at different tower distances

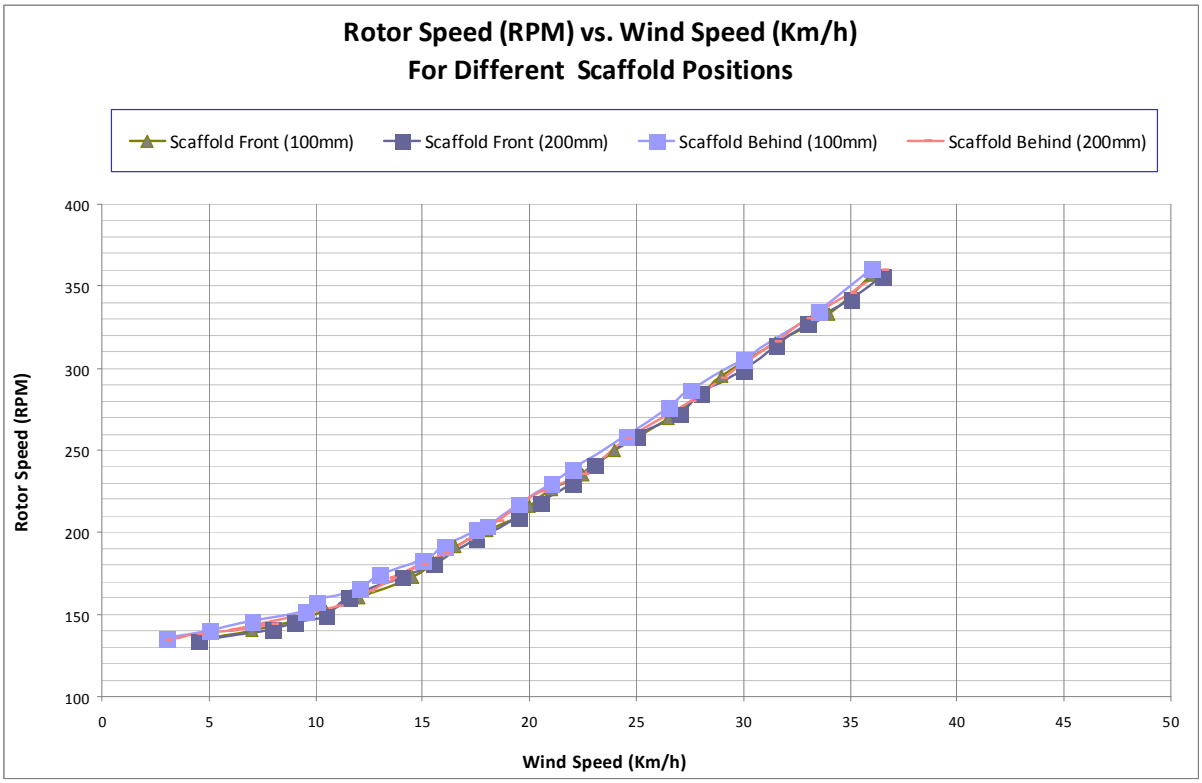

Figure 9: Rotor speed at different scaffold positions

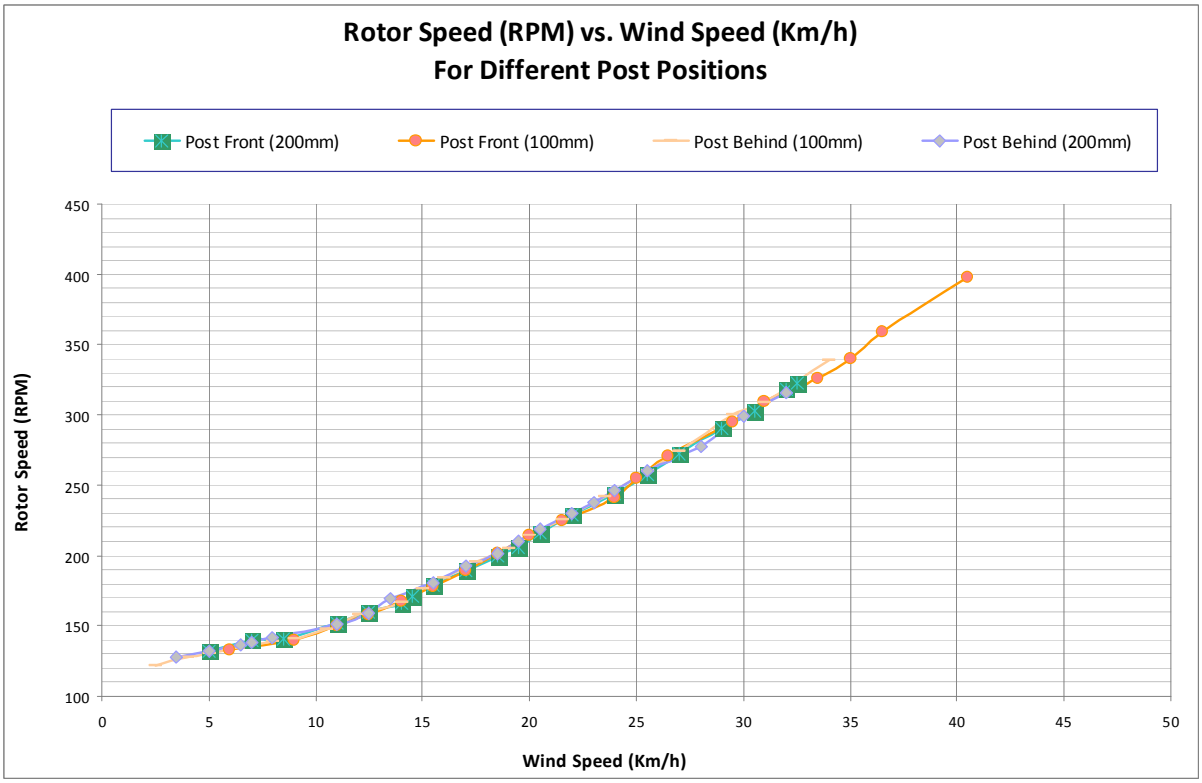

Figure 10: Rotor speed at different circular cross-sectioned post positions

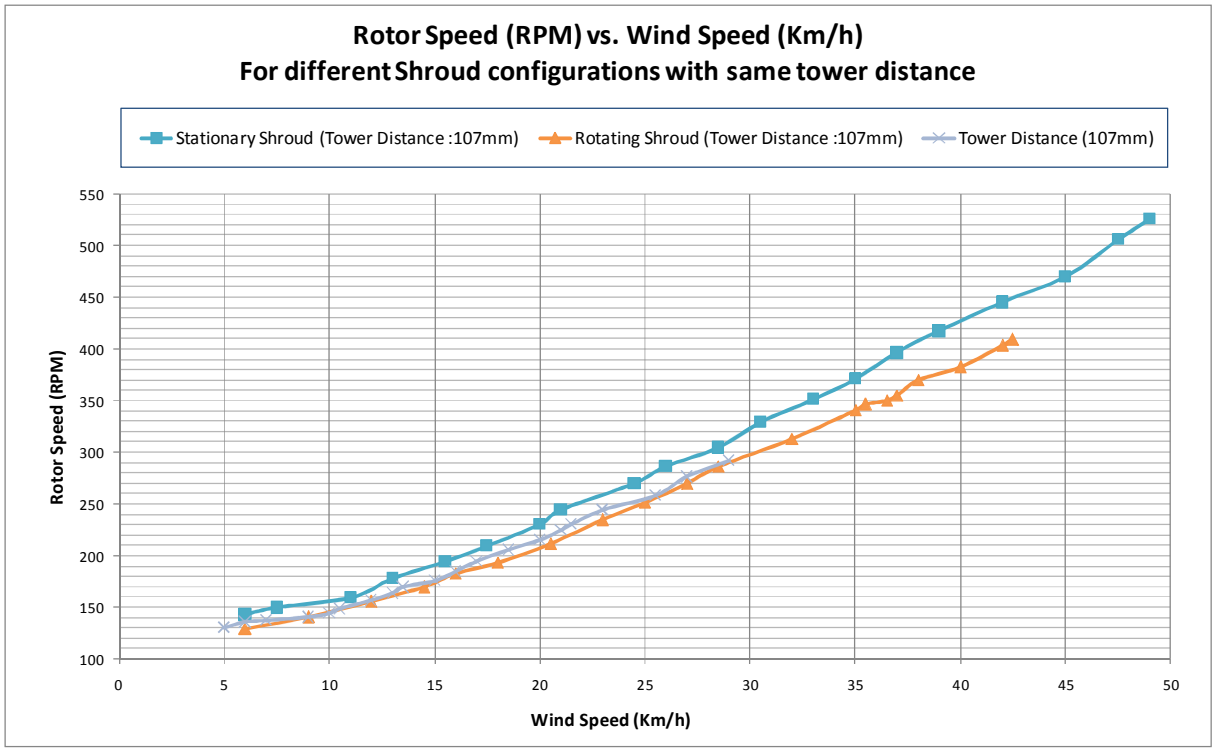

Figure 11: Rotor speed at different circular cross-sectioned post positions

6. CONCLUSIONS AND RECOMMENDATIONS

The following conclusions were made from the work presented here:

- The tower position immediately behind the rotor decreases rotor's rotational speed however the position has negligible effect if it is outside of the blades wake.
- The rotor speed can be significantly affected by the use of different types of towers within the vicinity of the blades.
- The shroud can have significant impact on rotor speeds depending on shroud's fixture (stationary or rotary)
- Blades number can play an important role in aerodynamic efficiency. Therefore, it would be worthy of further investigation of the blade number effects on rotor rotational speeds.
- The effects of rotating shroud must be investigated at higher speeds which was not possible in this work due to some structural rigidity problems.

ACKNOWLEDGEMENTS:

The authors would like to express their thanks to technical staff of the School of Aerospace, Mechanical and Manufacturing Engineering, RMIT University, Melbourne, Australia.

REFERENCES

[1] Kovarik, Pipher and Hurst, Wind Energy, Domus Books Inc., 1979

[2] Manwell, McGowan and Rogers, Wind Energy Explained Theory Design and Application, John Wiley and Sons Ltd., 2000

[3] Makund R. Patel, Wind and Solar Power Systems, CRC press LLC, 1999

[4] Gasch, R and Twele, J., Wind Power Plants, fundamentals, Design, Construction and Operation, Solarpraxis Publishing, 2002

[5] Gipe, P, Wind Energy Basics: A Guide to Small and Micro Wind Systems, Chelsea Green publishing company, 1999

[6] Steel, D., Wind Energy, Building the 10%, Professional Engineering Publishing, 2001

Proceedings of the 4th BSME-ASME International Conference on Thermal Engineering
27-29 December, 2008, Dhaka, Bangladesh

APPLICATION OF GENITIC ALGORITHM FOR SHAPE OPTIMIZATION OF 2D PLANER DIFFUSER

Suman Ghosh ,Dilip Kumar Pratihar, Biswajit Maiti, Prashanta Kumar Das

Department of Mechanical Engineering
Indian Institute of Technology
Kharagpur-721302, India
Phone-+91-3222-282992
Email : sumanghosh@mech.iitkgp.ernet.in

ABSTRACT

The shape of a 2D planar symmetric diffuser handling incompressible turbulent flow, is optimized by using a Genetic Algorithm (GA) coded with C programming language. For a prescribed inlet velocity and outlet pressure the shape of the diffuser is optimized in such a way that the pressure loss across the inlet and outlet become minimum. Commercial CFD software Gambit and Fluent is used for hydrodynamic analysis. For fully automated operation, CFD software and GA are combined in a monolithic platform by a computational algorithm.

KEYWORDS: *Incompressible Flow; Optimization; Genetic Algorithm; Gambit; Fluent.*

1. INTRODUCTION

Shape optimization is a classical problem. From the engineering point of view, the main motive for the optimum design has been a reduction in the initial cost, operating cost or the both under a set of constraints, which are dictated by the diverse parameters like process requirements, available infrastructure, safety, environmental concern etc. Based on the above goal, a set of design variables is optimized. As the present work is concerned with the optimum design of a fluid flow system, a brief overview of some of the shape optimization exercises in fluids engineering is given below.

A large volume of work had been carried out on shape optimization of fluid flow systems relevant to aerodynamics applications[1,2]. Falco[3] carried out optimization of aerofoil shapes using evolutionary algorithms. Multi-objective design optimization in aerodynamics and electromagnetics was conducted by Makinen et al. [4]. Several non-linear optimization problems related to general fluid flow had been solved using gradient-based optimization tools by various investigators [5-9]. A flow solver and a mathematical optimization tool (implementation of a trust region-based derivative-free method) were combined and used as an integrated procedure by Lehnhauser and Schafer [10] for the shape optimization of a fluid flow domain.

Diffusers are integral parts of many flow systems. An improperly designed diffuser may lead to flow separation and excessive consumption of pumping power. It may also produce a flow mal-distribution in the downstream, which is not acceptable in many applications. As a result, designing the optimum shape of a diffuser had been the subject of investigation for many researchers during the last decade. Optimum design of a straight-walled diffuser was

obtained by Kline et al. [11]. The performance of a straight two-dimensional diffuser had been studied and analyzed by Reneau et al. [12]. The effect of wall shape on flow regimes and performance had been studied in a straight two-dimensional diffuser by Carlson et al. [13]. The profile of a plane diffuser with given upstream width and length had been optimized to obtain the maximum static pressure rise by Cabuk et al. [14]. The stedy-state Navier Stokes equation was used to model the flow through the diffuser considering two-dimensional, incompressible and laminar flow. Geometries for three-dimensional viscous flow had been optimized by Svenningsen et al. [15], applying quasi-analytical sensitivity analysis. A response surface technique had been used to optimize the shape of a two-dimensional diffuser subjected to incompressible turbulent flow by Madsen et al. [16]. Growth-Strain Method was used for shape optimization in a flow system by Maeng and Han [17]. A diffuser had been optimized using the Support Vector Mechanics (SVM) by Fan et al. [18]. The SVM was used to construct a response surface. Shape optimization was carried out by Goel et al. [19] to improve hydrodynamic performance of diffuser vanes.

Gradient-based techniques and direct search techniques are two powerful methodologies of optimization [20]. In direct search, the search starts with randomly generated initial solutions and the final optimal solution might depend on the chosen initial solutions. The gradient-based method cannot be applied for a problem involving discontinuous objective function space. Moreover, the chance of the gradient-based method for getting stuck at the local extremum is more. Genetic Algorithm (GA) is a generic and robust search technique, which generally does not suffer from the above limitations. GA is a population-based search and optimization tool, which loosely mimics genetic evolution after following the principle of natural selection [21]. It starts with a population of solutions selected at random. The solutions are modified iteratively using several operators, namely reproduction, crossover and mutation. It provides several near optimal solutions, which offer the designer sufficient flexibility. The use of a GA coupled with a CFD-based modeling possesses enough promise to solve shape optimization of systems involving fluid flow.

2. PROBLEM DEFINATION

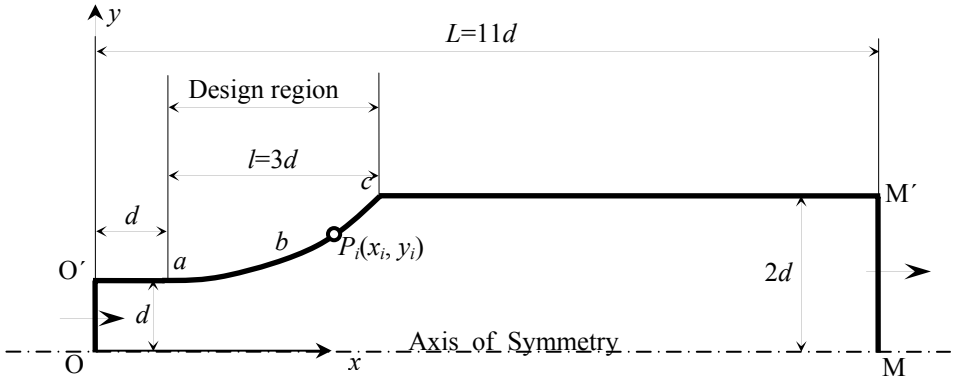

Figure 1: Symmetric half of a plane symmetric diffuser.

A symmetric two-dimensional planar diffuser (schematically shown in Fig. 1) is considered for the present problem. An incompressible fluid enters the domain of the diffuser with a uniform velocity. The flow through the diffuser is assumed to be fully turbulent with Reynolds number of 10^5, based on the inlet half-width of the diffuser d. The other dimensions of the diffuser are shown in the figure. The model considers symmetry condition along the channel axis. The main objective of the present problem is to finding out the appropriate shape of the curve *abc* to get the maximum static pressure recovery. A non dimensional pressure recovery factor C^*_p is defined as

$$C_p^* = \frac{\Delta p}{\frac{1}{2}\rho v_{inl}^2} \tag{1}$$

where Δp represents the static pressure rise, ρ indicates the density of the fluid and v_{inl} denotes the inlet velocity of fluid flow. Therefore, the problem boils down in finding out the appropriate shape of the curve *abc* (refer to Fig. 1) to give the maximum value of C^*_p.

3. METHODOLOGY

Methodology has three main parts. Hydrodynamics for a given shape of diffuser has been solved by using the CFD software Gambit[23] and Fluent[22] for calculating the objective function C^*_p for that particular shape of the diffuser. An optimization algorithm (GA in the present case) has been designed to optimize the objective function for the given set of constraints. To combine the CFD software with the GA programming in a monolithic platform for a fully automated operation a computational algorithm has been designed.

Within the hydrodynamic calculation, the mass and momentum conservation equations along with appropriate boundary conditions for a given geometry of the diffuser has been solve by commercial CFD software Gambit[24] and Fluent[23]. The standard k-ε model [25] with standard wall function has been used for turbulence modeling. The velocity inlet (OO′ in Fig. 1) boundary condition is considered, while a pressure outlet condition relaxing to atmospheric pressure is imposed at the exit (MM′ in Fig. 1). The symmetry condition is applied at the bottom boundary (O′M′ in Fig. 1) and wall condition is used on the top boundary (O′abcM′ in Fig. 1).

For optimization of the diffuser shape, GA has been used as the optimization tool. The principle of GA has been discussed in details in a number of references [21,22]. The boundary and inlet conditions for this problem are kept the same for different simulations, and only the computational geometries have been varied. The different options for the geometry of the diffuser wall (curve *abc* of Fig. 1) are generated by some design variables. These design variables are control points defined by the horizontal and vertical positions on the curve *abc* (in Fig. 1). Selection of these design variables or control points is most crucial for the present study. These design variables or control points are the sole input parameters from the GA to the CFD software. The control points P_i (x_i,y_i) derived from the GA-string is directly used to construct the curve representing the wall shape. x and y coordinates of the control points are independently evaluated from the GA-string and transported to the Gambit for the construction of the NURBS curve. The positions of the control points are chosen with respect to a coordinate system, as shown in Fig. 1. Attempts are made to determine optimal shape of the wall by varying the number of control points starting from one to six. The coordinates of each control point are constrained by the upper and lower bounds. These upper and lower bounds vary with the number of control points or design variables used to construct the wall shape. The general form of the constraints for x coordinate is given below for all the six cases.

$$\left[d + (m-1)\left(\frac{3d}{n}\right)\right] \le x_m \le \left[d + m\left(\frac{3d}{n}\right)\right] \ , \tag{2}$$

where n and m are integers and

$$1 \le n \le 6 \, , \tag{3}$$

$$1 \le m \le n \, . \tag{4}$$

x_m denotes the x coordinate of the m^{th} control point, where a total of n control points have been taken. The upper and lower bounds of y coordinates for all n control points have been kept the same, as expressed below.

$$0.09d \le y_m \le 2.1d \quad (5)$$

Considering the fact that the y coordinates of the extreme ends of the diffuser (a and c in Fig. 1) are $1.0d$ and $2.0d$, respectively, one may have taken $1.0d \le y_m \le 2.0d$. Instead, equation (5) has been chosen to provide a greater flexibility in design and give a larger search space for y_m.

GA program and the CFD software combine with each other seamlessly and data transfer takes places without any manual intervention. Using specially designed system commands, the interfacings among GA, Gambit and Fluent are done in such a manner that no human interventation is required. This has been achieved through an algorithm coded with the C programming language. The main challenge lies in embedding highly structured commercial softwares like Fluent and Gambit inside an indigenously developed control loop.

4. RESULTS AND DISCUSSION

Population size for the implemented GA has been taken as 40 and the crossover and mutation probabilities are considered as 0.5 and 0.01, respectively. The GA program is made to run for 100 generations, though optimum solution is obtained much before the maximum generation.

Before running the optimization algorithm, simulation of fluid in a diffuser geometry with a sudden expansion at its midway has been tried. The streamline pattern obtained by this exercise is shown in Fig 2. C_p^* value has been obtained as 0.34 for this shape. There is a prominent separation bubble at the top most corner just after the expansion. It is needless to say that such a big recirculation is mainly responsible for the large pressure drop experienced in a diffuser with a sudden expansion. A gradual increase in the cross sectional area will reduce both the separation as well as pressure drop.

As mentioned earlier, the number of control points has been varied to explore various design options. Table 1 shows the C^*_p values obtained with different number of control points and their optimal positions. It is important to note that coordinate values have been obtained as the function of inlet half-width (d). This generalizes the optimum solution. It is clear from the table 1 that an increase in the number of control points does not increase C^*_p monotonically. The magnitude of C^*_p starts falling, if the number of control points are more than four. Streamline pattern for the six different cases are shown in Fig. 3 to have a better appraisal of the various optimum designs presented in Table 1, In all the six cases, one can observe a smooth fanning of streamlines from a half width d to the half width $2d$ without any separation. Duct profile changes gradually with the increase of control points. The angles both at 'a' and 'c' (refer to Fig. 1) become steeper, as the number of control points is increased. Further, the curve abc transforms from a concave one to a convex one, as the number of control points goes above four. For five and six numbers of control points, the diffuser cone takes a bell shape. With this shape, there is gradual decrease in C^*_p according to the present simulation. However, the changes in both in the value of C^*_p and wall length for different cases of optimum design are marginal. This gives a confidence in achieving the optimum design through GA.

In the above exercise, diffuser length has been kept fixed as $3d$ and the optimum shape has been obtained. It is obvious that the maximum value of C^*_p depends on this length and a length of $3d$ need not be the best choice. Next, an investigation has been made by varying the diffuser length. Four additional lengths $2d$, $4d$, $5d$ and $7d$ have been considered and the optimum shapes have been obtained following the methodology already outlined in the above section. Interestingly, in all the four cases maximum value of C^*_p is obtained when four

control points are considered. The results of this investigation have been shown in Fig. 4. From Fig. 4 it is clear that C^*_p value increases with the diffuser length.

Table.1 C^*_p values with different number of control points and their optimal positions

Case	Curve wall length	C^*_p value	Points No.	x Coordinate	y Coordinate
Single control	3.44d	0.716660	1st	1.245d	1.026d
Two control points	3.45d	0.716725	1st 2nd	1.534d 3.613d	1.059d 1.761d
Three control points	3.45d	0.716562	1st 2nd 3rd	1.690 d 2.986 d 3.872 d	1.094 d 1.504 d 1.915 d
Four control points	3.43d	0.717127	1st 2nd 3rd 4th	1.415 d 2.343 d 3.214 d 3.909 d	1.046 d 1.265 d 1.556 d 1.919 d
Five control points	3.43d	0.714348	1st 2nd 3rd 4th 5th	1.570 d 2.197 d 2.794 d 3.394 d 3.905 d	1.112 d 1.353 d 1.595 d 1.807 d 1.955 d
Six control points	3.42d	0.713986	1st 2nd 3rd 4th 5th	1.258 d 1.969 d 2.488 d 2.969 d 3.426 d	1.043 d 1.269 d 1.501 d 1.667 d 1.801 d

Figure 2: Stream line pattern in the diffuser with a sudden expansion.

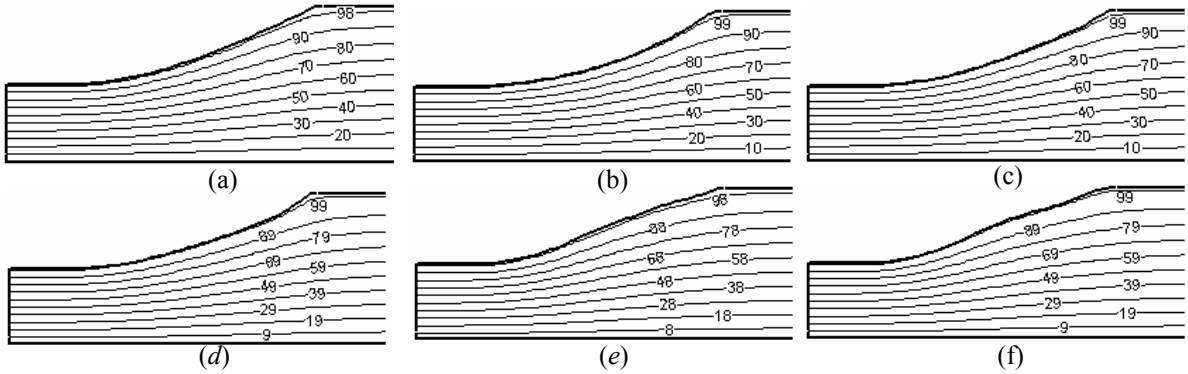

Figure 3: Optimum half shape of the diffuser and the corresponding streamline pattern for different control points (a) single control point, (b) two control points, (c) three control points, (d) four control points, (e) five control points, (f) six control points.

The trend is not surprising, as with a larger length of the diffuser the streamlines smoothly fan out from a lower to a higher cross-section. This reduces the possibility of flow separation. However, it can also be seen that the rate of increment in C^*_p diminishes with the gradual

increases in diffuser length. The criteria become maximum at a diffuser length of 5*d* but show a drooping trend, when the length is increased further to 7d. An increase in length of the diffuser beyond a certain limit may give a marginal advantage in the reduction of form drag but increases skin friction. In most of the practical applications, the maximum allowable length of the diffuser is limited. As the optimization algorithm is generic in nature, one can try any length of the diffuser but the final selection should depend on constraints like available space, system layout etc.

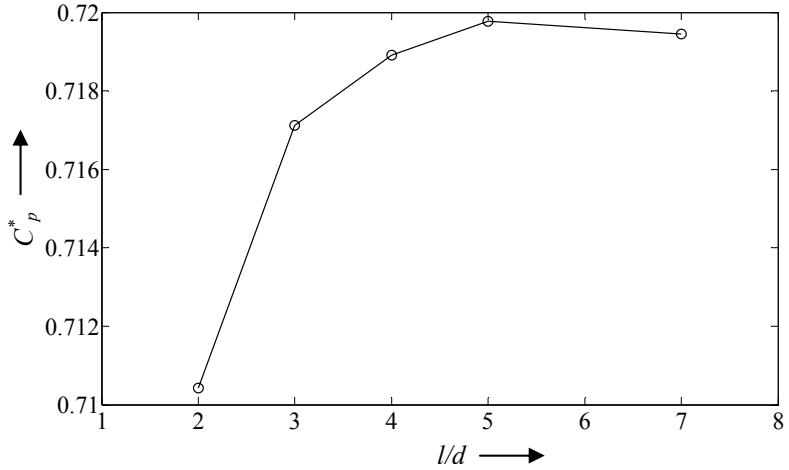

Figure 4: Variations of the highest value of optimum pressure recovery coefficient (C^*_p).

5. CONCLUSION

An indigenous algorithm has been developed for the optimization of a planar 2D symmetric diffuser. It not only executes the GA but also drives the Fluent and Gambit for the computation of C^*_p. By some specially designed system commands, it creates the interface among GA, Gambit and Fluent in a manner, such that no human interventation is required. The control points have been directly used after deriving from the GA-string to construct the curve representing the wall shape and the number of control points has been varied to cover a large enough search space.

The optimum diffuser shows a substantial improvement compared to the stepped diffuser. This can be substantiated through a comparison of C^*_p value.

It has been observed that too many control variables increase the computational time required but do not guarantee a better design. Again by using too few a variables, a limited range of shape alternatives is examined. Therefore, a wide range of shapes defined by a relatively small number of parameters are most suitable for achieving the optimum design. Here, four number of control points was found to be the best option.

C^*_p value increases with the diffuser length but the rate of increment in C^*_p diminishes with the gradual increase in diffuser length.

6. REFERENCES

[1] Mohammadi, B., Pironneau, O. Applied Shape Optimization for Fluids. Oxford University Press, 2001.

[2] Dulikravich, G. S. Aerodynamic shape design and Optimization. *AIAA Paper No.* 91-0476, (1991).

[3] Falco, I. D. An introduction to Evolutionary Algorithms and their application to the aerofoil design problem-Part I: the Algorithms. Von Kármán Lecture Series on Fluid Dynamics, Bruxelles, Belgium, April, 1997.
[4] Mäkinen, R., Neittaanmäki, P., Périaux, J., and Toivanen, J. A genetic algorithm for multiobjective design optimization in aerodynamics and electromagnetics, in: Papailiou, K. D., Tsahalis, D., Périaux, J., Knörzer, D. (Eds.), Computational Fluid Dynamics'98, Proceedings of the ECCOMAS 98 Conference, Wiley, Athens, Greece, 1998, Vol. 2, pp. 418-422.
[5] Baysal, O., Eleshaky, M. Aerodynamic design optimization using sensitivity analysis and computational fluid dynamics. *AIAA J.*, 30(1992), pp.718-725.
[6] Reuther, J., Jameson, A., Alonso, J., Rimlinger, M. and Saunders, D. Constrained multipoint aerodynamic shape optimization using an adjoint formulation and parallel computers. *Part 1, J. Aircraft*, 36(1999), pp.51-60.
[7] Reuther, J., Jameson, A., Alonso, J., Rimlinger, M. and Saunders, D. Constrained multipoint aerodynamic shape optimization using an adjoint formulation and parallel computers. *Part 2, J. Aircraft*, 36(1999), pp.61-74.
[8] Bängtsson, E., Noreland, D. and Berggren, M. Shape optimization of an acoustic horn. *Comput. Methods Appl. Mech. Engrg.*, 192(2003), pp.1533-1571.
[9] Mohammadi, B., Molho, J. and Santiago, J. Incomplete sensitivities for the design of minimal dispersion fluidic channels. *Comput. Methods Appl. Mech. Engrg.*, 192(2003), pp.4131-4145.
[10]Lehnhauser, T., Schafer, M. A numerical approach for shape optimization of fluid flow domains. *Comput. Methods Appl. Mech. Engg.*, 194(2005), pp.5221-5241.
[11]Kline, S. J., Abbott, D. E. and Fox, R. W. Optimum design of straight-walled diffusers. *Journal of Basic Engineering,* 81(1959), pp.321-329.
[12]Reneau, L. R., Johnston, J. P. and Kline, S. J. Performance and design of straight, two-dimensional diffusers. *Journal of Basic Engineering*, 89(1967), pp.141-150.
[13]Carlson, J. J., Johnston, J. P. and Sagi, C. J. Effects of wall shape on flow regimes and performance in straight, two-dimensional diffusers. *Journal of Basic Engineering*, 89(1967), pp.151-160.
[14]Cabuk, H., and Modi, V. Optimum Plane Diffusers in Laminar Flow. *Journal of Fluid Mechanics*, 237(1992), pp.373–393.
[15]Svenningsen, K. H., Madsen, J. I., Päuker, W. H. G. and Hassing, N. H. Optimization of Flow Geometries Applying Quasi-Analytical Sensitivity Analysis. *Applied Mathematical Modelling*, 20(1996), pp.214-224.
[16]Madsen, J. I., Shyy, W.R. and Haftka, T. Response surface techniques for diffuser shape optimization. *AIAA J.*, 38(2000), 9, pp.1512-1518.
[17]Maeng, J. S. and Han, S. Y. Application of the Growth-Strain method for Shape optimization of flow systems. *Numerical Heat Transfer, Part A*, 45(2004), pp.235-246.
[18]Fan, H. Y., Dulikravich, G. S. and Han, Z. X. Aerodynamics data modeling using support machines. *Inverse Problem in Science and Engineering*, 13(2005), pp.261-278.
[19]Goel, T., Dorney, D. J., Haftka, R. T. and Shyy, W. Improving the hydrodynamic performance of diffuser vanes via shape optimization. *43rd AIAA/ASME/SAE/ASEE Joint Propulsion Conference & Exhibit*, Cincinnati, OH, July 8-11, 2007.
[20]Pratihar, D. K. Soft Computing. Narosa Publishing House, New Delhi, India, 2007.
[21]Goldberg, D. E. *Genetic* Algorithms in search, Optimization & Machine Learning. Pearson Education, Inc., 1989.
[22]Fluent Inc., FLUENT 6.3 User's Guide, Lebanon, New Hampshire.
[23]Fluent Inc., GAMBIT 2.3 User's Guide, Lebanon, New Hampshire.

Proceedings of the 4th BSME-ASME International Conference on Thermal Engineering
27-29 December, 2008, Dhaka, Bangladesh.

DESIGN OF AN AUTOMATIC FIRE ALARM AND FIRE EXTINGUISHING SYSTEM FOR ME DEPARTMENT

Souman RUDRA[a], A.S.M SAYEM[b], S. K. BISWAS[c], J. P. CHAKRABATTY[d], S.Shamsi HUQ[d] and H.T. KIM[a]

a. Division of Energy Systems Research, Graduate School, Ajou University, Suwon 443-749, Korea.
b. Division of Energy and Environmental systems, Graduate School of Engineering, Hokkaido University, Japan.
c. Department of Mechanical Engineering, CUET, Chittagong -4349, Bangladesh.
d. Department of Electrical and Electronic Engineering, CUET, Chittagong -4349, Bangladesh.
E-mail: soumanrudra@yahoo.com , yessayem@yahoo.com

ABSTRACT

Property management is entrusted with the responsibility of protecting and preserving an institution's buildings, collections, operations and occupants. Constant attention is required to minimize adverse impact due to climate, pollution, theft, vandalism, insects and fire. Because of the speed and totality of the destructive forces of fire, it constitutes one of the more serious threats. Vandalized or environmentally damaged structures can be repaired and stolen objects recovered. Items destroyed by fire, however, are gone forever. An uncontrolled fire can obliterate an entire room's contents within a few minutes and completely burn out a building in a couple hours. The first step toward halting a fire is to properly identify the incident, raise the occupant alarm, and then notify emergency response professionals. This is often the function of the fire detection and alarm system. Several system types and options are available, depending on the specific characteristics of the protected space. Fire protection experts generally agree that automatic sprinklers represent one of the single, most significant aspects of a fire management program. Properly designed, installed, and maintained, these systems can overcome deficiencies in risk management, building construction, and emergency response. They may also provide enhanced flexibility of building design and increase the overall level of fire safety.

KEYWORDS: *Automatic fire alarm; smoke detector; ME department.*

1. INTRODUCTION

A key aspect of fire protection is to identify a fire emergency in a timely manner, and to alert the building's occupants and fire emergency organizations. This is the role of fire detection and alarm systems. Depending on the anticipated fire scenario, building and use type, number and type of occupants and criticality of contents and mission, these systems can provide several main functions. First the system provides a means to identify a developing fire through either manual or automatic methods and second, they alert building occupants to a fire condition and the need to evacuate. Another common function is the transmission of an alarm notification signal to the fire department or other emergency response organization. The systems may also

shut down electrical, air handling equipment or special process operations, and they may be used to initiate automatic suppression systems like water sprinkler systems.

2. OBJECTIVES

The following objectives were set:

- To design an automatic fire alarm system for Mechanical Engineering Department of CUET.
- To install the designed fire alarm system.
- To test the fire alarm system.

3. METHODOLOGY

It has been decided to follow the following methodology in completing the project work.

- Study of fire alarm system equipments.
- Study of various fire alarm systems.
- Inspection of various fire alarm systems.
- To design suitable system for ME department.
- To install & test the system.

4. PLACEMENT OF FIRE DETECTOR IN ME DEPARTMENT

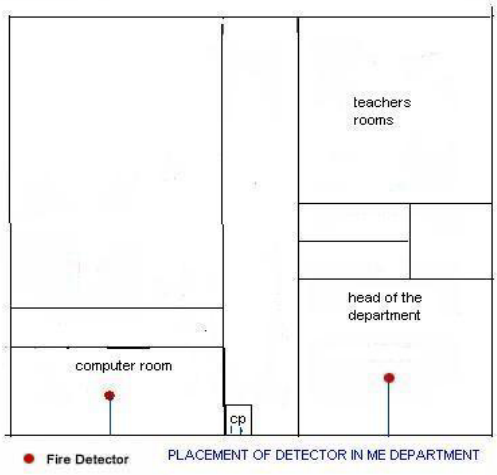

CP= Control Panel

Fig.1 Position of fire alarm

5. AUTOMATIC FIRE DETECTION SYSTEMS

Automatic fire detection systems, when combined with other elements of an emergency response and evacuation plan, can significantly reduce property damage, personal injuries, and loss of life from fire in the workplace. Their main function is to quickly identify a developing fire and alert building occupants and emergency response personnel before extensive damage occurs. Automatic fire detection systems do this by using electronic sensors to detect the smoke, heat, or flames from a fire and providing an early warning.

Fig.2 Smoke Detector

If your workplace uses a fire detection system that was designed and installed to meet the fire protection requirements of a specific OSHA standard, it must also comply with the "Fire Detector".

Fig.3 product of fire

Fire detectors work by sensing one or more products of fire. The three most common detectors are: .Smoke detectors.

- .Heat detectors.
- .Flame detectors.

5.1 Smoke detectors

Smoke detectors detect the visible or invisible smoke particles from combustion. The two main types are ionization detectors and photoelectric detectors

Fig.4: ionization detector

5.2 Ionization detectors

The ionization detector contains a small radioactive source that is used to charge the air inside a small chamber. The charged air allows a small current to cross through the chamber and complete an electrical circuit**.** When smoke enters the chamber, it shields the radiation, which stops the current and

triggers an alarm. These detectors respond quickly to very small smoke particles (even those invisible to the naked eye) from flaming or very hot fires, but may respond very slowly to the dense smoke associated with smoldering or low-temperature fires.

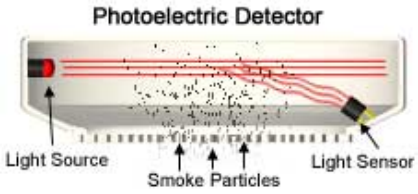

Fig.5 photoelectric detector

5.3 Photoelectric detectors

In a photoelectric smoke detector, a light source and light sensor are arranged so that the rays from the light source do not hit the light sensor. When smoke particles enter the light path, some of the light is scattered and redirected onto the sensor, causing the detector to activate an alarm. These detectors react quickly to visible smoke particles from smoldering fires, but are less sensitive to the smaller particles associated with flaming or very hot fires.

Fig.6 Heat detector

5.4 Heat Detectors

Heat detectors are normally used in dirty environments or where dense smoke is produced. Heat detectors may be less sensitive, but are more appropriate than a smoke detector in these environments. The most common heat detectors either react to a broad temperature change or a predetermined fixed temperature

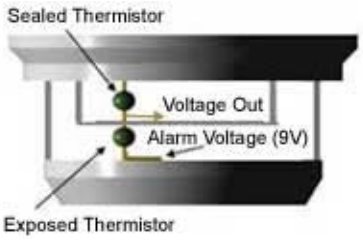

Fig.7 Heat detector with thermmistors

Heat detectors use a set of temperature-sensitive resistors called thermistors that decrease in resistance as the temperature rises. One thermistor is sealed and protected from the surrounding temperature while the other is exposed. A sharp increase in temperature reduces the resistance in the exposed thermistor, which allows a large current to activate the detector's alarm.

Fig.8 Flame Detectors

Flame detectors are line-of-sight devices that look for specific types of light (infrared, visible, ultraviolet) emitted by flames during combustion. When the detector recognizes this light from a fire, it sends a signal to activate an alarm

.

6. COST ESTIMATION

Equipments for circuit	Cost (BD taka)
Sensor	150.00
Chamber(sensor)	12.00
Switch for Sensor	5.00
LED -2 pieces	20.00
Speaker	35.00
Registers(5 pieces)	10.00
Capacitor(2 pieces)- (16v-100μF)	25.00
(25v-470μF)	30.00
Diode	20.00
Relay	55.00
Transistor(LM-35)	150.00
Power supply port	5.00
Control panel port	5.00
Others	
Loud Speaker (Siren Horn)	250.00
Wire(flexible, normal)	20.00
Switch for off & on of output	15.00
Initializing screws	5.00
Bare broad	40.00
Initialization charge	250.00
Others	150.00
Total	1358.00

These are only for a individual fire alarm system, and the total cost for this is about 1358.00 whenever we design for the whole building it includes what no. of fire detector are used in these system. Then the total cost will increase. Normally a detector can control 50 square feet area. So if the room is 300 sf (square feet) then we use 6 no. of detector in that room.

7. ABOUT THE PROJECT

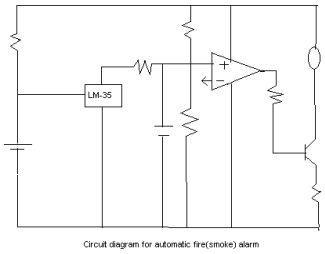

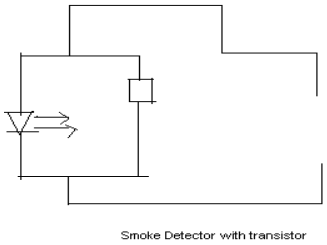

Fig.9 circuit diagram

7.1 Over all view of this project

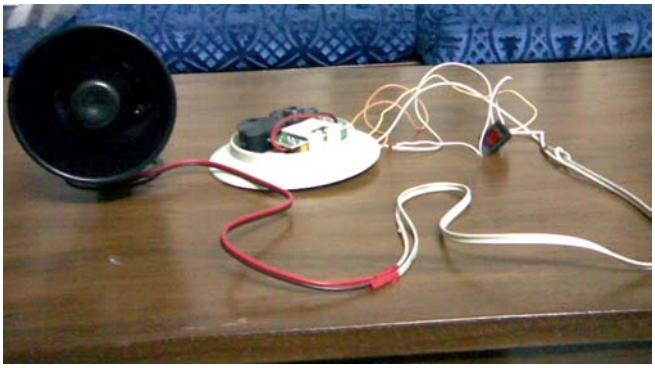

Fig.10 overall view

7.2 Special feature of my projector

1) Blinking LED Light

The indicator light under the Push to Test button blinks about once per minute to indicate the smoke alarm is receiving power.

2) False alarm control:

Simple push the test button to temporarily salience the smoke alarm if a nuisance the smoke alarm occurs or to prevent nuisance alarm. By momentarily depressing the test button, the alarm will automatically switch to a special reduce sensitivity condition for up to 15 minutes, after which it will reset to its full normal sensitivity. If a real fire occurs, however, and the quantity of smoke reaching the smoke alarm is sufficiently great, the until will sound an alarm.

3) Safety light:

This smoke alarm uses a miniature lamp designed to last for an average of 15 hours of continuous operation. When anyone pushes the test button the light will flash along with the alarm sounding to indicate it is working properly.

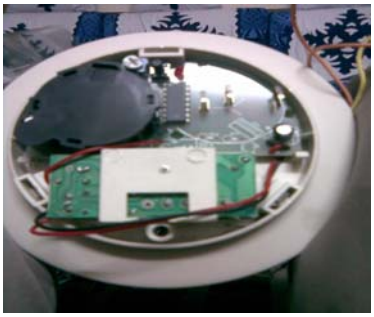

(a) (b)

Fig.11 (a) Input-Output port, Relay, Capacitor etc, (b) Circuit with a stand

8. FIRE EXTINGUISHING SYSTEM COMPONENTS

1) Discharge nozzles
2) Piping
3) Control panel
4) Discharge or warning alarms
5) Hazard warning or caution sign
6) Automatic fire detection devices
7) Manual discharge station
8) Storage container(s) & extinguishing agent

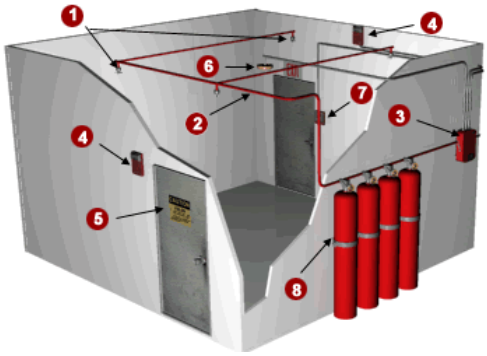

Fig.12 Position of system components

CONCLUSION

A fire alarm system's level of sophistication can range from manual pull stations that only alert nearby occupants to a networked campus complex consisting of multiple control panels with a variety of automatic detection inputs. The fire alarm system contributes to the well being of our life which is self evident. It gives people a way to get help quickly and automatically at the outbreak of fires. Although there are three types of transmission systems in use today, telegraphic, telephone and radio communication, much of the original hardwired technology, methods and procedures still apply.

In Bangladesh, many accidents are occurred by fire due to unserious ness. Most recent fire accident in Bangladesh occurred at Dhaka at NTV building. The fire spreader with alacrity and

caught different floors in huge flames. Panicked people were crying and asking for help from the top floors. After almost three hours fight the situation came under control. Also different export oriented industry which were engaged to reserve foreign currency were destroyed for such kind of accident. In every work safety is first. So when we are able to install fire alarm system and extinguishing system in our industrial and domestic purpose then we can save our lives.

I have designed a fire alarm system with smoke detector. This can be installed in any laboratory, room or office. This system will raise alarm if smoke is formed and a bell will ring at a place desired by the user. The designed system has been tested in a small scale and it can be installed if required components are purchased. A cost estimation is also made. In testing it was found the designed system worked as planned.

REFERENCES

[1] J. M. Robinson, Fire from space: global fire evaluation using infrared remote sensing. International Journal of Remote Sensing, 12 (1991), 3 – 24.
[2] S.M. Simence, Fire Dynamics I
[3] Rudolf F. Graf and George, The build-IT book of electronic project.
[4] Cecile E. Grant, Fire safety science.
[5] Boylsted, Introduction of Circuit Analysis
[6] http://www.ehs.uci.edu/programs/fire/firealarmsystem.pdf
[7] R.M. Stelting, Book for Fire alarm system, IEEE Boston Section. All rights reserved
[8] www.alarm-system-alart.com
[9] F.R. Doland, Fire safety Engineering Evaluation.
[10] International fire Protection Association, http://www.nfpa.org
[11] Venter, J. (2000). Firehawk™ electronic forest fire detection and management system. International Forest Fire News, 23, 105– 108.
[12] www.fire.nist.gov

Proceedings of the 4th BSME-ASME International Conference on Thermal Engineering
27-29 December, 2008, Dhaka, Bangladesh

PROBABLE SOLUTION OF TORQUE DIP PROBLEM OF CAMPRO 1.6L ENGINE

Mohiuddin, A.K.M., Rahman, A., Arfah, A., and Farraen, M.A.

Department of Mechanical Engineering
International Islamic University Malaysia.
E-mail: mohiuddin@iiu.edu.my

Abstract

CAMPRO engine is a basic Double Overhead Camshaft (DOHC) which has a capacity of 1597 cc and installed with a total of 16 valves developed by Malaysian car manufacturer PROTON. The CAMPRO engine experiences performance downfall (torque dip) when it reaches at 2500 – 3500 rpm. The main objective of this work is to perform an extensive study on the causes of the torque dip in CAMPRO engine and subsequently to provide the best solution that will improve the performance and reliability. The dip which occurs at 2500 – 3500 rpm is mainly influenced by the geometry of the designed intake manifold and valve timing. Analysis is mostly confined on the intake manifold geometry. From the analysis done, two possible solutions were provided viz., Natural Dual Intake Manifold and Continuous Variable Intake Manifold.

Keywords: *CAMPRO Engine, Torque Dip, Manifold Geometry, Valve Timing, GT-Suite.*

1. INTRODUCTION

CAMPRO engine has been developed by Malaysian car manufacturer PROTON in 2000. The CAMPRO engine is a basic Double Overhead Camshaft (DOHC) which has a capacity of 1597 cc and installed with a total of 16 valves. The bore and stroke dimensions of each cylinder is 76 mm and 88 mm respectively. It is claimed to produce 110 bhp (82 kW) @ 6500 RPM and 148 Nm of torque [1]. Despite of the great achievement, PROTON is facing a problem with the performance of its engine. In order to compromise the maximum torque and achieving the required emission level, PROTON engineers had to sacrifice the performance of the low-end torque of the engine. Therefore, unlike any other average performance engines, the CAMPRO engine experiences performance downfall when it reaches at certain rpm. The phenomenon is known as torque dip or torque loss where the output torque is not smooth, consequently formed a dip in the torque curve. The dip which occurs at 2500 – 3500 rpm is mainly influenced by the geometry of the designed intake manifold and valve timing. The main objective of this work is to perform an extensive study on the causes of the dip in CAMPRO engine and subsequently to provide the best solution that will improve the performance, reliability as well as production cost. The analysis is mostly confined on the intake manifold geometry and the valve timing. This is done by simulating similar model of CAMPRO in the GT SUITE software and acquired the results of changed intake geometry and valve timing on the output torque.

GT-SUITE is an integrated set of computer-aided engineering (CAE) tools developed by Gamma Technologies, Inc. to address engine and power train design [2]. GT-SUITE comprised of six solvers (GT-Power, GT-Drive, GT-Vtrain, GT-Cool, GT-Fuel, and GT-Crank), a model-building interface (GT-ISE), a powerful post-processing package (GT-POST), and a collection of supporting tools [3]. GT-ISE provides the user with the graphical user interface (GUI) that is used to build models as well as the means to run all GT-SUITE applications. GT-SUITE comes with an individual solver specifically to assist engineers in the design of valve trains which is called GT-VTRAIN. A useful tool included in GT-VTRAIN is the VT-Design. Two distinct features of the tool are Cam Design and Valve Train Kinematics.

From the analysis it can be concluded that the torque dip phenomenon is caused by the pressure wave that is not coherent with the valve opening. The traveling pressure wave which is supposed to arrive at the time the intake valves are opening will be induced into the cylinder as a result of the vacuum effect created by piston's downward motion. The shape of the torque curve is largely dependent on the runner geometry, valve timing and pressure wave arrival.

.

2. GT POWER: CAMPRO ENGINE MODEL

A GT-Model is created to model the CAMPRO engine. The model data were referred from PROTON Power train department database [1]. Due to insufficient information, some data were taken from default value [2]. Fig. 1 shows the model of the CAMPRO in GT Power. Variation of torque with rpm for the CAMPRO 1.6L engine and its GT Power model is shown in Fig.2.

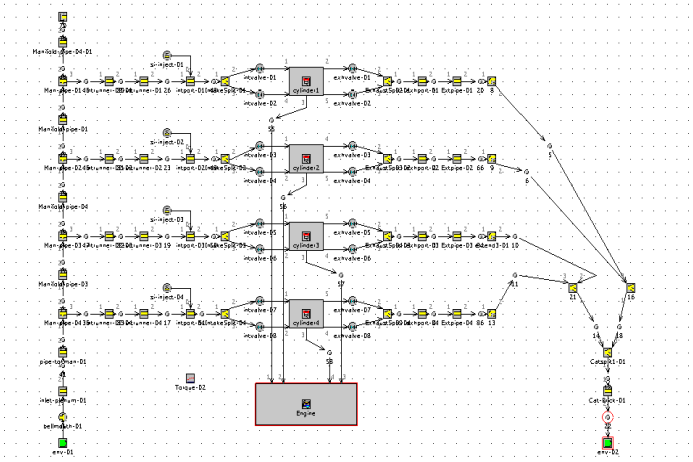

Fig.1. CAMPRO Model in GT Power

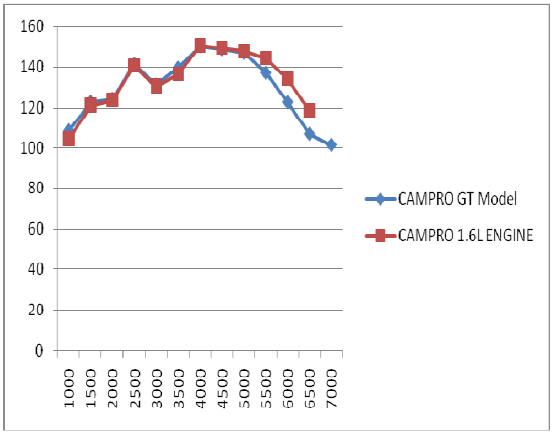

Fig.2. Torque vs RPM for the CAMPRO 1.6L Engine and its GT Model

3. ANALYSIS

3.1 INTAKE MANIFOLD PHENOMENON

Intake manifold is a complex part of the engine. The pressure behavior is relatively complex due to the negative and positive pressure wave oscillation in the manifold. The intake system can be modeled as a spring-mass system. A series of pulsating waves of expansion and compression are occurring in the intake runner. The wave travels back and forth in the runner due to inertia. The pressure at the port builds up when the valve is closed (Fig.3). As it builds up, the pressure wave travels back and forth creating an oscillating wave. Theoretically, when the

timing of the pressure wave is right, the pressure wave will travel towards the cylinder when the valve is open and the pressure at the port falls below atmospheric pressure. At the maximum opening of the valve, the positive pressure starts to drop as the valve starts to close. The pressure in the port will start to increase as the valve closes. When the valve is fully closed, the pressure wave travels backward as a negative pressure wave. Then, the pressure wave travels back to the valve again until the valve is open for the next cycle. According to Lumley [4], as seen in the pressure graph in Fig. 4, the pressure in the intake manifold can be modeled as a loaded spring and is released. The fluid in the runner oscillates in similar manner as the spring-mass system. The oscillations dampen until the valves open again.

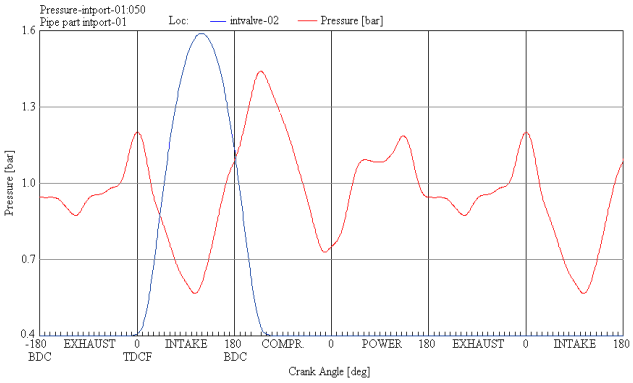

Fig.3. Intake Port Pressure vs. Crank Angle at 6000 rpm

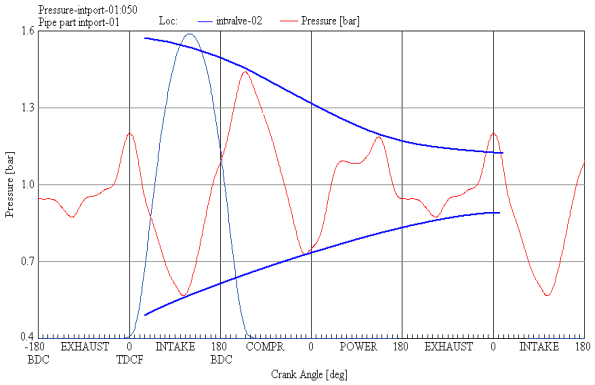

Fig.4. Valve Timing and Pressure Oscillation in Intake Manifold

Referring at crank angle where the valve is at its maximum opening in Fig.5, the pressure for the operating range other than 3000 rpm is much lower. Low pressure at the port when the valve is opening indicates pressure flowing into the cylinder. Therefore the pressure at 3000 rpm during valve opening is higher in magnitude than the pressure at 2500 rpm during valve opening. It shows that the pressure wave that sucked into the cylinder is lower at 3000 rpm than at 2500 rpm, consequently producing less torque and power. This is where the torque dip occurs. This happens mainly because of the timing the pressure arrives at the valve. If the pressure wave arrives later than it supposes to be, then the pressure at 3000 rpm can be lowered and more pressure may enter the cylinder. To make the pressure at 3000 rpm arrives later; the length of the runner has to be changed so that the pressure of 3000 rpm at maximum opening of valve is lower than the pressure of 2500 rpm at maximum opening. Then, it will have higher cylinder pressure at maximum valve opening. It is important to tune the length [5] accordingly, so that maximum cylinder pressure at the maximum valve opening can be achieved.

The runner length of the CAMPRO engine is optimized for higher torque at high rpm. So, the length is much shorter than other manufacturer's intake runner design. The low end torque is sacrificed and the torque dip occurs between 2500 and 3500 rpm (Fig. 6). The torque dip occurs only at this particular range because the valve timing and the pressure wave arrival time is not coherent at this range. The pressure wave arrives too early before the valve opens. The pressure arrival time at 3000 RPM is earlier than the opening of the valve. So, less pressure enters the cylinder. The oscillation at low rpm is more than the oscillation of higher rpm. At low engine speed, the valve opens and closes at a lower speed. So, the pressure wave formed in the intake runner bounces back and forth much more until the valve reopens. This explains why the oscillation at lower rpm is more than that at higher rpm. The more oscillations, the unstable the

pressure forms at the intake port. The number of effective pressure wave assisting the fluid flow is higher. So, the study of the pressure wave effects is only limited to rpm higher than 2500.

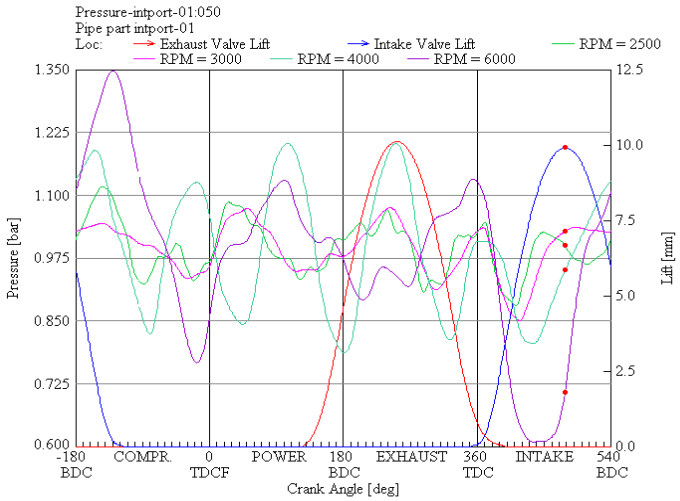

Fig.5. Intake Port Pressure and Intake Valve Lift vs. Crank Angle

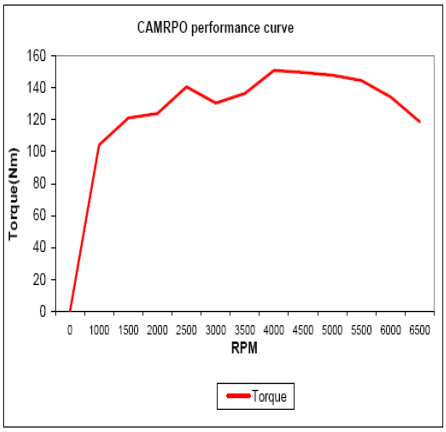

Fig. 6. CAMPRO Torque Curve

3.2 INTAKE RUNNER LENGTH

For optimum performance result, an appropriate length and diameter of the manifold should be used to get as much as possible of air/fuel mixture into the cylinder in time. The main key of the design of intake manifold is to provide maximum possible fresh charge during the intake stroke. In addition, by moving the air as fast as possible into the cylinder, we can increase the turbulence. Thus the mixing operation will be accelerated. The runner length controls the timing of the returning waves. With correct length of intake runner, it helps the wave in the runner to return at the port at correct time. But with the valve closing, the air cannot go anywhere and it piles up and became compressed. The compressed air must be diverted so that it turns around it and will flow back through the intake runner in the form of pressure wave (manifold pressure) at the time when the valve is opened and bounces back and forth. If timed properly, it will arrive at the port when the valve is opened again and the extra pressure can force extra air drawn into the engine thus increasing the volumetric efficiency. The amplitude of the pressure wave i.e., nearest to the maximum valve opening is the main concern. The pressure wave arrival time can be controlled by increasing or decreasing the length. By increasing the length, we can increase the travel duration, thus later arrival and vice versa.

4. POSSIBLE SOLUTION

Analysis shows that at the point of dip; a downfall of the volumetric efficiency also occurs. The volumetric efficiency is influenced by many factors such as the density of the fresh charge, the amount of exhaust gas in the clearance volume, the design of the intake and exhaust manifold and also the valve timing [6]. The volumetric efficiency is inter-related with the pressure wave [7]. In order to enhance the volumetric efficiency and to eliminate the torque dip, two parameters are considered, viz., runner length & diameter and valve timing. In this paper focus will be given on the length of intake manifold. Therefore two types of intake manifold; Natural Dual Intake Manifold (NDIM) and Continuously Variable Intake Manifold (CVIM) are analyzed.

4.1 NATURAL DUAL INTAKE MANIFOLD

The Natural Dual Length Intake Manifold (NDIM) is a manifold having two different paths internally with different diameters; small diameter and large diameter. Referring to Figure 7, the inlet, center and the outlet diameter of each pipe are not of the same size. The pipe is designed to have venturi in the middle of its length. The objective of having the venturi is to create a venturi effect on the air flow. Both pipes are designed to have the same length. The hypothesis made is that during the low end speed, the air will utilize the small diameter passage. But later when the engine reaches higher speeds, the pressure increases and the small diameter passages are incapable of providing maximum flow, the pressure will be shifted to the big diameter runner passage. This will in some way create the dual diameter intake manifold effect. To test the hypothesis, NDIM GT Model was created and simulated in the GT POWER. The intake manifold of CAMPRO GT model was replaced by the split pipe having small diameter and large diameter for each cylinder. Comprehensive simulations are done by varying different diameter and length to get the appropriate diameter and length for each pipe that give the best performance. The NDIM GT model is shown in Figure 8. As stated earlier in the hypothesis, the

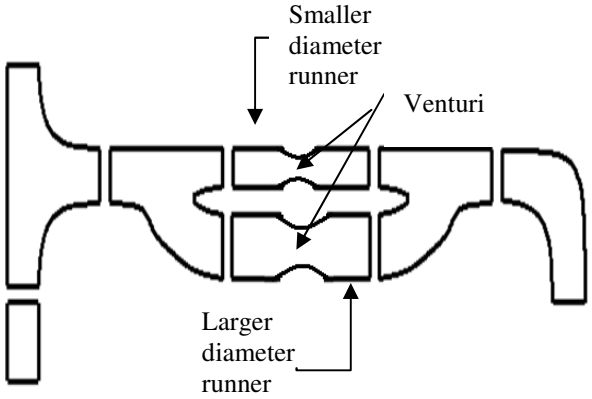

Figure 7. Intake Runner of NDIM Model

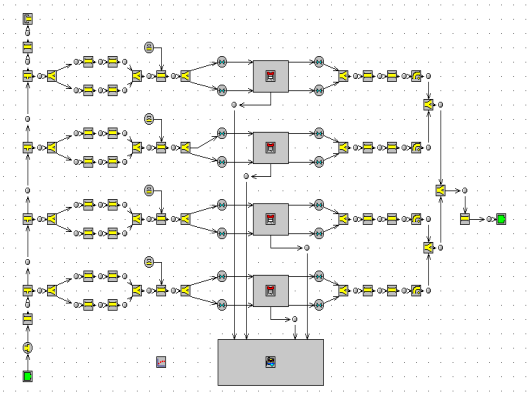

Figure 8. NDIM GT Model

air will utilize the small diameter passage during the low end speed. But later when the engine reaches higher speeds, the pressure increases and the small diameter passages are incapable of providing maximum flow, so the pressure is shifted to the big diameter runner passage. This will in some way create the dual diameter intake manifold effect. In order to verify the hypothesis made, the NDIM GT model was simulated and the pressure of each runner is compared. With higher speed, the pressure in the larger diameter runner will increase thus acting as a dual diameter intake manifold. The operation is similar to the dual diameter intake that uses the butterfly valve except that this system is self-actuated depending on the maximum pressure at the small runner. The effects of changing the diameter and length will cause unpredictable behavior of pressure and torque. From the result of the simulation, it is observed that a promising outcome is achieved. Figure 9 shows the comparison of the output torque between CAMPRO engine, CAMPRO GT model and NDIM GT model. With NDIM, it is effective most when used at low engine speeds. The main objective of torque dip is eliminated using NDIM. The fabricated prototype of the NDIM is shown in Figure 10.

4.2 CONTINUOUSLY VARIABLE INTAKE MANIFOLD

An intake manifold based on the CAMPRO intake manifold is modified to have the varying runner length effect. A manifold that can vary its runner length at specific engine speed

advantage the high pressure in the intake manifold at all engine operating range. The runners are wrapped around a plenum housing which houses the rotating plenum. The plenum along with the inlet of the primary runners rotates along the primary runner creating the elongation of the runners. The Continuously Variable Intake Manifold is shown in Figure 11. FLUENT software is used to simulate the flow in the manifold. The results of the CVIM simulation show an increase of the low end torque by 12Nm and the maximum torque by 5Nm. The manifold can be easily adjusted to have the most optimized air flow to the engine.

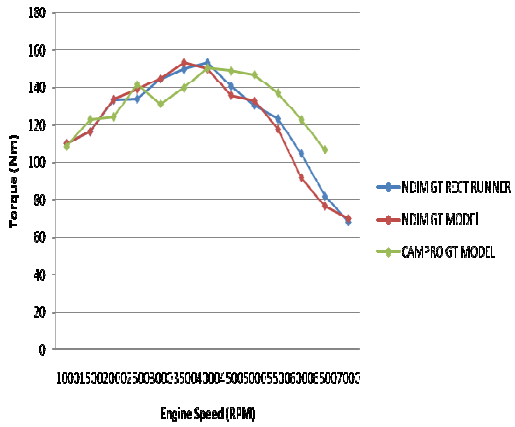

Figure 9. Performance of CAMPRO, CAMPRO GT and NDIM GT Model - Torque

Figure 10. Fabricated NDIM

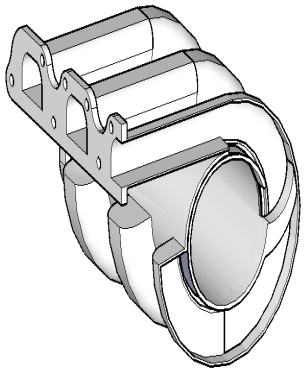

Figure 11. Continuously Variable Intake Manifold Model

5. CONCLUSION

The causes of occurrence of torque dip between the range of 2500 rpm – 3500 rpm are thoroughly investigated. It can be concluded that the torque dip phenomenon is caused by the pressure wave that is not coherent with the valve opening. The traveling pressure wave which is supposed to arrive at the time the intake valves are opening will be inducted into the cylinder as a result of the vacuum effect created by piston's downward motion. The shape of the torque curve can be optimized using different types of manifold. The NDIM and CVIM can increase the performance of the low end of engine. Both of the manifolds have their own advantages.

REFERENCES

[1] http://www.proton.com/innovation/rnd/campro.php, (2005)
[2] Gamma Technologies, GT-Suite, http://www.gtisoft.com, (2004).
[3] GT-suite V6.1 User's Manual, Gamma Technologies, (2004).
[4] Lumley, John, L., , Cambridge University Press, (2000).
[5] Hartman, J., How to Tune & Modify Engine Management Systems, MBI Publishing Company, (2003).
[6] Ganesan, V., Internal Combustion Engines, Tata McGraw-Hill, 2nd Ed. 2004.
[7] Ohata, A., and Ishida, Y., "Dynamic Inlet Pressure and Volumetric Efficiency of Four Cycle Four Cylinder Engine" SAE paper 820407, SAE Trans., vol. 91, (1982).

Acknowledgement: The paper is an outcome of the research project EDW B0802-97 funded by Research Management Centre, IIUM.

Proceedings of the 4th BSME-ASME International Conference on Thermal Engineering
27-29 December, 2008, Dhaka, Bangladesh

DESIGN STUDY OF PODDED PROPULSION SYSTEM FOR NAVAL SHIP

M.P Abdul Ghan, M.Z. Mohd Yusop & M. Rafiqul Islam
Faculty of Mechanical Engineering
University Technology Malaysia (UTM), Skudai, Johor, Malaysia
e-mail: pauzi@fkm.utm.my

ABSTRACT

This study was carried out to investigate the effect of existence of pod housing to the ship in aspects of stability characteristics and resistance. The basis ship chosen to be analyzed is Sealift class type Multi Purpose Command Support Ship (MPCSS). This basis ship was redrawn by using MAXSURF software. In this study, selection of dimension of the new pod housing is based on design that had been proved by VTT Technical Research Centre of Finland. After the dimension of new design is obtained by using comparative method, the basis ship is attached with this pod housing at suitable position after taking into consideration of all clearance. The basis ship and ship with pod are then compared in terms of hydrostatic properties, stability and resistance characteristics. On this study, the stability assessment has been conduct by using HYDROMAX software while for the resistance characteristics, the assessment been conduct by using HULLSPEED software. The result from this study shows that the stability characteristic for ship with pod housing is better than basis hull while the resistance analysis show that ship with pod housing has bigger resistance value.

KEYWORD*S: Podded Propulsion, Resistance, Stability, sealift class*

1. INTRODUCTION

Ships play a major role in global transportation of cargos in terms of weight and volume. It also plays the important role for the national maritime's security. In Malaysia, government agencies that lead the national maritime's security are Royal Malaysian Navy, Malaysia Maritime Enforcement Agencies, Marine Police and Customary Agencies. Although ships have a long story of technological development, there are always new developments in order to meet the new requirement. For example, the propulsion system and the electric power generation plant are almost always integrated in some form. This integration may not be limited just for the shaft line propulsion system but also for azimuth propulsion or also known as podded propulsion [1]. In order to provide a function, the new propulsion system also must meet the requirements set by underlying principles such as physics, economics, reliability, safety, maintainability, space and weight limitations and controls. The system also need to follow the regulation set by national and regulatory bodies such as International Maritime Organization (IMO), International Electro-technical Committee (IEC), United States Coast Guard (USCG) and American Bureau of Shipping (ABS).

This paper will give the detail view about the podded propulsion itself including the principle of the propulsion, comparison with conventional propulsion in various aspects, identifying the advantages and disadvantages of this propulsion system and the effect of this propulsion system towards naval ships. The main objective of this study is to analyze the design of podded propulsion system and the effect of the pod itself towards naval ship's performance with respect to resistance and stability. The naval ship used in this study is Sealift class which is a naval supply vessel with length overall of 103 m.

The podded propulsion system normally used an electric motor driven by diesel electric drive [3]. This propulsion drive has been used in ice-breakers and other special purpose vessels. The electric propulsion drive system makes the ship more economical and easy to manage onboard. In January 2000 the U.S navy announced that its surface war ship would use an electric propulsion system eventually. The opportunities for ship designers to design a new generation war ship using electric drive are opening up there after. An electric propulsion system replaced the traditional mechanical shaft driven propellers with propulsion pods powered by electric motors. For many years, podded propulsion has been used for main propulsion as well as for manoeuvring. Such units were initially attractive for small and medium sized vessels [4] but have been extended to larger vessels especially because of their station keeping capabilities, which are often needed in the offshore marine industry. Podded propulsors are often electric drive propulsion units, azimuth through 360 degrees around their vertical axis.

2. HULL SELECTION AND PRINCIPAL PARTICULAR

As this research comparing the result on resistance and stability of bare hull and hull with podded housing, the hull used is the sealift class of Multi-purpose command support ship's type (MPCSS). This class are commonly used by world Navy. For bare hull with podded housing, the podded housing is attached at the afterward of the hull. The number of podded housing used is 1 (one) only. The basis ship particular data of sealift class ship are as in Table 1.

3. PARAMETRIC STUDY OF PODDED HOUSING

The method used in predicting the size of podded propulsion is by referring the proven design of pod. The proven pod size is as Table 2 below:

Table 1: Particular of the sealift class MPCSS ship. [6]

Item	Value
Length overall	103.000 m
Breadth	15.000 m
Depth	11.000 m
Camber	0.150 m
Dead rise	0.625 m
Draught	4.409 m
LBP	97.044
Displacement	4431.57

Table 2: Basic parameter of proved pod model [5]

Parameter	Value
Ship length, m	68.84
Propeller diameter (m), D	2.60
Number of blades, Z	4
Pitch ratio at 0.7R	0.85
Hub diameter ratio:	0.36
Expanded area / disc area, A_E/A_O	0.537
Pod length, Lp , m	3.12
Pod diameter dp , m	1.042

To determine the new design size is still subjective. It relates with many things like the power output required, the ratio with the bare hull area and also the position suitable to be placed so that the propeller at pod housing doesn't touch the ship's hull. The maximum propeller diameter that can be fitted after taking into account of all clearance is 4 metres. The suitable position of centre of pod that can be attached to the hull is at 98.671m from forward extremity. So, the maximum length of pod suitable is approximately 6.5 m (estimation from lines plan drawing). If the length of pod is too high, it will cause a defect to the ship when the pod turns at 180^0 where the blade of propeller will touch the ship's hull. The maximum size of

pod diameter allowed is 2.5 m after taking into account all clearance. The summary of new pod design parameter is on table 3 below. The size of the new design doesn't exceed the maximum size allowed. So, this parameter is acceptable. The result of the new lines plan drawing with podded housing attached is as on Figure 1, 2 and 3 below.

Table 3: Parameter of new pod design

Parameter	Value
Propeller diameter, m (D)	3.887
Pod length, m (L_p)	5.995
Pod diameter, m (D_p)	2
Pod length ratio, L_p/D	1.542
Pod diameter ratio, D_p/D	0.514

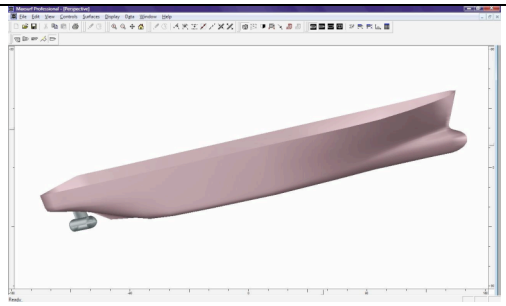

Fig. 1 Perspective view of hull with podded housing

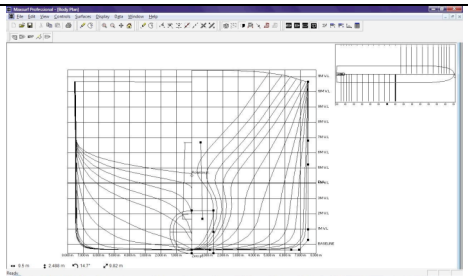

Fig. 2 Body plan view of hull with podded housing

Fig. 3 Model of podded housing in MAXSURF

3. 1 Hydrostatic Calculation

Hydrostatic data and hydrostatic curves had has been obtained from the HYDROMAX software. The hydrostatic curve for hull with podded housing is shown in figure 6 and the hydrostatic curve for hull without podded housing is shown in figure 7.

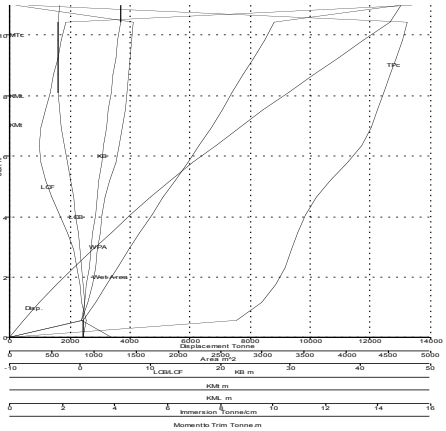

Fig. 4 Hydrostatic curves for hull with podded housing

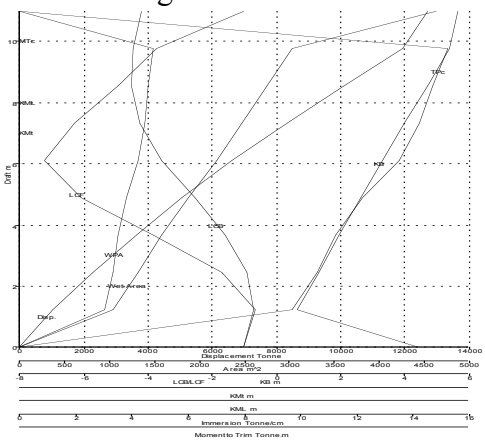

Fig. 5 Hydrostatic curves for hull without podded housing

3. 2 Stability Assessment

In stability assessment, both the hulls are analyzed using HYDROMAX software. The data input are the lines plan drawing from MAXSURF. In order to analyze the ship's stability by using HYDROMAX, the compartment must be formed. Figure 6 and 7 below show the compartments for hull without podded housing and hull with podded housing respectively.

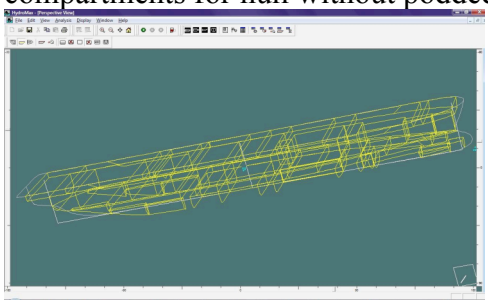

Fig. 6 Compartments for hull without podded housing

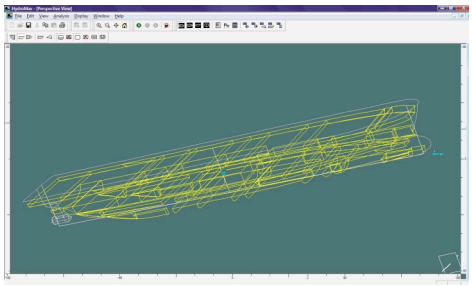

Fig. 7 Compartments for hull with podded housing

The stability assessment has been conducted for 4 loading conditions which are:

i. Full load (departure condition, 100%)
ii. Half load (50%)
iii. Arrival load (20%)
iv. Lightship condition

The assessment is based on IMO criteria. IMO requirement is given in Table 4 and the results of stability analysis are shown in table 5 below and GZ curves in figures 8, 9, 10 and 11 respectively.

Table 4: IMO criteria [7]

Stability Criteria	Large Ship (IMO)
Area Under Curve 0^0 - 15^0	N.A
Area Under Curve 0^0 - 30^0	$\geq$ 0.055 m.rad
Area Under Curve 0^0 – 40^0 or up to flooding angle	$\geq$ 0.090 m.rad
Area Under Curve 15^0 - 30^0	N.A
Area Under Curve 30^0 – 40^0 or up to flooding angle	$\geq$ 0.030 m.rad
Maximum GZ	$\geq$ 0.20 m
Angle at Maximum GZ	$\geq$ 30.0 deg
Initial GM	$\geq$ 0.35 m

Table 5: Result of stability assessment

Condition	Criteria	Hull with pod	Hull without pod
Departure (100%)	Area 0. to 30.	0.359	0.368
	Area 0. to 40. or Down flooding Point	0.673	0.687
	Area 30. to 40. or Down flooding Point	0.314	0.319
	GZ at 30. or greater	2.689	2.569
	Angle of GZ max	60	60
	GM	2.332	2.393

Half load (50%)	Area 0. to 30.	0.29	0.3
	Area 0. to 40. or Down flooding Point	0.541	0.556
	Area 30. to 40. or Down flooding Point	0.25	0.256
	GZ at 30. or greater	2.121	2.018
	Angle of GZ max	60	60
	GM	1.818	1.886
Arrival (20%)	Area 0. to 30.	0.268	0.278
	Area 0. to 40. or Down flooding Point	0.49	0.506
	Area 30. to 40. or Down flooding Point	0.222	0.228
	GZ at 30. or greater	1.828	1.736
	Angle of GZ max	60	60
	GM	1.665	1.737
Lightship	Area 0. to 30.	0.442	0.452
	Area 0. to 40. or Down flooding Point	0.75	0.764
	Area 30. to 40. or Down flooding Point	0.308	0.312
	GZ at 30. or greater	2.416	2.334
	Angle of GZ max	70	60
	GM	3.124	3.213

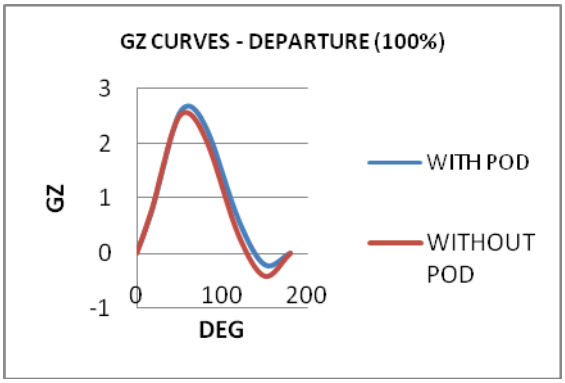

Fig. 8 GZ curves of departure (full load)

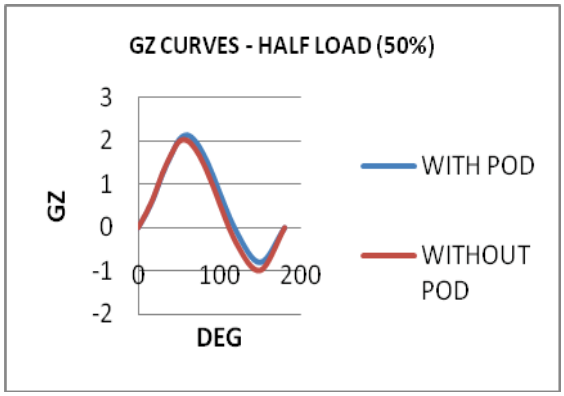

Fig. 9 GZ curves of half load condition

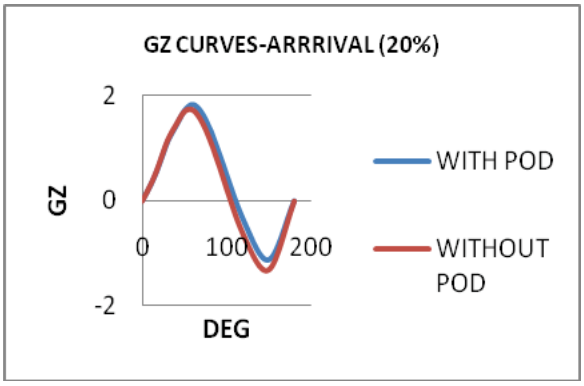

Fig. 10 GZ curves of arrival (20% load)

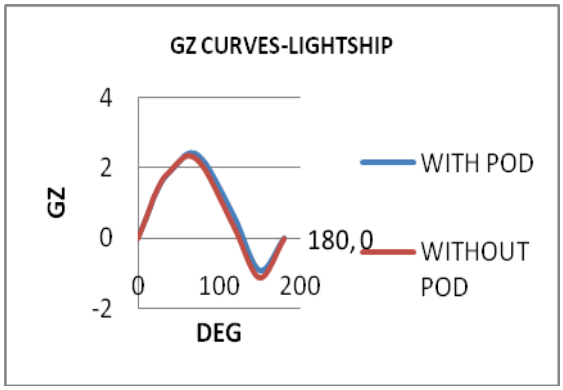

Fig. 11 GZ curves of lightship

The result shows that both hulls fulfil the IMO stability criteria. Based on the graphs plotted, the pattern shows that for all loading conditions, the values of area under GZ curves at angle from 0^0 to 50^0 are almost same. The difference is small and is shown in percentage in table 6 below. The difference of IMO criteria pass for each loading condition is just around 0.2% to 2%. However as the heeling angle increasing and exceed beyond 50^0, the hull with pod shows different pattern. The GZ value for hull with pod is bigger than hull without pod. Since GZ is the indicator for the righting lever, the bigger value of GZ will create bigger

righting moment. Righting moment is the moment that pulls the ship back to its original position after heeling. For analysis on the angle of vanishing stability (AVS), the result shows that hull with pod has better AVS characteristic compare to hull without pod. The comparison is given in table 7 below.

Table 6: Stability result's comparison for both hulls

Condition	Criteria	Percentage pass (%)	
		With pod	Without pod
Departure load (100%)	1	84.67967	85.05435
	2	86.60714	86.89956
	3	90.44586	90.59561
	4	92.55952	92.21487
	5	50	50
	6	93.56223	93.73172
Half load (50%)	1	81.03448	81.66667
	2	83.36414	83.81295
	3	88	88.28125
	4	90.57049	90.0892
	5	50	50
	6	91.74917	92.04666
Arrival load (20%)	1	79.47761	80.21583
	2	81.63265	82.21344
	3	86.48649	86.84211
	4	89.05908	88.47926
	5	50	50
	6	90.99099	91.36442

Table 7: Summary result on angle of vanishing stability, AVS

Loading condition	AVS	
	With pod	Without pod
100%	138^0	130^0
50%	120^0	110^0
20%	110^0	105^0
Lightship	138^0	132^0

From table 7, hull with pod shows the better AVS characteristic. It means that at 100% loading, the maximum angle of heel for hull with pod before her capsizes is 138^0 while for hull without pod is 130^0.

From the stability assessment conducted, the result shows that existence of podded housing at afterward of the hull improved the stability of the hull. The results show that the maximum GZ value for hull with pod is higher than hull without pod. Analysis on angle of vanishing stability also shows that hull with pod have higher value compare to hull without pod.

3. 3 Resistance

The resistance for both hulls are computed using HULLSPEED software and the data input are the lines plan drawings which is drawn by MAXSURF. In HULLSPEED, there are a lot of computational methods available. However not all methods can be used for certain

hull. Based on available methods, the selected method is Fung. It is because the characteristics of both hulls are compatible to be analysed by this method

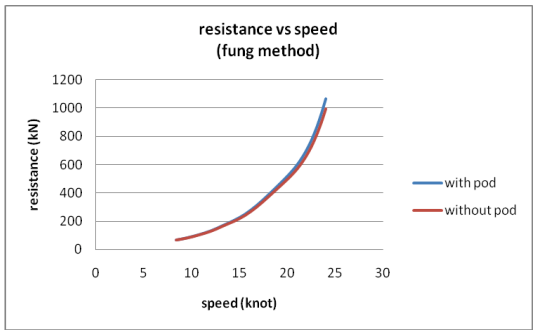

Fig. 12 Resistance comparison graph between hull with and without pod

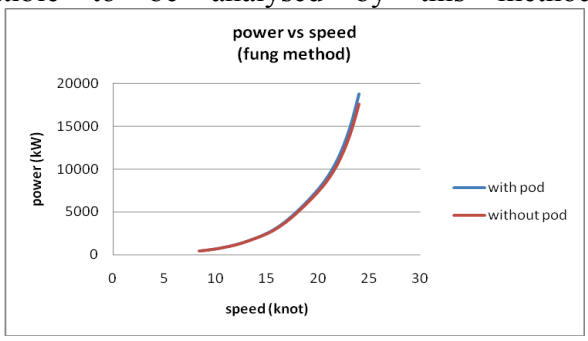

Fig. 13 Power comparison graph between hull with and without pod

From Figure 12 and Figure 13, it is seen that the pattern of curve for effective power is almost same for total resistance. For higher resistance, the power required also high to give a thrust to the hull to move forward at the desired speed. The summaries of result are given Table 10 below. From the table, it is seen that the resistance at lower speed hull without pod is slightly higher than hull with pod. However, the different is small and can be considered as same. At higher speed, the resistance of hull with pod is bigger than the resistance for hull without pod. But the difference of resistance is still small.

Table 10: Summary of resistance analysis result

Speed (knot)	Fn	With pod (kN)	Without pod (kN)	Difference percentage (%)	With pod (kW)	Without pod (kW)	Difference percentage (%)
8.4	0.0485	62.25	69.11	-0.11	402.78	426.65	-0.059
10.2	0.165	92.1	94.43	-0.025	690.44	707.84	-0.025
16.8	0.272	310.65	303.07	0.024	3835.54	3741.94	0.024
20.0	0.330	547.22	525.95	0.0388	8204.1	7885.27	0.0388

For resistance analysis at the design speed (16.8 knots), it can be show as follow:
Resistance of pod only = 2.328 kN
Resistance of bare hull = 303.07 kN
Resistance of bare hull + pod = 310.65 kN
Percentage of pod drag compare to bare hull,
= (2.328 kN/303.07 kN) %
= **7.68%**
Percentage of different between hull with pod and hull without pod,
= (310.65 kN – 303.07 kN) %
= **2.5 %**

From the calculation, the percentage of total pod drag is 7.68% of the bare hull total resistance. The ratio is very small and can be neglected. The sum of the separately measured nominal total resistance (bare hull + pod drag) compared to the directly measured total resistance deviate only approximately 2.5 % from each other. Thus it can be concluded that there are no significant pod – hull interaction.
For analysis in term of total wetted surface area, the calculation can be show as below:
(a–b)/bx100=[(1805.248 m^2-1728.51m^2) /1728.51m^2] %
=4.44%

Where ‘a’ is wetted area of hull with pod and ‘b’ is wetted area hull without pod. The difference is only 4.44%. So, it is seen that existence of pod give additional resistance to the hull especially at the high speed. But the value is very small compare to the other benefit it provides. The resistance is still subjective and depends on the shape and size of the podded housing itself.

4. CONCLUSION

Based on the results obtained, the following conclusions can be drawn:
The podded propulsion improved the stability of the hull and at the same time increase a little total hull resistance. The stability assessments show that both hulls fulfil the minimum requirement of IMO criteria. For hull without pod, the maximum GZ value at full load condition is 2.569 while for hull with pod, the value is 2.689. As the number of GZ bigger, it shows that the stability of the vessel also better. It because GZ is the arbitrary lever that created due to shift of centre of buoyancy during inclined position.
For the value of angle of vanishing stability, AVS, for hull with pod at full load condition, the point is at 138^0 while hull without pod at 130^0. It shows that the hull with pod can face the heeling angle larger than hull without pod.

From theory, hull with pod has higher resistance value due to the additional wetted surface area. Based on result, at the design speed (16.8 knots), the resistance value for hull with pod is 310.65 kN while for hull without pod is only 303.07 kN. The difference between these two values is only about 2.5 %. The value is very small thus it can be concluded that there are no significant pod – hull interaction. For the comparison of resistance of podded housing with the bare hull, it only differs 7.68 %. Even it affects the value of hull resistance, but still the value is very small. However experimental study is required to confirm this fact.

REFERENCES:

1. Hans Klein Woud and Douwe Stapersma, Design of Propulsion and Electric Power Generation System, *Institute of Marine Engineers*, UK, 2002.
2. Kvaerner, ABB and Wärtsilä NSD, Annual Report of Efficient Ship Machinery Arrangement Project (ESMA), Shafts vs Pod- Comparison Between A Conventional Shaft Line and a Podded Drive in a Fantasy Class Cruise Ship, *NFR Project No. 125942/230*, 1999.
3. Timothy J. McCoy, Trends in Ship Electric Propulsion, *Power Engineering Society Summer Meeting, IEEE*, Vol. 1, 2002, pp. 343-346.
4. Cornelia Heinke, Hans-Jürgen Heinke, Investigations About the use of Podded Drives for Fast Ships, *The Seventh International Conference on Fast Sea Tra*nsportation, Ischia (Italy), 2003.
5. Heikki Helasharju, Alaska Region Research Vessel -Calm Water Model Tests For Propulsive Performance Prediction, *VTT Technical Research Centre, Finland,* 2002.
6. Jane’s Fighting Ship edition 2004/2005
7. A.B Biran, Ship Hydrostatic and Stability, *Butterworth-Heinemann (BH*), 2003.

Proceedings of the 4th BSME-ASME International Conference on Thermal Engineering
27-29 December, 2008, Dhaka, Bangladesh

DISINTEGRATION OF A SQUARE CYLINDRICAL LIQUID COLUMN

Mohammad Ali*1, A. Umemura*2 and A K M Sadrul Islam*3

*1 Department of Mechanical Engineering, BUET, Dhaka, Bangladesh
*2 Department of Aerospace Engineering, Nagoya University, Nagoya, Japan
*3 Department of Mechanical and Chemical Engineering, IUT, Gazipur, Bangladesh
email: mali@me.buet.ac.bd

ABSTRACT

This paper describes the disintegration and capillary instability during the contraction of a square cylindrical liquid column. The breakup behavior for the present configuration of the liquid column is investigated and found some significant differences from those predicted by conventional jet atomization theories. The numeric illustrates the underlying physics during relaxation of the liquid cylinder, formation of capillary wave, its propagation and disintegration of liquid column. The formation of capillary wave is initiated by the surface tension on the sharp edge of the square end of the cylinder and the propagation of the wave occurs due to the effect of surface tension force on the motion of the fluid. The investigation reveals that before disintegration of the liquid the capillary waves become unstable and the source of making the wave unstable is inherently developed by the system.

KEYWORDS: *Disintegration, Capillary wave, Instability, Liquid column, Jet atomization.*

1. INTRODUCTION

In liquid jet atomization capillary instability and disintegration of liquid are important and interesting phenomena to the fluid dynamists. An earlier account of the work is summarized by Rayleigh [1] who performed a delightful discussion on jet instability and published both theoretical and experimental results on capillary instability phenomena. During the contraction of liquid jet or cylindrical liquid drop the capillary waves are radiated on the fluid interfaces. These waves are caused by surface tension and generated at the tip of liquid jet. In an experiment Goedde and Yuen [2] examined the capillary instability of vertical liquid jets of different viscosities and measured the growth rates of waves for disturbances of various wavelengths. The author discussed about the drop formation and ligament detachment. In another investigation Donnelly and Glaberson [3] performed some experiments and discussed the effects of viscosity on the capillary instability and growth rate.

Recently Umemura et al. [4,5] performed a series of experiments on liquid jet atomization problem and obtained a new concept on capillary instability and liquid jet breakup processes. In present study a three-dimensional numerical code is developed and validated with experimental data. The code is then used for numerical simulation to understand the phenomena of capillary waves radiated from the tip of the square liquid column in an otherwise quiescent fluid and its disintegration processes.

2. NUMERICAL FORMULATION

To understand the phenomena of capillary instability on the liquid surface and the disintegration processes of cylindrical liquid column, a numerical algorithm has been developed which is used to solve time dependent three-dimensional Navier-Stokes equations with surface tension force. The algorithm can capture the capillary waves radiated on the surface of cylindrical liquid column. For the simulation, volume-of-fluid (VOF) method with a fixed, regular, uniform grid is used to solve the problem. The treatment of surface tension consists of artificially smoothing the discontinuity present at the interface is a Continuum Surface Force (CSF) manner [6].

3. PROBLEM STATEMENT AND BOUNDARY CONDITIONS

A three-dimensional numerical scheme is used to simulate the contraction of a square cylindrical liquid column in an otherwise quiescent gas as well as the capillary waves formed on the liquid gas interfaces. The width of the cylinder is 2.2×10^{-4} m and the column length and width ratio is 17.32. The average radius of the cylinder is calculated as the square root of (cross sectional area/π) and denoted as "a". Sulfur hexafluoride (SF_6) of critical temperature, 318.7 K and critical pressure, 3.76 MPa is used as liquid. Gaseous nitrogen is used as immiscible, viscous fluid with pressure of 7.0 MPa. The rectangular coordinate system has been considered for this calculation. The grids are cubic and uniform in the whole calculation domain. The width of calculation domain is eight times larger than the half width of liquid column. As the liquid column contracts, only a few grid points have been considered beyond the shrinkage end of the column. The other end of the column coincides with the domain boundary on which symmetric boundary conditions are imposed. Therefore contraction of liquid column is observed from one end. Solid boundary conditions are imposed on other boundaries of the calculation domain.

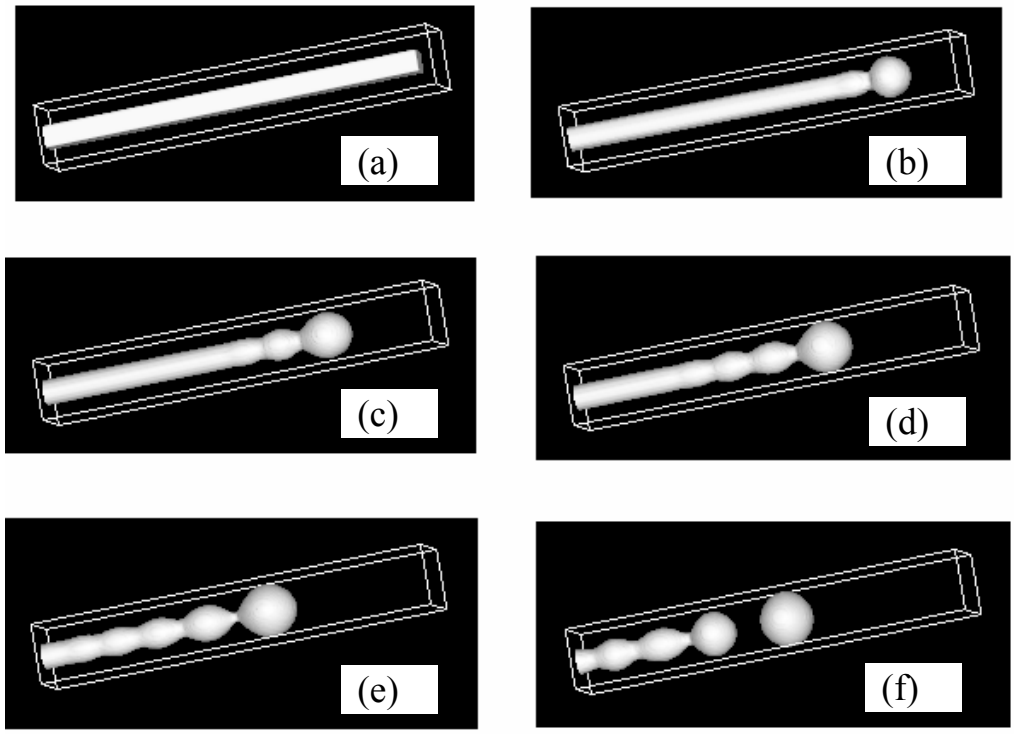

Fig.1 Evolution of capillary wave and liquid disintegration; (a) At dimensionless time, t=0.0, (b) t=4.2, (c) t=8.4, (d) t=12.6, (e) t=16.8 (f) t= 21.0

4. RESULTS AND DISCUSSION

4.1 Capillary Wave and Disintegration of Liquid Column

The time evolution history of capillary wave and droplet formation during the contraction of liquid cylinder is shown in Fig.1. The dimensionless time reported here has been calculated as the ratio of real time and the timescale, $t_c = \sqrt{\frac{\rho_l a^3}{\sigma}}$, where ρ_l is the density of liquid, a the average radius of the liquid cylinder and σ, the surface tension. Here the dimensionless time is denoted by "t". Initially the tip of the liquid cylinder is rectangular in shape. Due to surface tension the cubic end of liquid cylinder changes gradually and forms capillary wave and a bulbous end. From the beginning of calculation the formation of capillary wave starts and a complete wave including swell and neck forms at about dimensionless time, t=1.4. The wave then propagates and generates second wave at time, t=2.82. The propagation time for second wave is shorter than that for third, fourth and fifth wave. The time interval for third, fourth and fifth wave is almost same after generation of second wave and it is equal to the dimensionless time of

4.23. This uneven time interval for wave propagation is caused by the surface tension force at the end of liquid cylinder. The amplitude of the first wave (tip wave) gradually becomes larger and forms a droplet at t=18.2. It has been observed that the growth of swell and neck of the droplet is not uniform. An exponential growth of both swell and neck can be found during the relaxation process of the liquid cylinder. However by a close observation it has been revealed that the breakup does not occur unless and until the capillary wave reaches to the symmetric end of the liquid cylinder. The arrival of capillary wave to the end of the column causes a disturbance in the process and makes the capillary wave unstable and eventually breakup occurs. This instability of the wave can be understood by rapid changes of the amplitudes as shown in Fig.2. The diameter of the first droplet is 2.12 times larger than the average diameter of the liquid cylinder. Three consecutive waves including tip wave are considered to observe the instability and the variation of amplitude. Here the amplitude is denoted as "A" measured from undisturbed surface formed by average diameter of the cylindrical liquid column and is considered as positive for swell and negative for neck. The capillary wave initiated from the tip of cylinder reaches to the symmetric end of the cylinder at t=15.4. Instability occurs after this time and therefore, to observe the instability the amplitudes from time 9.0 are plotted in Fig.2. It can be observed that the amplitude of the first swell (tip wave) is always much larger than that of the following swells of the waves which is caused by the effect of liquid column shape at the end. We can see that after time, t=16.0 the amplitudes of both swell and neck of all waves grows faster than previous. The neck of the first wave which is the farthest away from symmetric end of the liquid cylinder grows much faster and makes a droplet at time, t=18.2. The amplitudes of waves in longer distance grow faster than that in shorter distance which is the characteristics of the unstable waves. It can also be observed that before time, t=16.0 the growing rate of first swell becomes lower which indicates that the pinching process is just lapsing time for unstable waves. Once the system becomes unstable, the instability of the waves expedites the liquid disintegration process. This self-excitation of the instability is different from conventional jet instability theory.

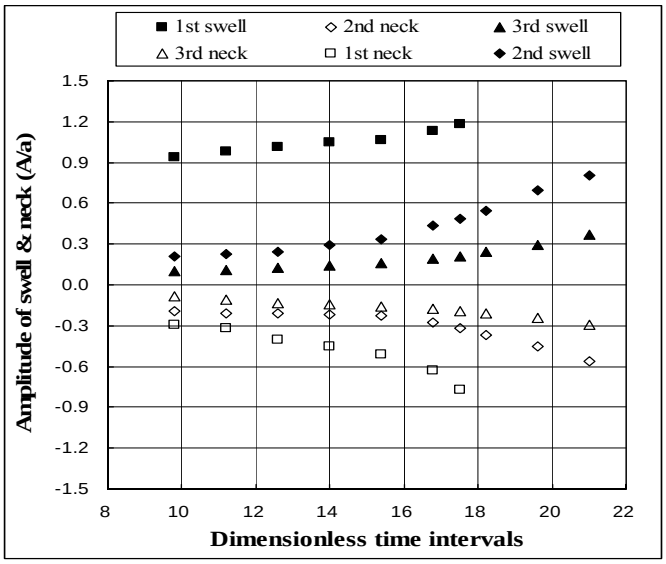

Fig.2 Variation of wave amplitudes with different time intervals

4.2 Characteristics of Capillary Wave

Figure 3 shows the evolution of wave profiles with time for the first three waves. The profiles of different waves are drawn on the basis of their propagation time. The evolution time of different wave profiles is counted from the trace out moment of that wave. The wave profiles are observed at time t=4.1~14.1 with equal time interval between the adjacent profile to study the shape of the wave at different times and the growth of swell and neck. The height of wave profile denoted by A_x at different position along the wave length is normalized by average radius of the liquid column. To plot the profiles, only half of the wave length is considered. Though the wave lengths of various waves are not equal, the distance along the wave length is normalized by the half wave length to make it unity. From Fig.3 we can see that for all waves the swells are broad and the necks are narrow, and for first wave (tip wave) the swell is much broader than the other waves. Figure 3(a) shows that though initially the span of neck is

about one third of that of swell, with time being the span of neck broadens narrowing the span of the swell. For second and third waves as shown in Figs.3(b) and (c) we can see that the neck broadens with nodal point moving inward of the swell. During the evolution the nodal point for second wave remains fixed near the distance 3/5 of the wave length from swell side and for third wave the nodal point is very clear which moves more inward of the swell and remains fixed exactly at distance 3/5 of the wave length from swell side. In general the swell grows faster than the neck and for the swell the growing rate increases with time except for the wave profile at time t=14.1 of the first wave as shown in Fig. 3(a). Another observation is that the amplitude of the first wave is always much higher than that of the other waves which is caused by the surface tension force at the contraction end of liquid column. Gradually the amplitude decreases for the later waves, which is caused by the effect of viscosity.

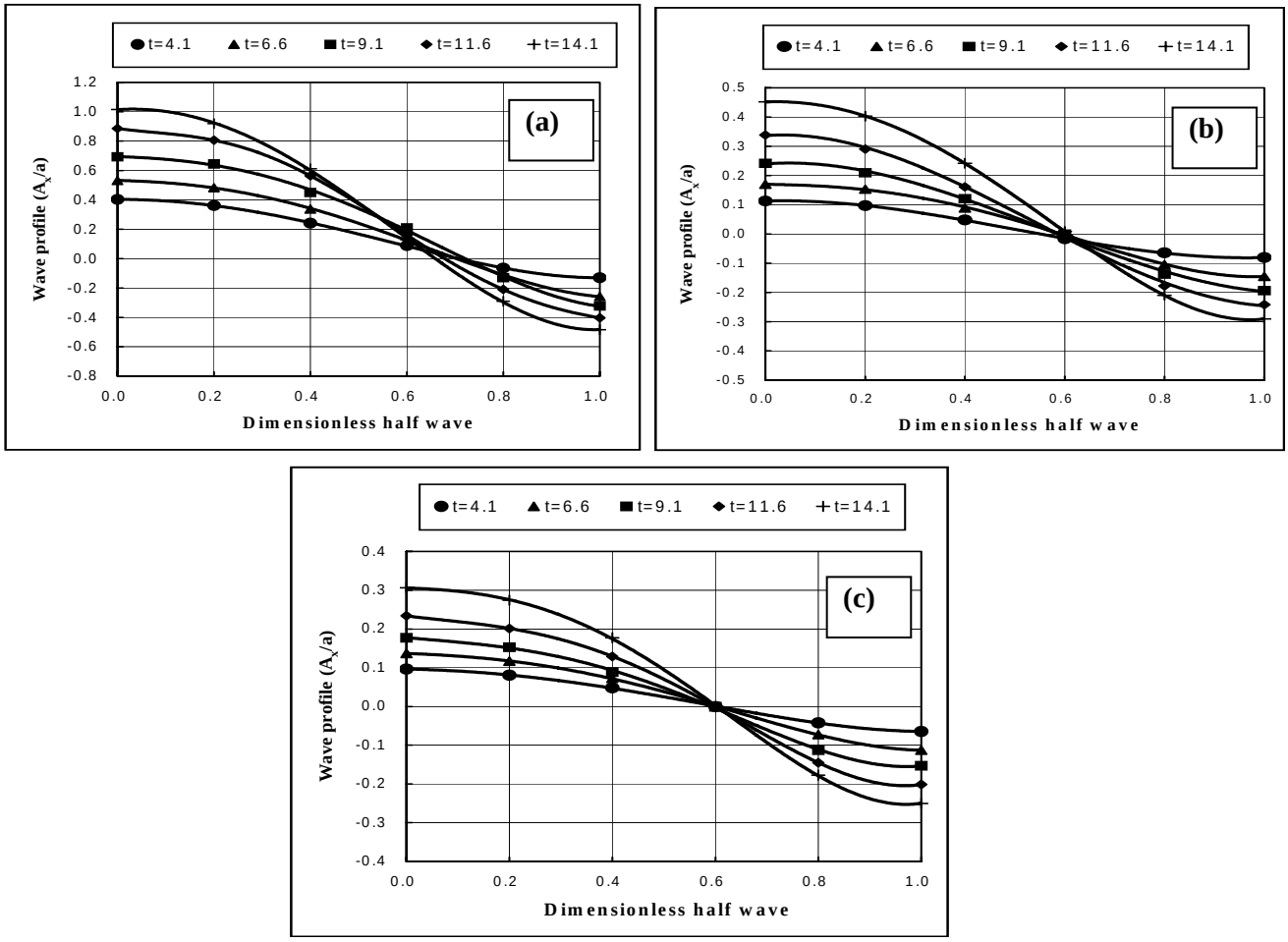

Fig.3 Variation of wave profiles with different times; (a) First wave (tip wave), (b) Second wave, and (c) Third wave

Figure 4 shows the variation of pressure along the horizontal axis of liquid cylinder at time t=14.1 when few capillary waves have already been formed. The pressure on the central axis at different position of capillary waves can be understood from this figure. In fact the surface tension force causes pressure variation in the liquid and eventually produces fluid motion and capillary waves. For easy understanding about the variation of pressure and its effect on the motion of the fluid, the velocity along the axis of the liquid column and the velocity vector at the mid-plane are drawn in Figs. 5 and 6, respectively. Figure 4 shows the pressure of liquid taking the gas pressure as reference. No doubt the liquid pressure is always higher than the gas pressure and the pressure varies within the liquid depending on the surface tension force and fluid motion. Due to variation of pressure, motion of the fluid occurs and accordingly from Figs. 4 and 5 we can see that at the position of peak pressure the motion of fluid is almost zero, from this position of peak pressure motion of fluid starts towards opposite direction and horizontal velocity attains peak value towards both right and left of the peak pressure as shown in Fig.5. It can be pointed out that the maximum pressure in liquid occurs at immediate behind (left side) of the first neck and the bulbous

region has the lowest pressure. After the bulbous region several peak values on both high pressure and low pressure sides can be found in Fig.4. The peak value of pressure is caused by surface tension and fluid motion. The overall fluid motion can be understood from Fig.6 which shows a part of velocity vector plane of the fluid through horizontal axis of the liquid cylinder. Both vector length and color represent the magnitude of the velocity. The red color indicates the maximum velocity which is equal to 48 mm/sec. From this figure we can see that at the trough of every neck there is a vortex. The inertia force of the fluid motion in vortex increases the pressure with surface tension force at immediate behind of the trough of the neck. The inertia force of the fluid motion in same vortex as shown in Fig. 6 works to the outward direction of the cylinder at immediate right side of the trough of the neck and decreases the pressure and eventually causes the lowest peak pressure as shown in Fig.4. The peak value of both high and low pressure gradually decreases with the decrease of wave amplitudes for both swells and necks. The decrease of peak pressure is the consequences of increase in radius of curvature and decrease in the fluid motion as can be found in Fig.5. Similarly the peak values of horizontal velocity towards both positive and negative directions decrease with the decrease of amplitudes which decreases the narrowness of the neck and width of the swell. The decrease of horizontal velocity is the consequences of conservation of mass.

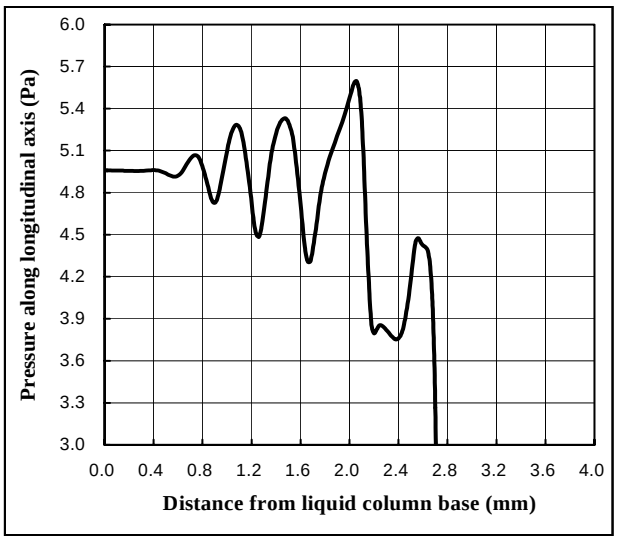

Fig.4 Variation of pressure along the longitudinal axis of liquid column at t = 14.1.

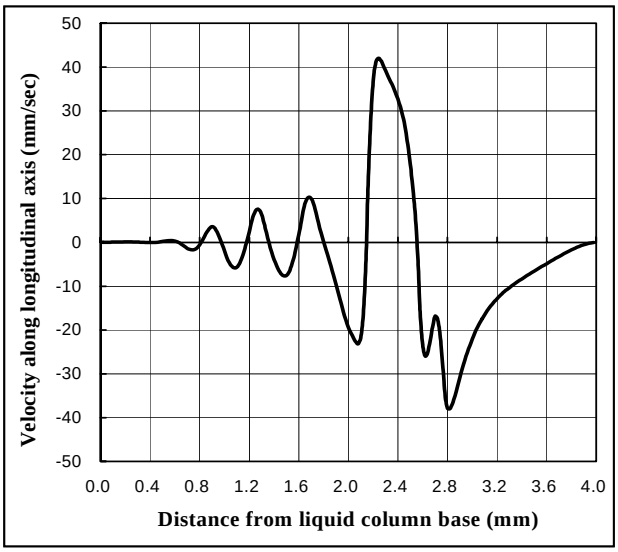

Fig.5 Velocity profile along the longitudinal axis of liquid column at t = 14.1.

5. CONCLUSIONS

The capillary instability and breakup characteristics are studied during relaxation of a square cylindrical liquid column. Calculation shows that capillary wave generates from the tip of liquid cylinder and evolution of the tip wave depends on the shape of the cylinder tip. From the initial stage the swell-growth of the first wave (tip wave) is much higher than that of later waves which is caused by the surface tension force on the shape of the liquid cylinder tip. The propagation of capillary waves to the base of the column causes a disturbance on the system and makes the wave unstable. Due to instability of the wave the amplitudes of both swell and neck grow rapidly and eventually pinch-off occurs. Wave profiles show that in general the span of neck from nodal point is shorter than that of swell and the span of first neck is much shorter than that of the other necks. Depending on the motion of fluid and surface tension, pressure along the longitudinal axis of liquid cylinder fluctuates and peak values of both low and high pressure sides decrease with the decrease of amplitudes of both swell and neck. Immediately before liquid breakup, horizontal velocity in neck increases rapidly which causes rapid pressure drop in the neck and enhances the disintegration of liquid droplet.

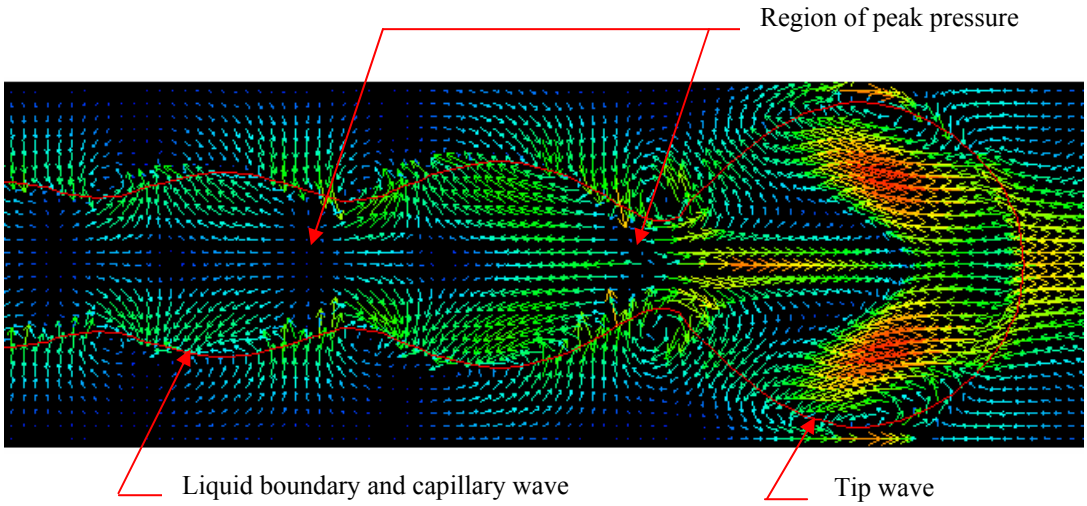

Fig.6 A part of velocity vector plane through longitudinal axis of liquid cylinder at t = 14.1.

6. REFERENCES

[1] Rayleigh, L. On the Capillary Phenomena of Jets. Proceedings of the Royal Society of London, 29 (1879), pp.71-97.

[2] Goedde, E. F. and Yuen, M. C. Experiments on Liquid Jet Instability. *J Fluid Mech.*, 40(3) (1970), pp. 495-511.

[3] Donnelly, R. J. and Glaberson, W. Experiments on the Capillary instability of a liquid Jet. Proceedings of the Royal Society of London, Series A, 290 (1966), pp. 547-556.

[4] Umemura, A. Micro-gravity Study on Instability of Near Critical Mixing Surface jet (Mechanisms of Rayleigh-Taylor Instability) Excitation at Nozzle Exit and Short Spacing Disintegration. *J Combustion Society of Japan*, 46(135) (2004), pp. 50-59 (in Japanese).

[5] Umemura, A. and Wakashima, Y. Atomization Regimes of a Round Liquid Jet with Near-Critical Mixing Surface at High Pressure. Proceedings of the Combustion Institute, 29 (2002), pp. 633-640.

[6] Brackbill, J. U. Kothe, D. B. and Zemach, C. A Continuum Method for Modeling Surface Tension. *J Computational Physics,* 100, pp. 335-354.

"Proceedings of the 4th BSME-ASME International Conference on Thermal Engineering
27-29 December, 2008, Dhaka, Bangladesh"

HYDRAULIC LOSS REDUCTION IN HYDRO GENERATOR STATOR VENTILATION DESIGNS VIA EXPERIMENTS AND CFD ANALYSIS

[1]G.Chella Rao, [2]N.Gunabushanam, [3]N.Govindarajulu, [4]T.k.k.Reddy
[1]Research Fellow, Satyam computers services Ltd, Hyderabad
[2]Formal G.M, BHEL R&D,Hyderabad
[3,4]Professors, Jawaharlal Nehru Technological University, Hyderabad, India
e-mail: chellarao@yahoo.com

ABSTRACT

This paper presents a set of experiments and analytical solutions for hydro generator ventilation system. Ventilation losses, because of their great share in total losses, have remarkable influence on the energetic performances of hydro generators. Windage losses constitute around 40 to 45% of the total losses. Any effort to minimize the windage losses boost up the efficiency of hydro generator. On the basis of experimental investigations and computational models the most significant impact parameters identified to determine the ventilation losses of air-cooled hydro generators. It is found from the experiments about 80% of total losses occur only in the entrance of the stator part i.e wedge zone of the machine. New wedge and spacer models have been evolved to minimize these losses by selecting various models and combinations. The test results obtained have been compared with Analytical solutions using CFD package 'Fluent'. These results indicated there are certain critical zones between the wedge, spacer and slot where reverse and stagnation flows can occur. The results obtained using CFD have matched well with experiments. . It is concluded that these losses can be brought down considerably which would result in improvement in efficiency of the Hydro generator even to the extent of 0.2 to 0.3%. The improvement in the efficiency can result in overall savings of investment in the power and also it enhances considerably to upgrade the hydro power generation of the Nation without doing the major modifications of the existing power plants.

KEY WORDS: *Hydro generator, Hydraulic resistance, CFD, Spacer, Wedges*

1. INTRODUCTION

Many hydro generators in use today suffer from poorly designed ventilation (cooling) systems. The cooling air is misdirected, underutilized and propelled by inefficient and loss creating fans. It is not unusual for our systems to reduce airflow, the temperature of heat producing parts and power losses. The major components of a typical Hydro generator are Rotor, Stator, Conductor, End winding, Wedges, Cooling fan, and Coolers. Stator is cylindrical in shape. The stator is made of laminated packets. Spacers are arranged between two laminated packets to form the cooling passages. The inner periphery of stator is provided with wedge slots. This wedge being a structural member withstands the vibrations created in stator part and at the same time acts as a guiding element to the flow of cooling medium. Air gap of 20 to 25mm is usually provided between the rotor and the stator. Fans are mounted on the rotor to supply air for cooling purposes. The design of a good ventilation system plays an important role in the performance of generator. In a medium capacity generator, the fans are mounted on the rotor and powered by the generator itself. If there is high pressure loss in the ventilation system then the fan consumes more power which reduces the generator output.

The reduction of pressure drop in the machine effects the fan power requirement. In order to minimize pressure drop for a given volumetric flow rate, it is necessary to optimize the ventilation components.

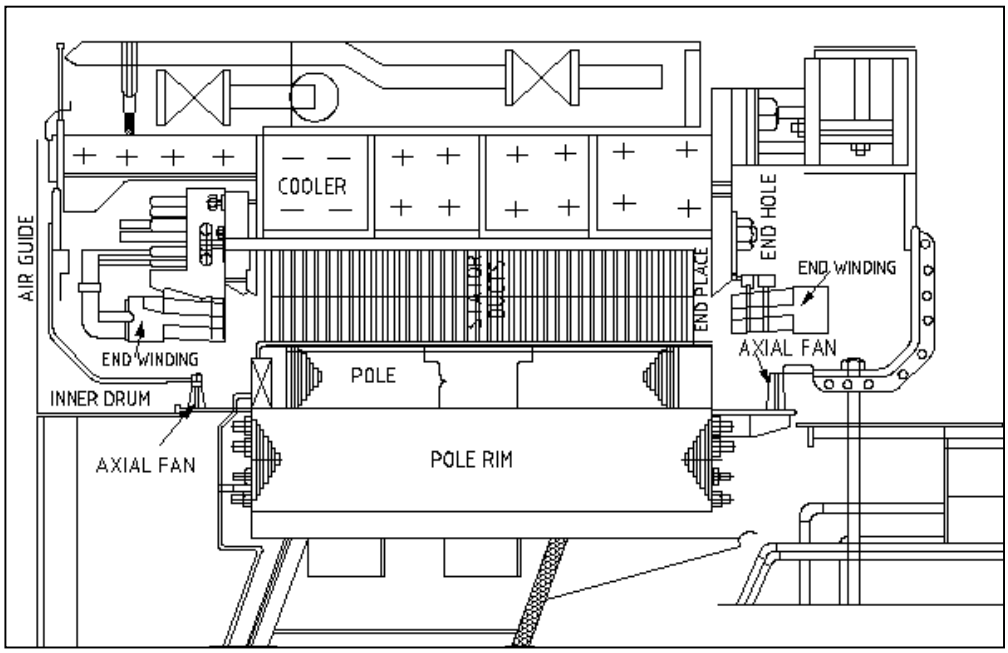

Fig:1, Hydro generator Cross section and Ventilation

Typical cross section and ventilation is shown in Fig(1). Two fans are mounted on the rotor and the air (cooling medium) is in circulation in three paths.

a) Air from main fan passes through stator over hang, end holes and enters into the cooler.
b) Air from main fan enters end fingers and directly discharged into the coolers.
c) In addition rotor acts as a fan and the pressure created causes the air to pass through inter polar gaps, the stator radial ducts and to coolers.

The air passages in these paths are adjusted such that flow in each path is sufficient to cool the stator winding in that path. All these three paths take the heat from the machine and finally pass through the coolers.

1.1. Pressure drop analysis in stator core

In stator core the pressure of cooling medium drops due to boundary layer effects, frictional effects and also due to the presence of various contours (i.e. Contractions, Expansions, Bends, Obstructions etc). A fan used in ventilation system has to overcome the total pressure drops in the active parts of stator, which accounts for 65% and above of the total available pressure. The various sections, which contribute for pressure drops in hydro generator, are

1) Stator end enclosure: here pressure drop consists of frictional losses, Impulse losses, Frictional losses can be neglected compared to Impact losses.
2) End windings enclosure: here the static pressure difference is very small. A uniform flow distribution over the end windings is needed. Proper fan arrangement will reduce these losses.

3) Stator core: Major losses in stator core are Impulse loss at inlet, Wall friction losses in duct, losses due to geometry bends, Impulse losses at out let.

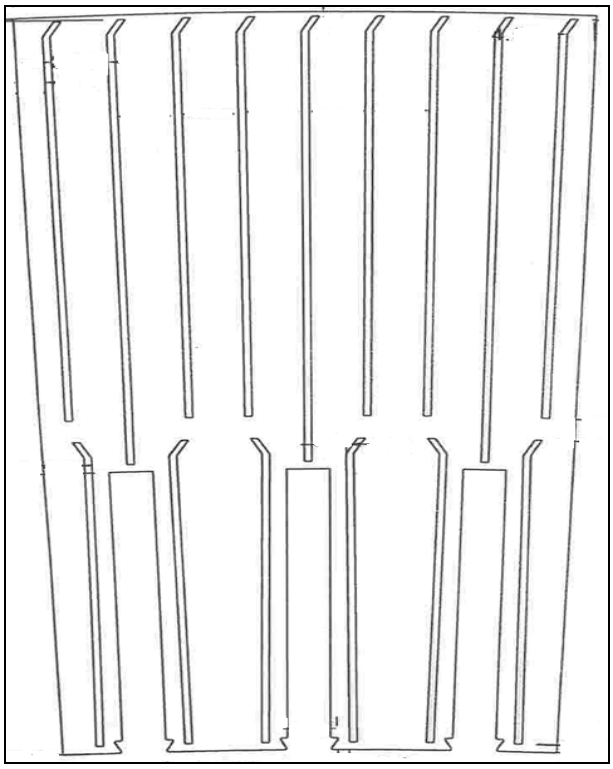

Fig:2, Stator spacer Configuration

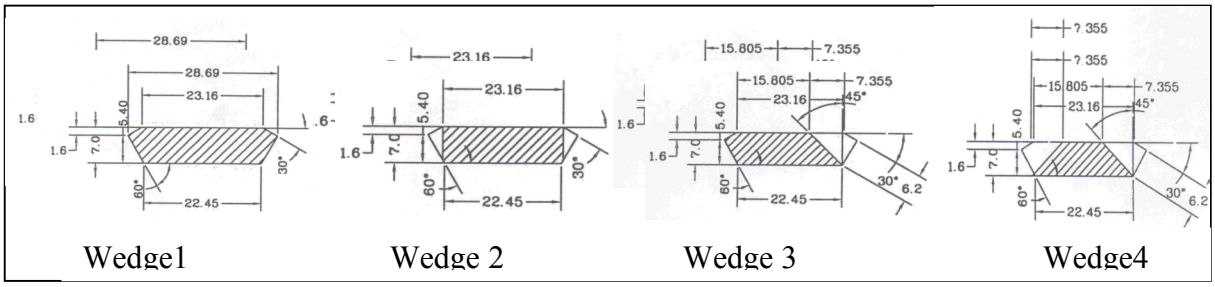

Fig:3, Different Wedge Shapes

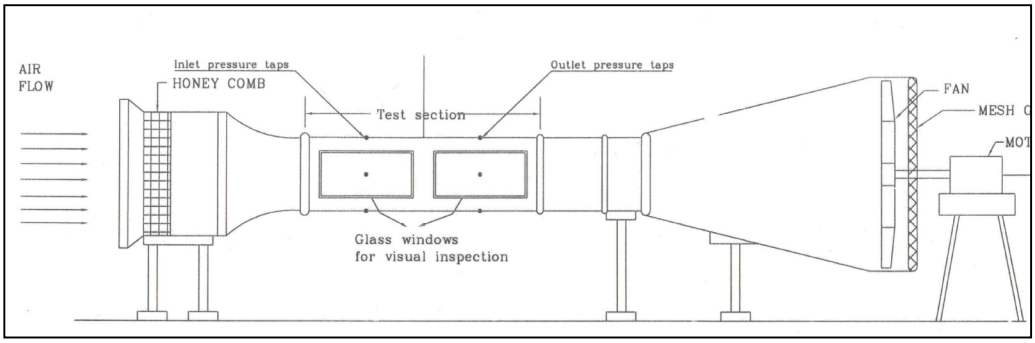

Fig:4, Experimental Set up

2. EXPERIMENTAL SETUP AND PROCEDURE

2.1 Model description

A part model of hydro generator stator is manufactured. This model consists of 7 stator segments (48.1 mm thick), each separated by spacers (4x6 mm). Each segment consists of 3 conductor slots in which conductor blocks are fitted. All the 7 packets are bolted by screw fastenings. 4 types of wedge shapes with different types of slopes and cuts are made shown in Fig 3 .

2.2. Details of test

The test rig is consists of a Honey comb, a test section and a D.C.Motor blower. Various velocities can be set at the inlet to model by varying the speed of the D.C.Motor and for the given model the maximum velocity obtainable is 40 m/sec.

2.3 Instrumentation

A total of 90 pressure tap locations are identified, and accordingly holes of 1mm diameter are drilled along the width of packet. Static pressure probes are placed at wedge, tooth and core parts. Copper hypodermic tubes of 1mm ID are carefully embedded and taken out of packets from backside. To avoid any flow disturbances in the subsequent packets, the copper tubes are embedded in the packet and the surface is leveled smoothly by a chemical paste. The model is placed in the wind tunnel, and PVC tubes of 1.6mm ID are connected to each cooper tube. These PVC tubes are taken out of the wind tunnel and connected to channel selectors, and in turn to digital micro manometer and data logger.

2.4 Velocity Measurement

The duct passage is an expanding passage in which the velocity of the fluid changes. The analysis based on static pressure does not show the actual behavior. Hence total pressure is evaluated by calculating the velocity at various sections. Velocity of airflow in the tunnel is measured just before the model using a Hot wire electronic velocity meter.

2.5 Testing procedure and Evaluation of Hydraulic loss coefficient

To evaluate the hydraulic loss factors for stator- spacer layout in Fig (2) with 4 types of wedge shapes at different air velocities ranging from 5 to 35 m/sec. The air is drawn into the test section using the blower. Velocity readings at 45 locations just before the model are measured using Velocity meter.

Let F : Impulse Force (Newton), ρ : Density (Kg / m^3), A: Area (m^2), V: Velocity(m/sec)
C : Constant of proportionality (Dimensionless),
K: Coefficient of hydraulic resistance
(Dimensionless),
Δp = Pressure drop (mmwg)
Pressure drop in the flow is given by

$$\Delta p = F / A$$

$$\Delta p = \rho V^2 C$$

$$K = (2g \Delta p) / \rho V^2$$

Here Δp is considered as total head drop in various sections and density ρ is taken at 21.1^0c.

3. ANALYTICAL MODEL

The main application of CFD methods lies in the simulation of the air flow of representative hydro generators. For several combinations of parameters such as geometry and air flow characteristics, the relevant values of velocities, pressure differences, windage losses are calculated. Using these results, it is possible to improve the conventional design programs which are used for fast design decisions and the arbitration between design alternatives. For the main interesting parts such as stator ventilation ducts, wedges, rotor (rim ducts and poles), air gap. A part model of hydro generator stator packet is modeled and simulated for different velocity and design combinations using CFD package Fluent. From the simulation the physical behavior of air flow inside the stator ducts has reported and it will helps in avoiding the stagnation zones.

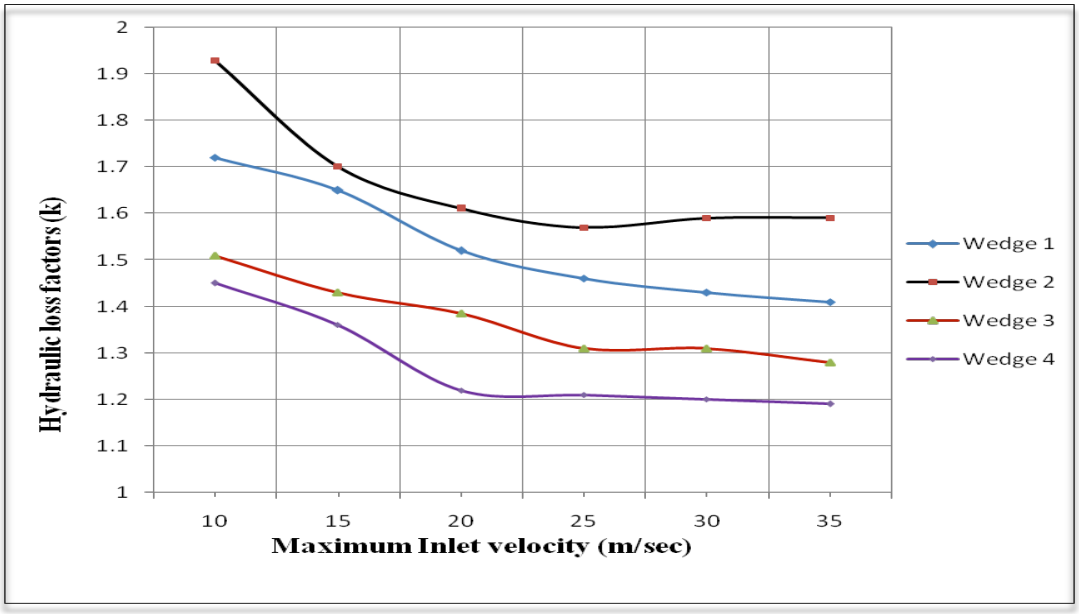

Fig: 5, Hydraulic Lossfactors Vs Maximum inlet velocity

4. EXPERIMENTAL RESULTS AND DISCUSSIONS

The overall hydraulic loss factor (k) is calculated for all 4 types of wedge shapes at different velocities ranging from 10 m/sec to 35 m/s. This factor K includes the entry and exit losses because the pressure probes are placed 10mm to 15mm before and after the model. Hydraulic loss factor for different wedge shapes with respect to various inlet velocities shown in Fig :5. Wedge shape 1 has no cuts or slopes rather it is a simple type and can be considered as basic shape for comparison. At a medium velocity of 25 m/s, it has given a loss factor K= 1.46. The range of velocity at the wedge for a normal machine is 25-30 m/s. Wedge shape 2 has straight cuts on both sides and has given a loss factor k=1.57 at velocity 25 m/s. This trend is observed in wedges 1 and 2. Hence it can be concluded that the presence of cuts on both sides are giving adverse results. In view of the above observation the wedge shape 4 is made by providing a complete slope of 45 deg on one side and no cut on the other side. This wedge has given a loss factor of 1.31 a reduction of 11% compared to wedge 1 is shown in TABLE 1 and reduction of 20% in hydraulic loss factor compared to wedge 2 at 25 m/s. Hence it is observed that there is a limitation for the slope angle. When angle increases above 450 , the

loss factor also increases. This is because the air has to deflect more at higher angles, which results in more losses. Keeping in view the performance of the above 3 wedge shapes and the effects of straight cuts and slopes, wedge shape 4 has been developed by providing 450 complete slopes on both sides which gave a loss factor of 1.21 at 25 m/sec a reduction of 17.5% compared to wedge shape1 and 23%compared to wedge shape2. From this experimental analysis it can be concluded that by modifying the wedge shape a reduction of 15 to 25% in overall hydraulic loss factor can be achieved. In the stator duct passage the maximum pressure drop occurs in the wedge and tooth zone. Hence any effort to minimize these losses will greatly enhance the efficiency of the generator.
The CFD analysis indicates a possibility of occurrence of reverse and stagnation flows near the wedge zone if the wedge shapes are not designed properly. This situation may lead to burn out of the conductor windings at that place. Hence a proper design of wedge shape is very important to cool the windings properly.

5. CONCLUSIONS

Detailed experiments have been carried out on the model with different wedge shapes for velocities ranging from 5 m/s to 35 m/s. The experiments have revealed that the major losses takes place in the wedge zone only and any modification in this zone will improve the performance of the ventilation system. 4 types of wedge shapes with cuts and slopes of different angles are used in the analysis. It is observed that by providing straight cut (at one side or both sides) is increasing losses. Providing slope is increasing the flow and reducing the losses because air glides over the slope and enters the duct smoothly. At an average velocity of 20 to 25 m/s for all the wedge shapes, it is observed that 60% to 70% of losses occur at wedge zone only. The wedge losses are increasing with increasing in inlet velocity. Wedge shapes 3, 4 are given better results .The presence of slopes(45 degree on both sides) make the wedge 4 week considerably in the duct zone. As wedge acts as a structural member and has to withstand the vibrations, the strength of the wedge in the duct zone cannot be overlooked. Hence wedge 3 could be the best option.
The CFD analysis indicates a possibility of occurrence of reverse and stagnation flows near the wedge zone if the wedge shapes are not designed properly. This situation may lead to born out of the machine. Hence a proper design of wedge shape is very important.

6. REFERENCES

[1] J.H.Walker, “Large A.C.Machines design manufacturing and operation”
[2] FUJI electric Review “ Improvrment of generator efficiency” (1982)Volume 28 p 52-58
[3] BHEL Manual 1995 “ Ventilation and Heat Transfer of electrical machines”
[4] BHEL Manual 1996 “ Ventilation and Cooling in electrical machines”
[5] ESDU Engg Data Book “ Fluid Mechanics and Internal Flows
[6] G.K.Ridley, GEC Review, 1988 Vol 4, p 2.
[7] ABB Review 1995, Vol 10, P23 “ Power plant service –a new concept for faster Retrofitting of turbo Generators”

Proceedings of the 4th BSME-ASME International Conference on Thermal Engineering
27-29 December, 2008, Dhaka, Bangladesh

EXPERIMENTAL STUDY OF A CLOSED WET COOLING TOWER WITH MULTI PATH

G. J. Shim [1], M. M. A. Sarker[2], S. M. Baek [1], H. S. LEE [3], E. P. Kim [3], J. I.Yoon[3]

[1] Department of Refrigeration and Air-Conditioning Engineering, Graduate School, Pukyong National University, Namgu, Pusan 608-739, South Korea.
[2] Department of Mathematics, Bangladesh University of Engineering and Technology, Dhaka-100, Bangladesh
E-mail: masarker@math.buet.ac.bd
[3] School of Mechanical Engineering, Pukyong National University, Namgu, Pusan 608-739, South Korea.

ABSTRACT

The performance of closed-wet cooling tower (CWCT) having a rated capacity of 2RT have been studied experimentally. The test section has multi path those have been used as the entrance of cooling water that flows from top part of a heat exchanger. The heat exchanger consists of 19.05mm tubes with eight rows and twelve columns and the coils are in staggered arrangement. In this experiment, heat and mass transfer coefficients and temperature ranges were calculated with several variations including multi path. The results indicated that CWCT operating with two paths has higher values of heat and mass transfer coefficients than with one path.

Keywords: *Multi path, Cooling capacity, Wet-bulb temperature, Transverse pitch.*

1. INTRODUCTION

Cooling towers are used frequently to reject heat from an industrial system or process without thermally polluting surface water. In general, cooling towers are classified into open and closed type [5]. Open cooling towers expose the water directly to the atmosphere and transfers source heat load directly to the air causing the air pollution. The other type, called closed circuit cooling tower that maintains an indirect contact between fluid and atmosphere and are being used increasingly due to the non pollution of cooling water or air [6].

Parker and Treybal [1], Mizushina et al. [2] and Nitsu et al. [3] conducted experimental studies of closed circuit cooling tower and proposed correlations of heat and mass transfer coefficients as a function of diameter of tube.

In a closed-wet cooling tower (CWCT), cooling water and spray water circulation pumps and fans are the prime factors responsible for power consumption. A cooling water pump consumes 60 to 70 % of total power consumption [7-8]. Due to this energy consumption concerns, it is required to design the CWCT in such a way that the quantity of cooling water can be decreased. In an efficient design, one can curtail expenditure incurred by coils by reducing the quantity of cooling water. In that case, the cooling capacity could be a bit low if it is applied to typical CWCT with one path, because the velocity of process fluid in the tubes decreases. To increase the velocity of the process fluid in the tube, blocking tubes can be installed in the heat exchanger in multi path system. Fig. 1 shows the concept of multi path.

In the relevant literature, no results have been reported so far involving the CWCT with multi path. In this scenario, the objective of this paper is to obtain basic data from this experimental study on a small-size CWCT with multi path and analyze the performance characteristics.

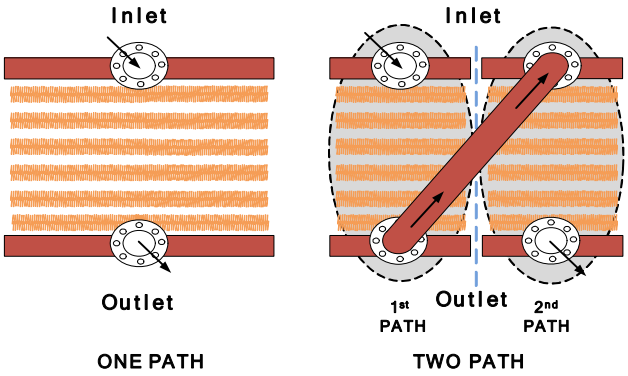

Fig. 1: Concept of multi path

2. EXPERIMENTAL SETUP AND PROCEDURE

The schematic and photograph of the experimental apparatus used in this study are shown in Fig. 2. In the experiment, the prototype CWCT is used where the coil section is located at the upper part, and fans are installed at the lower part. In the coil section, coils, spray system, eliminator and the other peripherals connecting the parts are sequentially organized and are kept in a casing. The copper coil with an outer diameter of 19.05 mm is used in the 0.6 m ×0.304m×0.525m dimensional tower and in a staggered arrangement. The cooling water is supplied by pipes and the pipes are connected to the distribution head through 8 horizontal cooling coils. The cooling water flows downward from the top. The spray water is uniformly distributed at the upper part of the coils by pump and circulates in the tower. The lower water tank section consists of a cooling water collecting tank and ambient air forcing fans. Ambient air constrains were maintained to the required state with the help of air-heater and humidifier. Table 1 gives the experimental conditions and the tower geometry.

Table 1: Specification of heat exchanger and Experimental conditions

Tube diameter	19.05		[mm]
Transverse pitch	38.1		
Cooling Water	Flow rate	[kg/h]	600-3120
	Inlet temperature	[^{o}C]	32-50
Spray Water	Flow rate	[kg/h]	720-2160
Air	Velocity	[m/s]	1.0-3.5
	Inlet wet-bulb temp.	[^{o}C]	22-29

Cooling water flows inside the coils of the CWCT. The cooling water after coming out through the outlet of the CWCT is sent to the constant temperature tank. The cooling water gains heat and gets stabilized to a certain temperature while passing though the constant temperature tank. Then, it re-circulates to the CWCT.

The T-type thermocouple temperature sensor with a diameter of 0.3 mm is used while measuring the temperature of cooling water and air at the inlet and the outlet of the CWCT. The humidity sensor is used to measure the humidity. The humidity and temperature at 5 points in the air inlet and the outlet are measured at every 5 seconds and the averages of these values are applied. Under the experimental conditions given in Table 1, the experiment was conducted changing the flow rate and inlet temperature of cooling water, flow rate of spray water and wet-bulb temperature and velocity of inlet air. The data were recorded with the help of automatic data logger, and all the readings at all inlets and outlets were collected after the experiment stabled in a steady state.

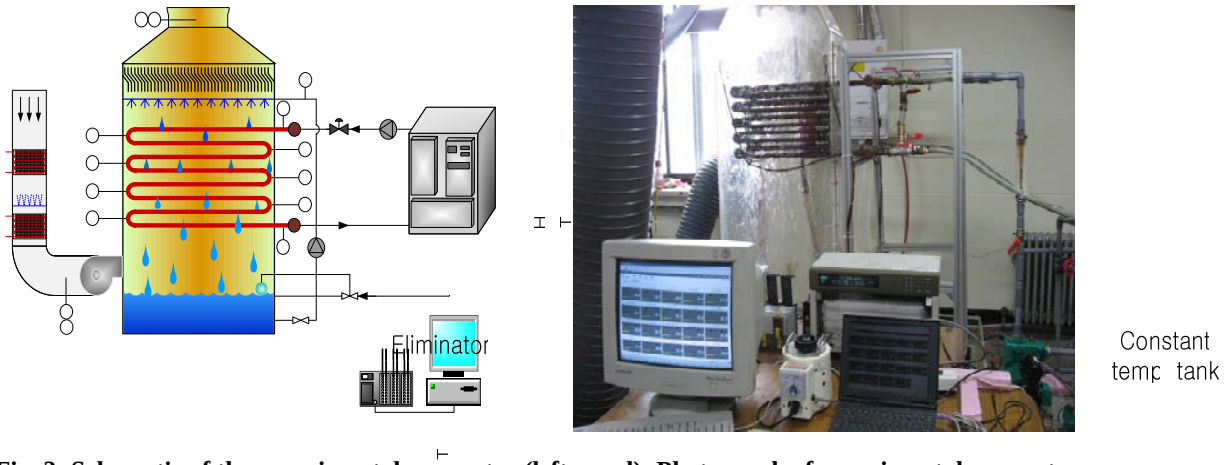

Fig. 2: Schematic of the experimental apparatus (left panel); Photograph of experimental apparatus (right panel)

3. THEORITICAL BACKGROUND

Heat transfers from a hot process fluid inside tubes to spray water and to air through a water film. Heat transfer is in latent and sensible forms when heat transfers from spray water to air. The rate of heat lost by cooling water is given by ,

$$dq_w = m_w c_{p_w} dt_w = U_o (t_w - t_s) dA \quad (1)$$

The rate of heat gain by air is,

$$dq_a = m_a di_a = k(i' - i_a) dA \quad (2)$$

The mass transfer coefficient can be obtained using mass balance.

$$m_a (x_{a,2} - x_{a,1}) = kA dx_{LM} \quad (3)$$

where, dx_{LM} is the logarithmic mean humidity difference, more details about the underlying theory can be found from [1-3].

4. RESULT AND DISCUSSION

To check the reliability of the experimental apparatus using the heat and mass transfer balance, equations (1) and (3) are used. The results have been shown in Fig. 3 where the heat balance data those have fallen within ±15% were used. The heat balance of the apparatus could be claimed to be satisfactory.

Fig. 4 shows the mass transfer coefficient *k* with respect to (w.r.t) air velocity and Γ in the CWCT. In the left panel of fig. 4, mass transfer coefficients are compared to the values of the correlations by Parker and Treybal [1], Mizushina et al [2] and Nitsu et al [3]. In case of the CWCT using one path, mass transfer coefficients are similar to the correlation of Parker and Treybal [1]. This means that there is a high reliability of the experimental apparatus. It is observed that mass transfer coefficients which were calculated in the CWCT having one path and two paths, increased with the increase of the air velocity. Mass transfer coefficients having two paths are approximately 43%, 17% higher than those having one path when air velocity were 1m/s and 3.5m/s respectively. This is mainly because the measured temperature of spray water in the surface of tubes having two paths are higher than the other and then it caused to increase the absolute humidity at the outlet of CWCT having two path.

Fig. 4 (right panel) shows the changes of mass transfer coefficient *k* w.r.t Γ in the CWCT. Γ means flow rate of spray water per unit breadth. Mass transfer coefficients in the CWCT using two and one path do not show any significant increase with regard to spray water flow

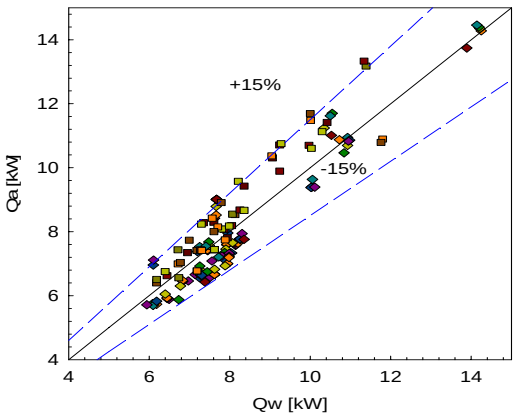

Fig. 3: Heat balance of the experimental apparatus

rate compared to the variable air velocity. The difference of mass transfer coefficients tends to decrease with the increasing spray water flow rate. Mass transfer coefficients in the CWCT using two path are about 28%, 17% higher than one having one path when Γ= 8.6806e-3 and 0.0226 kg/ms respectively.

Fig. 5 shows heat transfer coefficients h_o w.r.t air velocity and Γ in the CWCT. In both figures heat transfer coefficients, which were calculated in the CWCT using one path, similar to the correlation by Nitsu et al [3]. Furthermore, heat transfer coefficients as using two paths are similar to the correlation of [1]. It indicates that heat transfer coefficients are increasing as increasing Γ and shows hardly any increase w.r.t air velocity. Heat transfer coefficients in the CWCT using two paths are higher than those in one path in both figures.

Range with respect to a variable cooling water inlet temperature (CWIT) and wet-bulb temperature (WBT) are shown in Fig. 6. It is evident that range increases almost linearly with the increasing temperature of cooling water. At the standard design condition, ranges which were measured in the CWCT using one and two path are respectively 4.2^o C, and 5.1^o C. Range in the CWIT using two paths is approximately 20% higher than that with one path.

Fig. 6 (right panel) shows range with a variable inlet wet-bulb temperature. From this figure it is clear that the range decreases with the increase of the wet-bulb temperature. This is because when the wet-bulb temperature at the inlet increases, the temperature difference between the inlet cooling water and air decreases. Thus, the vaporization of the spray water outside the pipes decreases so that the falling of the temperature of the cooling water flowing inside the tubes deceases. Ranges of the CWIT using two paths are higher than that in one path at all cases. This is mainly because the heat transfer coefficient for water inside tubes of

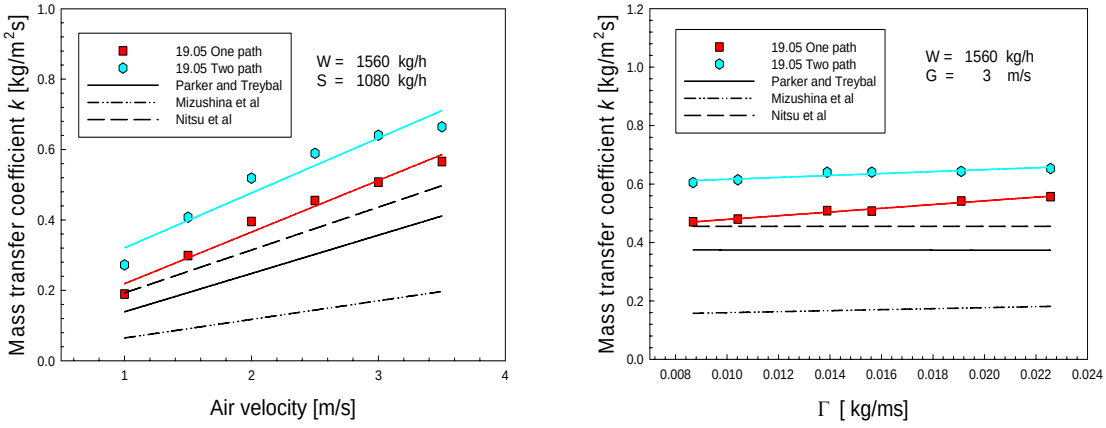

Fig. 4: Mass transfer coefficient *k* w.r.t air velocity (left panel); and Mass transfer coefficient *k* w.r.t spray water flow rate (right panel)

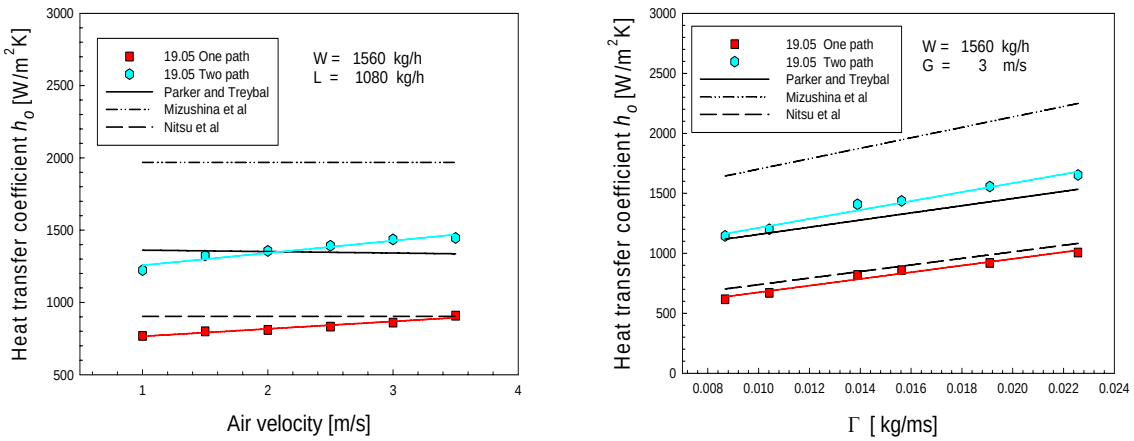

Fig. 5: Heat transfer coefficient h_o w.r.t air velocity (left panel); and Heat transfer coefficient h_o w.r.t spray water flow rate (right panel)

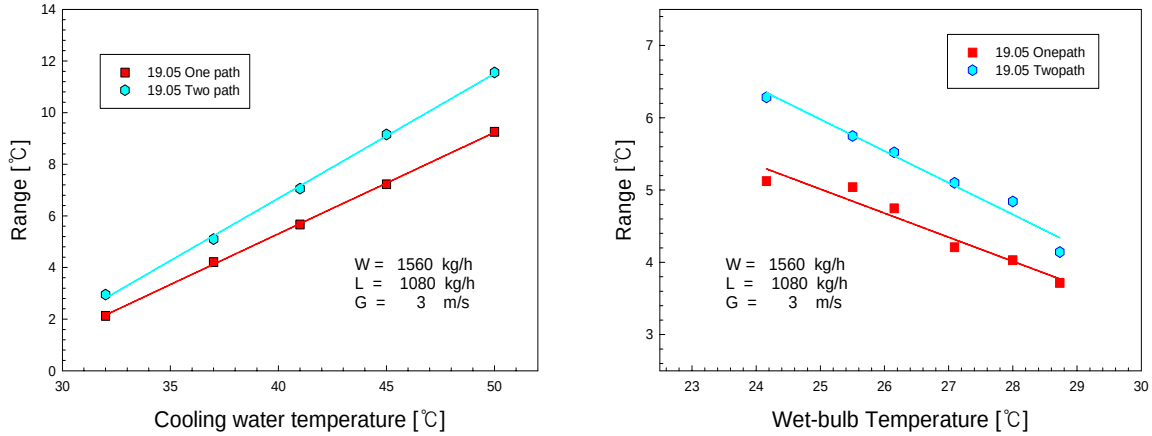

Fig. 6: Temperature range w.r.t inlet cooling water temperature (left panel); and Temperature range w.r.t inlet wet-bulb temperature (right panel)

the CWCT using two path is almost two times higher than the other.

Fig.7 shows cooling capacity with respect to air velocity and cooling water flow rate. Cooling capacity of the CWCT having two paths is remarkably higher than that with one path in both cases due to the significant enhancement of heat transfer coefficient in germane cases.

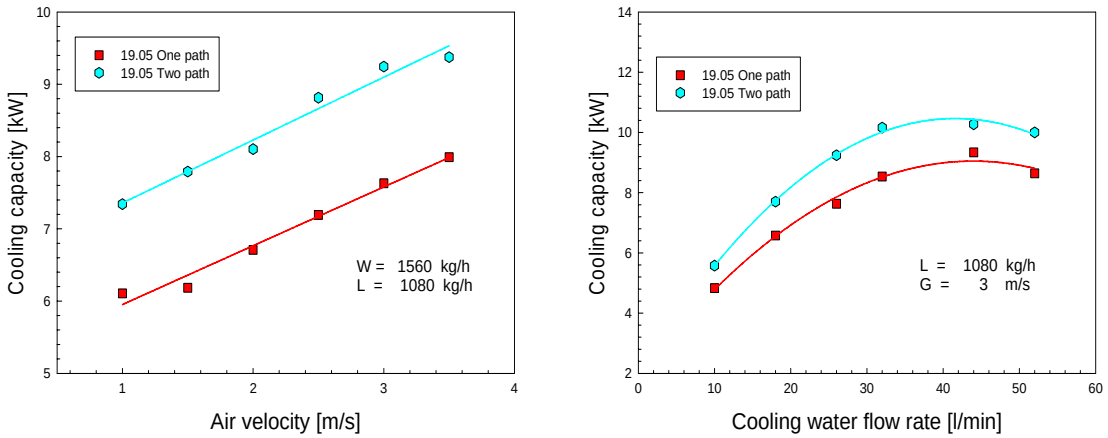

Fig. 7: Cooling capacity w.r.t air velocity (left panel); and Cooling capacity w.r.t cooling water flow rate (right panel)

5. CONCLUSIONS

The fundamental study on the performance characteristics of the closed-wet cooling tower with multi path has been done experimentally having a rated capacity of 2RT. The results could be summarized as follows:

1. Heat and mass transfer coefficient of the CWCT using one path was found to conform well to the already reported results for almost all cases considered.
2. In the optimum level, mass transfer coefficients for variable air velocity and spray water flow rate of the CWCT having two paths are respectively about 43% and 28% higher than those having one path.
3. The range of the CWCT using two paths is nearly 20% higher than that with one path.

ACKNOWLEDGEMENT

This work was partially supported by NURI Project in 2008.

NOMENCLATURE

A	Area [m^2]	**Subscript**	
D	Tube diameter [m]	a	Air
h	Convective heat transfer coefficient [w/m^2k]	i	Inside
i	Enthalpy [kJ/kg]	o	Outside
λ	thermal conductivity [w/mk]	w	Cooling water
m	Mass flow rate [kg/s]	1	Inlet
q	Rate of heat transfer [W]	2	Outlet
		3	Interface (spray water film/air)

REFERENCES

[1] Parker, R.O., and Treybal, R. E., The heat, mass transfer Characteristics of Evaporative coolers, Chemical Engineering Progress Symposium Series, 1961, pp. 57-32, pp.138-149.

[2] T. Mizushina, R ito, H. Miyashita, Characteristics and methods of thermal design of evaporative cooler, International Chemical Engineering, 8 (1968), 3, pp. 532-538.

[3] Nitsu, Y., K. Naito, and T. Anzai, , Studies of the Characteristics and Design Procedure of Evaporative Coolers, Journal of the society of Heating, Air-Conditioning, Sanitary Engineers of Japan, 41 (1969) 12, and 43 (1969), 7.

[4] S. V. Bedekar, P. Nithiarasu, K.N. Seetharamuz, Investigation of the performance of a counter-flow, packed-bed mechanical cooling tower, Energy, 23(1998), 11 pp. 943-947.

[5] Ala Hasan, Kai Siren, , Theoretical and analysis of closed wet cooling towers and its applications in cooling of buildings, Energy and buildings, 34 (2002), 5, pp. 477-486.

[6] Pascal Stabat, Dominique Marchio, Simplified for indirected-contact evaporative cooling-tower behaviour, Applied Energy, 85 (2003), 2-3, pp. 128-142.

[7] Jorge Facao, Armando Oliveira, Heat and mass transfer correlations for the design of small indirecr contacr cooling towers, Applied Thermal Engineering 24 (2004), 14-15, pp.1969-1978.

[8] M. M. A. Sarker, E. Kim, C. G. Moon, J.I.Yoon, Performance characteristics of the hybrid closed circuit cooling tower, Energy and Building 40 (2008), 8, pp. 1529-1535.

Proceedings of the 4th BSME-ASME International Conference on Thermal Engineering
27-29 December, 2008, Dhaka, Bangladesh

CRITICAL BEHAVIOR OF THE HYDROMAGNETIC FLOWS IN CONVERGENT-DIVERGENT CHANNEL

Md. Sarwar ALAM and Md. Abdul Hakim KHAN

Institute of Natural Science, United International University
Department of Mathematics, Bangladesh University of Engineering and Technology
Dhaka-1000, Bangladesh
e-mail: csemdsarwar@yahoo.com

ABSTRACT

The two-dimensional, steady, nonlinear flow of an incompressible conducting viscous fluid in convergent-divergent channel under the influence of an externally applied homogeneous magnetic field has been analyzed by means of Hermite – Pade′ approximation especially differential approximate method. A series related to similarity parameters is obtained by using algebraic programming language MAPLE. The series is then analyzed by approximate methods to show the dominating singularity behavior of the flow and the critical relationship among the parameters of the solution.

Key words: *Critical behavior, Hydromagnetic flow, Convergent-Divergent channel, Bifurcation.*

1. INTRODUCTION

In modern times the theory of flow through convergent-divergent channels have many applications in aerospace, chemical, civil, environmental, mechanical and bio-mechanical engineering as well as in understanding rivers and canals. The study of conducting viscous fluid flow through convergent-divergent channel under the influence of an external magnetic field is not only fascinating theoretically, but it also finds application in mathematical modeling of several industrial and biological systems. The mathematical investigations of this type of problem were pioneered by Jeffery [1] and Hamel [2], which was the classical flow of ordinary fluid dynamics. Jeffery-Hamel flows are interesting models of boundary layers in divergent channels. Fraenkel [3], Sobey and Drazin [4], Banks et al. [5] have studied extensively the problem in different ways. Makinde [6-7] investigated the Magneto Hydrodynamic (MHD) flows in convergent-divergent channels. He extended the classical Jeffery-Hamel flows of ordinary fluid dynamics to MHD. Makinde [7] studied that in the MHD solution an external magnetic field acts as a control parameter for both convergent and divergent channel flows. Hence, beside the flow Reynolds number and the channel angular width, at least an additional dimensionless parameter appears such as the Hartman number Ha. He obtained a perturbation series of twenty-four terms in powers of perturbation parameters Re, α and Ha and showed how the flows evolve and bifurcate as the flow parameters vary by using algebraic approximate method [9].

Our work extends the Makinde [7] by using the differential approximate method [8, 10]. We have analyzed the series to study the critical behaviour of the flow and the critical relationship among the parameters.

2. MATHEMATICAL FORMULATION

Consider the steady two-dimensional flow of an incompressible conducting viscous fluid from a source or sink at the intersection between two rigid plane walls under the influence of an externally applied homogeneous magnetic field as shown in Figure1. It is assumed that the fluid has small electrical conductivity and the electromagnetic force produced is very small. Let (r,θ) be polar coordinate with $r=0$ as the sink or source. Let α be the semi-angle and the domain of the flow be $-|\alpha| < \theta < |\alpha|$. Denote the velocity components in the radial and tangential direction by u and v respectively. The governing equations in terms of the vorticity (ω) and stream-function (ψ) can be written as [7]

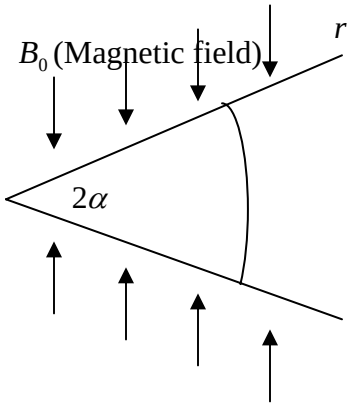

Fig 1: Convergent-Divergent channel

$$\frac{1}{r}\frac{\partial(\psi,\omega)}{\partial(\theta,r)} = \upsilon\ \nabla^2\ \omega - \frac{\sigma_e {B_0}^2}{\rho r^2}\omega, \qquad \omega = -\nabla^2\psi\ , \tag{1}$$

where $$\nabla^2 = \frac{\partial^2}{\partial r^2} + \frac{\partial}{r\partial r} + \frac{\partial^2}{r^2\partial\theta^2}$$

with the boundary conditions

$$\psi = \frac{Q}{2}, \quad \frac{\partial\psi}{\partial\theta} = 0, \qquad \text{at} \quad \theta = \pm\alpha \tag{2}$$

Here $Q = \int_{-\alpha}^{\alpha} urd\theta$ is the volumetric flow rate, $B_0 = (\mu_e H_0)$ the electromagnetic induction, μ_e the magnetic permeability, H_0 the intensity of magnetic field, σ_e the conductivity of the fluid, ρ the fluid density and υ is the kinematic viscosity coefficient..

For Jeffery-Hamel flow of conducting fluid, we assume a purely symmetric radial flow as described in [5], so that the tangential velocity $v=0$ and as a consequence of the mass

conservation, we have the stream-function given by $\psi = \frac{QG(\theta)}{2}$. If we require $Q \geq 0$ then for $\alpha < 0$ the flow is converging to a sink at $r = 0$.

The dimensionless form of equations (1)-(2) is

$$\frac{d^4G}{d\eta^4} + 2\,\mathrm{Re}\,\alpha \frac{dG}{d\eta}\frac{d^2G}{d\eta^2} + (4 - Ha)\alpha^2 \frac{d^2G}{d\eta^2} = 0 \tag{3}$$

with $$G = 1,\ \frac{dG}{d\eta} = 0,\ \text{at}\ \ \eta = \pm 1 \tag{4}$$

where $\eta = \frac{\theta}{\alpha}$ and $Ha = \sqrt{\frac{\sigma B_0{}^2}{\rho\upsilon}}$, $\mathrm{Re} = \frac{Q}{2\upsilon}$ are the Hartmann number and the flow Reynolds number respectively.

The problem defined by equation (3) is non-linear, for small channel angular width, one can obtain a series of the form

$$G(\eta) = \sum_{i=0}^{\infty} G_i \alpha^i \tag{5}$$

We then find that $G(\eta)$ has a singularity at $\alpha = \alpha_c$ of the form

$$G(\eta) \sim C(\alpha_c - \alpha)^{\beta_c}$$

with the critical exponent β_c.

Substituting the above expressions (5) into (3) and collecting the coefficients of like powers of α and with the help of MAPLE, we have computed the first 18 terms for stream-function G in terms of α, Re, Ha. The first few terms of the expansion of G are

$$\mathrm{G}(\eta;\alpha,\mathrm{Re},\mathrm{Ha}) = \frac{1}{2}\eta(3-\eta^2) - \frac{3}{280}\eta(\eta^2-5)(\eta-1)^2(\eta+1)^2\alpha\,\mathrm{Re} - \frac{1}{431200}\eta(98\eta^6 - 959\eta^4$$
$$+ 2472\eta^2 - 2875)(\eta-1)^2(\eta+1)^2\alpha^2\,\mathrm{Re}^2 + \frac{1}{40}\eta(\eta-1)^2(\eta+1)^2(4-\mathrm{Ha})\alpha^2 + \ldots$$

Although the computational complexity increases rapidly, we managed to compute the first 75 terms for G in terms of single parameter α for $\mathrm{Re} = 20$ and $Ha = 0,1,2,3,4,5$. We also computed the first 75 terms for G in terms of single parameter Re at $\alpha = 0.1$ for $Ha = 4$. These series are then analyzed by Differential approximate methods [8, 10] to determine the critical behaviour of the flow and used the algebraic approximate method [9] to show the bifurcation diagrams and the critical relationship among the parameters.

3. RESULTS AND DISCUSSIONS

For the analysis, we make use of the series in powers of α, Re and Ha for the following functional form:

$$G'(\eta = 0;\alpha,\mathrm{Re},Ha).$$

This quantity is proportional to the velocity of the flow along the centre line. By analyzing the series, we have calculated the location of the singularity with the critical exponents for different parameters. The results are obtained in terms of the critical channel angular width α_C and critical Reynolds number Re_C for different values of magnetic parameter Ha and these are shown in

Table 1-2 and graphically in Figure 2-6. In Table1 and 2, it is shown that α_C and Re_C increases uniformly as Ha increases which are comparable with the results of Makinde [7].

Tab.1: Comparisons of critical angles α_C and corresponding critical exponent β_c at $\mathrm{Re} = 20$ using High-order differential approximants [8]. The result is comparable with the result of Makinde [7].

HODA $d = 4$ $N = 18$	Ha	0	1	2	3	4	5
	α_C	.26797366	.26925148	.27037606	.27163028	.27290283	.27419950
	β_c	.49539333	.45619063	.50330153	.50119097	.50084769	.50079159
Makinde	Ha	0	1	2	3	4	5
	α_C	0.267960	0.269162	0.272906	0.279878	0.290431	0.307406
	β_c	0.50000	0.50000	0.50000	0.50000	0.50000	0.50000

Tab.2: Comparisons of critical Reynolds number Re_C and corresponding exponent β_c at $\alpha = 0.1$ using High-order differential approximants [8] and Makinde [7].

HODA $d = 4$ $N = 18$	Ha	0	1	2	3	4	5
	Re_C	54.44407939	54.47805874	54.51340970	54.54702585	54.58135150	54.61676356
	β_c	.4991155356	.4991155356	.4991155356	.4997069458	.5001231984	.4985944495
Makinde	Ha	0	1	2	3	4	5
	Re_C	54.4389	54.47179	54.58087	54.66510	55.22071	55.52727
	β_c	0.50000	0.50000	0.50000	0.50000	0.50000	0.50000

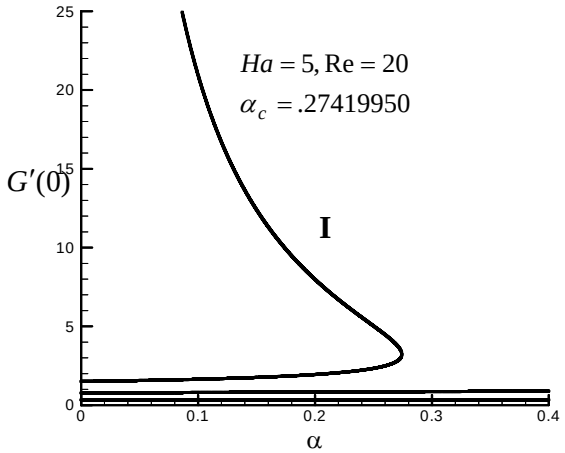

Fig. 2 Approximate bifurcation diagram (curve I) of α_c in the $(\alpha,\ G'(0))$ Plane with $Ha = 5$ obtained by Drazin-Tourigny [9] method for $d = 8$. The other curves are spurious.

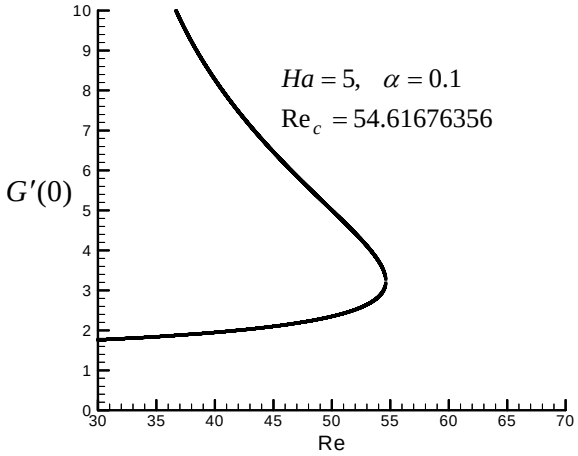

Fig. 3 Approximate bifurcation diagram of Re_c in the $(\mathrm{Re},\ G'(0))$ Plane with $Ha = 5$ obtained by Drazin-Tourigny [9] method for $d = 4$.

Fig. 2 and Fig. 3 display the approximate bifurcation diagram in the $(\alpha,\ G'(0))$ and $(\mathrm{Re},\ G'(0))$ plane respectively for $Ha = 5$ using Drazin-Tourigny [9] method . Therefore it is observed that the effect of magnetic intensity changes the solution behaviour of the problem.

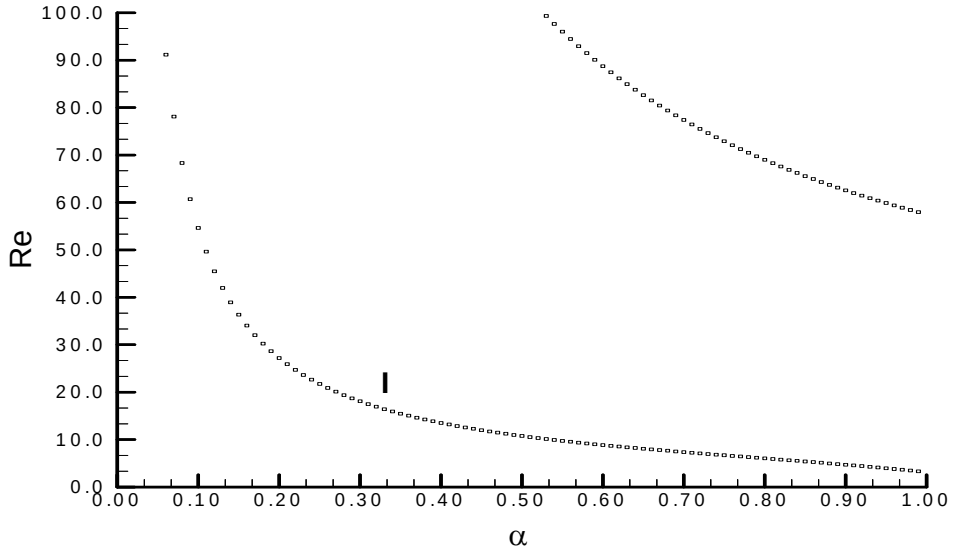

Fig.4: Critical α -Re relationship (curve I) using High-order partial Differential approximants [10] with $d = 6$. The other curve is spurious.

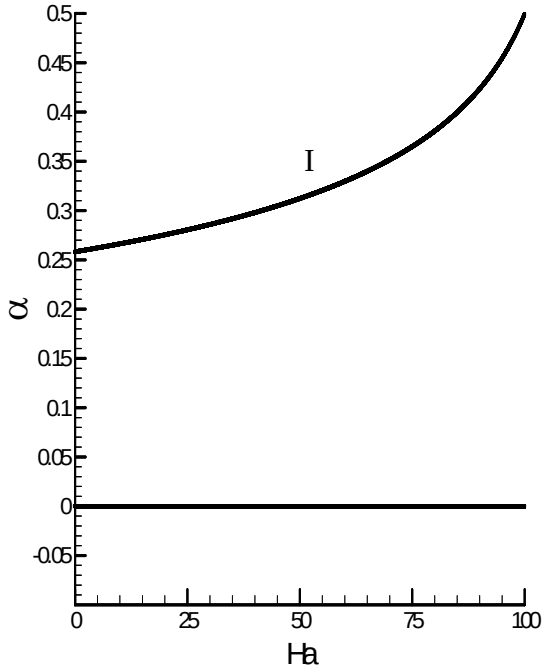

Fig.5: Critical $Ha - \alpha$ relationship (curve I) using High-order partial Differential approximants [10] with $d = 6$. The other curve is spurious.

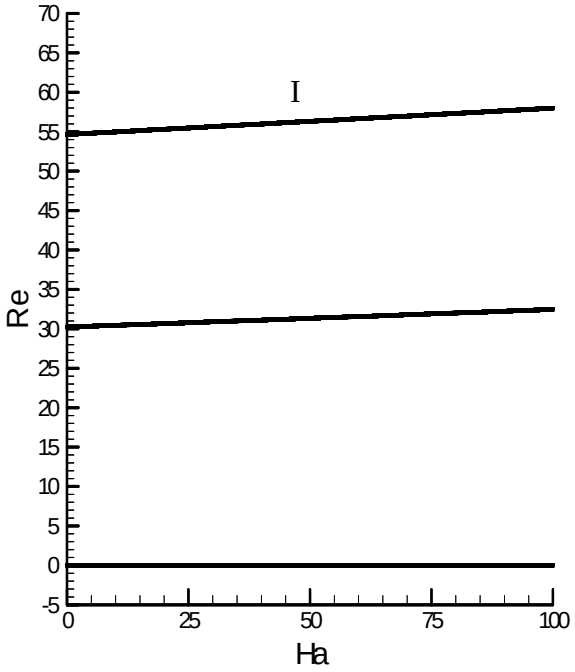

Fig. 6: Critical $Ha - \mathrm{Re}$ relationship (curve I) using High-order partial Differential approximants [10] with $d = 6$. The other curves are spurious.

The High-order Partial Differential Approximant [10] is applied to the series $G'(0;\alpha,\mathrm{Re},Ha)$ in order to determine the critical relationship of $\alpha_c, \mathrm{Re}_c, Ha_c$. In Fig 4, it is observe that as Re_c increases then α_c decreases. Fig. 5 and Fig. 6 show that α_c and Re_c changes significantly with the changes of magnetic parameter Ha.

4. CONCLUSION

In this paper, we have used power series to study the singularity behaviour of the nonlinear problem of hydromagnetic Jeffery-Hamel flow by using series summation technique. Our results confirm the conjecture of Makinde [7] with a little difference. Remarkably, we have shown the critical relationship among the parameters of the flow. We provide a basis for guidance about what method of summing power series should be chosen for many problems in fluid dynamics in order to show the critical behaviour of the flow. The procedure reveals asymptotically the analytical structure of the solution function.

5. REFERENCES

[1] Jeffery, G. B., The two-dimensional steady motion of a viscous fluid, *Phil Mag.,* Vol.6 (1915), pp 455-46.

[2] Hamel, G., Spiralförmige Bewgungen Zäher Flüssigkeiten, *Jahresbericht der Deutschen Math. Vereinigung,* Vol.25 (1916), pp 34-60.

[3] Fraenkel, L. E., Laminar flow in symmetrical channels with slightly curved walls. I: On the Jeffery-Hamel solutions for flow between plane walls, *Proc. R. Soc.Lond.* Vol.267 (1962), pp 119-138.

[4] Sobey, I. J., Drazin, P. G., Bifurcations of two-dimensional channel flows, *J. Fluid Mech.* Vol.171 (1986), pp 263-287.

[5] Banks, W. H. H., Drazin, P. G., Zaturska, M. B., On perturbation of Jeffery-Hamel flow, *J. Fluid Mech.,* Vol.186 (1988), pp 559-58.

[6] Makinde, O. D., Steady flow in a linearly diverging asymmetrical channel, *CAMES* Vol.4 (1997), pp 157-165.

[7] Makinde, O. D., *Hermite – Pade'* Approximation approach to Hydromagnetic flows in convergent-divergent channels, (Report), The Abdus Salam International Centre for Theoretical Physics, 2005, Trieste, Italy.

[8] Khan, M.A.H., High-Order Differential Approximants, J. of Comp. & Appl. Maths Vol.149 (2002), pp 457-468.

[9] Khan, M.A.H., Drazin P. G., Tourigny, Y., The summation of series in several variable and its applications in fluid dynamics, *Fluid Dynamics Research,* Vol.33 (2003),191-205.

[10] Rahman, M.M., A New Approach To Partial Differential Approximants, M. Phil thesis, BUET, Dhaka, 2004.

Proceedings of the 4th BSME-ASME International Conference on Thermal Engineering
27-29 December, 2008, Dhaka, Bangladesh

DRAG AND TORQUE COEFFICIENTS OF A STATIONARY SIX BLADED VERTICAL AXIS VANE TYPE ROTOR

Faizul Mohammad Kamal[1] and Md. Quamrul Islam[2]

[1]Atomic Energy Centre, Ramna, Dhaka-1000, Bangladesh
[2]Department of Mechanical Engineering
Bangladesh University of Engineering & Technology, Dhaka-1000, Bangladesh
Email address: kamal_ndt@yahoo.com

ABSTRACT

This research work has been carried out to study the aerodynamic characteristics i.e. torque coefficient, drag coefficient etc. of an equally spaced vertical axis six bladed vane type rotor by measuring the pressure distribution on the blade surfaces at various rotor angles. The experimental investigation was performed at Reynolds number 1.65 $\times 10^5$ in a uniform flow jet produced by an open circuit wind tunnel. It has been observed that the total static torque coefficient decreases from 0^0 to 20^0 angle of rotation, and then increases up to 60^0. Then total static torque coefficient at different rotor angles curve repeats from 60^0 to 110^0, 120^0 to 170^0, 180^0 to 230^0, 240^0 to 290^0 and 300^0 to 350^0 angle of rotation. A quasi-steady approach was applied for the prediction of dynamic performance of the rotor using the static drag and torque coefficients. This method results in a fair agreement with the measured power coefficients.

Key words: *Vertical axis wind turbine, wind tunnel, drag coefficient, torque coefficient.*

1. INTRODUCTION

Both aerodynamic and structural works on the vertical-axis Savonius wind turbine have been done in many parts of the world. Islam et al. [1] investigated the aerodynamic forces acting on a stationary S-shaped rotor and made an attempt to predict the dynamic performance from these forces. Islam et al. [2] analyzed the performance of S-shaped rotor by placing a flat plate in front of the retreating blade. F. Diaz et al. [3] analyzed the drag and lift coefficient of Savonius wind machine in order to obtain quantitative information about the Savonius rotor. Ogawa et al. [4] studied the performance of the Savonius rotor with circular guide vanes. Rigorous studies on the performance characteristics of Savonius rotor are found in the literatures and these enable the identification of an optimum geometrical configuration for practical design [5, 6, 7, 8].

The present research work has been carried out to study the aerodynamic characteristics i.e. torque coefficient, drag coefficient etc of a vertical axis equally spaced six bladed vane type rotor. Later in this paper a comparison has also been made between the present dynamic predictions (for six bladed vertical axis vane type rotor) with previous work of vertical axis wind turbine (Three bladed Savonius rotor) in terms of power coefficient for different tip speed ratios.

2. EXPERIMENTAL SETUP AND PROCEDURE

2.1 Wind Tunnel

The experimental setup of the present investigation has been shown in the schematic diagram of Figure 1. An open circuit subsonic type wind tunnel was used to develop the required flow, and the rotor was positioned at the exit section of the wind tunnel. The tunnel was 5.93 meter long with a test section of 460 mm x 480 mm in cross-section. In order to smoothen the flow, a honeycomb was fixed near the outlet

of the wind tunnel. The setup had a bell-shaped converging duct at the entry. To generate the wind velocity, two axial flow fans were used, with each of the fans connected to a motor of 2.25 kW capacity and 2900 rpm. A butterfly valve was used to control the flow rate. A silencer was connected just after the butterfly valve for reduction of the noise.

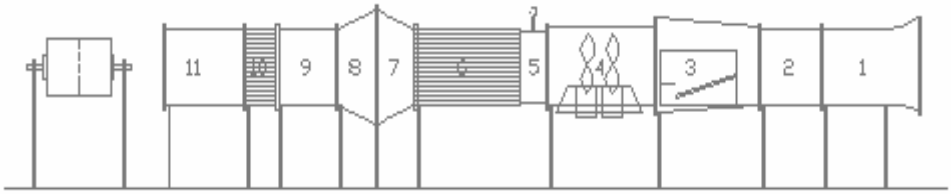

1	Converging entry	7	Diverging section
2	Perspex section	8	Converging section
3	Rectangular diverging section	9	Rectangular section
4	Fan section	10	Flow straightener section
5	Butterfly section	11	Rectangular exit section
6	Silencer with honeycomb section		

Fig. 1: Schematic diagram of wind tunnel.

The central longitudinal axis of the wind tunnel was always kept at a constant height of 990 mm from the floor. The axis of the model was also placed coinciding with the axis of the wind tunnel. The converging duct inlet was then merged into the wind tunnel so that air can enter smoothly into the tunnel and maintain uniform flow into the duct, keeping it free from any outside disturbances. The flow through the wind tunnel was induced by a two-stage rotating axial flow fan of 18.16 m^3/s capacity with a head of 152.4 mm of water and running at 1475 rpm.

2.2 The Six Bladed Vane type Rotor

The constructional detail of the six bladed vane type rotor [9] is shown in the Figure 2. Six bladed vane type rotor was made up of six half cylinders (blade) of diameter, d = 65 mm and height, H = 340 mm. Rotor diameter, D was 200 mm. Optimum value of d/D ratio was taken as 3. The cylinders were made of PVC material. The center-to-center distance of the blade was 137.5 mm. The whole rotor was fixed on an iron frame by using two side shafts and two ball bearings. The pressure measurements were made at 8 pressure tappings on each blade.

Fig. 2: Six bladed vertical axis vane type rotor.

2.3 The Experimental Procedure

The pressure distribution over the blade surfaces was measured step by step by using the multi-manometer. At first, the vane rotor with the frame was placed 500 mm down stream of the exit section of the wind tunnel. One blade of the rotor was fixed parallel to the free stream velocity i.e. parallel to the horizontal, which was called the reference plane and from this plane angle of rotation was measured. At the beginning, the first blade was at 0° angle of rotation, exposing the convex surface in front of free stream air, so the other five blades were at 60°, 120°, 180°, 240° and 300° angle of rotation respectively. The rotor was then made static by fixing one end of the shaft with the angle-fixing device. Then power was supplied to the motor of the wind tunnel for starting flow of the free stream air of uniform velocity over the blades of the rotor. Pressure on the convex surface of blades was measured at a particular rotor angle α, fixing the rotor at static condition. Gradually, pressure on the convex surfaces was measured in this process for every 10° interval of rotor angle up to 350° angle of rotation. The same steps were performed for the measurement of the pressure on the concave surfaces.

3. RESULTS AND DISCUSSION

3.1 Drag Coefficient

Normal drag coefficient, C_n of an individual blade effect of six bladed vane rotor is shown in Figure 3 for different rotor angles. For the flow over the six-bladed system, considering a single blade the normal drag coefficient $C_n(\alpha)$ decreases with the increase of the rotor angle from $\alpha=0^\circ$ to 10°, and then increases up to 130°. From $\alpha=130^\circ$ to $\alpha=210^\circ$, drag coefficient $C_n(\alpha)$ decreases linearly. Between $\alpha=0^\circ$ to $\alpha=180^\circ$, drag coefficient $C_n(\alpha)$, is positive for a rotor angle of 110° to 180° and reaches its maximum value at $\alpha=130^\circ$. The value of C_n increases from $\alpha=210^\circ$ to $\alpha=300^\circ$ and then again decreases from $\alpha=300^\circ$ to $\alpha=320$. After that it slightly rises up to $\alpha=330^\circ$. From $\alpha=330^\circ$, the value of C_n sharply falls till $\alpha=360^\circ$. Therefore, positive torque is available between $\alpha=110^\circ$ to $\alpha=200^\circ$ and $\alpha=220^\circ$ to $\alpha=340^\circ$. Negative torque is available between $\alpha=0^\circ$ to $\alpha=100^\circ$, $\alpha=210^\circ$ and $\alpha=350^\circ$ to $\alpha=360^\circ$.

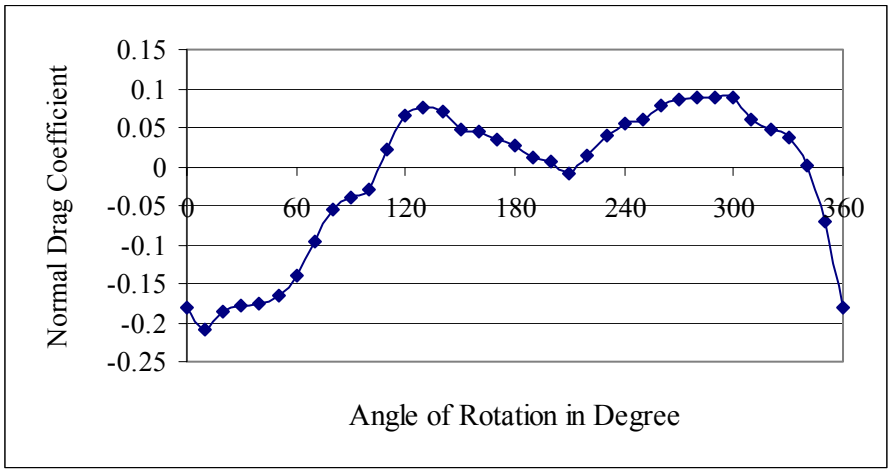

Fig. 3: Normal drag coefficient of individual blade effect.

Normal drag coefficient, C_n with six blades combined effect is shown in Figure 4 for different rotor angles. Drag coefficient, C_n increases with the increase of the rotor angle from $\alpha=0^\circ$ to $\alpha=20^\circ$, and then decreases up to $\alpha=60^\circ$. The system repeats from $\alpha=60^\circ$ to $\alpha=110^\circ$, $\alpha=120^\circ$ to $\alpha=170^\circ$, $\alpha=180^\circ$ to $\alpha=230^\circ$, $\alpha=240^\circ$ to $\alpha=290^\circ$, and $\alpha=300^\circ$ to $\alpha=350^\circ$. In the six bladed system, the C_n rises and falls sharply.

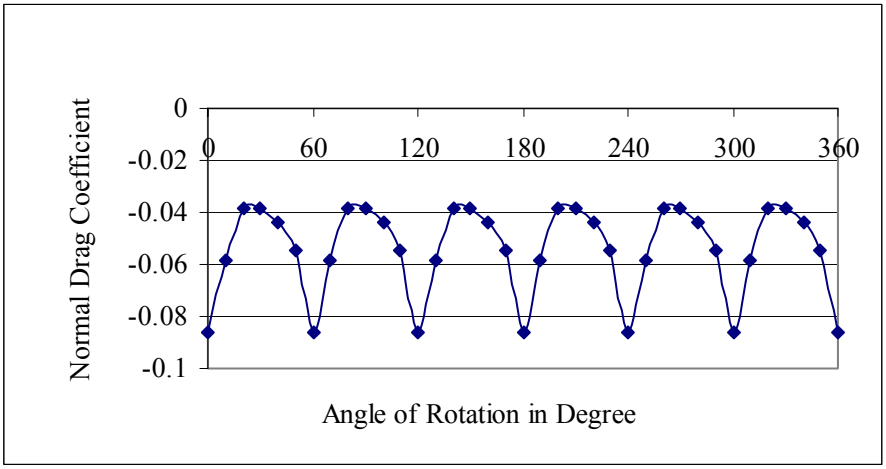

Fig. 4: Normal drag coefficient with combined blade effect.

3.2 Torque Coefficient

Torque coefficient, C_q of an individual blade of six bladed vane rotor is shown in Figure 5 for different rotor angles. Considering the flow over the six-bladed system, on the first blade, the torque coefficient, C_q increases with the increase of the rotor angle from α=0˚ to 10˚, and then decreases up to 130˚. From this point the drag coefficient increases up to 210˚. Between α=0˚ to α=100˚, the torque coefficient C_q is positive for a rotor angle of 0˚ to 100˚ and reaches its maximum value at α=10˚. The coefficient decreases from α=210˚ to α=300˚. From then onwards, the C_q increases from α=300˚ to α=320˚ and slightly falls at α=330˚. It increases from α=330˚ to α=360˚. Therefore, the positive torque is available for a rotor angle of 0˚ to 100˚ and from 340˚ to 360˚. Negative torque is available for a rotor angle of 110˚ to 200˚ and from 220˚ to 330˚.

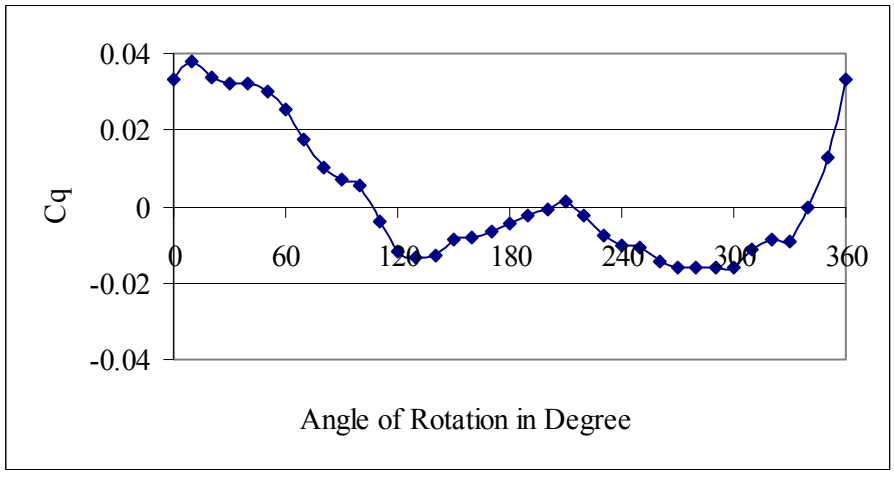

Fig. 5: Torque coefficient with individual blade effect.

Total static torque coefficient, C_q with six blades Vane rotor is shown in Figure 6 at different rotor angles. For the six-bladed system, the nature of the curve repeats after 50° angle of rotation like that of the normal drag coefficient due to combined effect. The value of torque coefficient is smaller than that of normal drag coefficient with combined blade effect. The total static torque coefficient is positive where normal drag coefficient for combined blade effect is negative value. Here the total static torque decreases with the increase of the rotor angle up to α=20˚. From this point the coefficient C_q increases till α=60˚. Then the curve repeats. The curve repeats from 60˚ to 110˚, from 120˚ to 170˚, from 180˚ to 230˚, 240˚ to 290˚ and from 300˚ to 350˚.

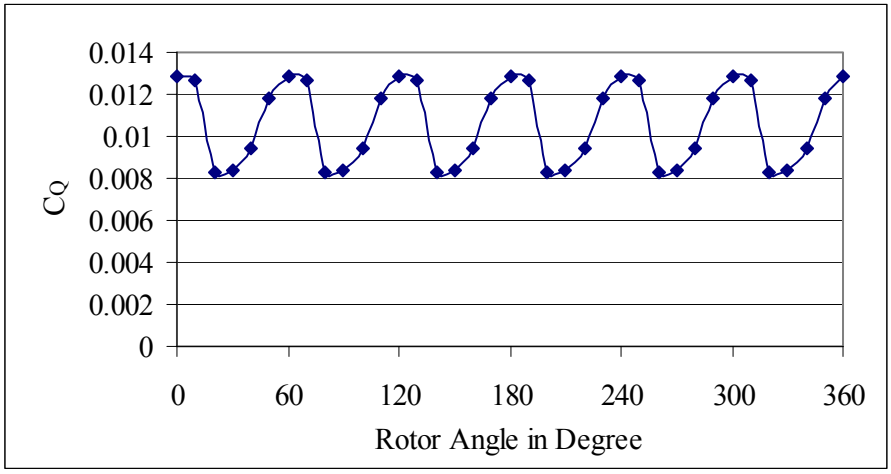

Fig. 6: Total static torque coefficient at different rotor angle.

3.3 Power Coefficient

The quasi-steady approach applied for the analysis of a Darrieus rotor has been considered for predicting the performance of the vane rotor. The static drag coefficient obtained experimentally at a blade angle of α, has been used in conjunction with the relative velocity, V_r corresponding to a particular tip speed ratio, λ to evaluate the force acting on the blade. The power coefficient has been estimated by averaging the work done over a cycle.

The predicted power coefficients, C_p for different tip speed ratios, λ are shown in Figure 7 for six bladed vane rotor along with the measured data of Rahman [10]. The present method assumes a potential vortex. However, in reality the flow field around a rotating rotor is also dependent and governed by shear layers, flow separation, high turbulence level, etc. Furthermore, the effect of wake formation has not been considered in the present study.

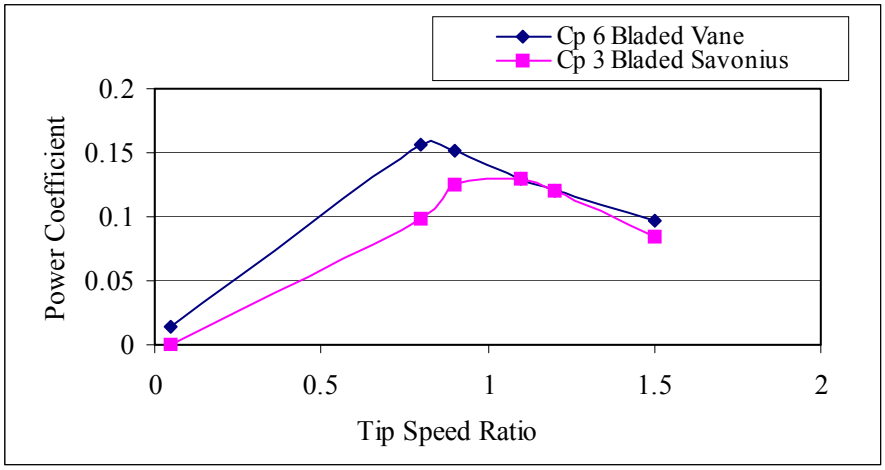

Fig. 7: Power coefficient versus tip speed ratio.

4. CONCLUSIONS

The following conclusion can be drawn from the present study:

i) The drag varies with different rotor angle. This contributes significantly for producing torque. The nature of the torque coefficient is opposite to that of the normal drag coefficient on the individual blade of the six bladed vane type rotor.

ii) Total static torque coefficients for six bladed vane rotor at different rotor angle were also

analyzed in the present research work. In the case of six bladed rotor, it is found that the curve repeats after 50° angle of rotation like that of the normal drag coefficient due to combined effect. For six bladed vane type rotor, the net torque is always positive.

iii) For study of dynamic characteristics, the measured power coefficients (C_p) for different tip speed ratio (λ) of the present research work matches with the nature of the theoretical C_p vs. λ curve. Comparing with the existing measured data, the present study agrees well with the curves of other research works.

5. NOMENCLATURE

C_n normal drag coefficient
C_t drag coefficient in the transverse direction of the chord
C_q static torque coefficient for a single blade
C_Q total static torque coefficient
D diameter of the vane rotor
R_e Reynolds number, U_0D/ν
S ratio between distance of two blades and diameter of a blade
U_0 free stream velocity
V_r relative velocity

Greek Symbols:
α rotor angle
Φ angle of pressure tappings
λ tip speed ratio, $D\omega/2U_0$
ω angular speed of the rotor
ν kinematics viscosity of air

6. REFERENCES

[1] Islam, A.K.M.S, Islam, M.Q., Mandal, A.C., Razzaque, M.M., Aerodynamic Characteristics of a Stationary Savonius rotor, *RERIC Int. Energy Journal*, Vol. 15(1993), No. 2. pp. 125-135.

[2] Islam, A.K.M.S, Islam, M.Q., Razzaque, M.M., Ashraf, R., Static Torque and Drag Characteristics of an S-shaped Savonius Rotor and Prediction of Dynamic Characteristics, *Wind Engineering*, Vol. 19(1995), No. 6, U.K.

[3] Gavalda, J.,Massons J., Diaz, F., Drag and Lift Coefficients of the Savonius Wind Machine, *Wind Engineering*, Vol. 15(1991), No. 5, U.K.

[4] Ogawa, T., Tahara, K., Suzuki, N., Wind Tunnel Performance Data of The Savonius Rotor with Circular Guide Vanes, *Bulletin of JSME*, Vol. 29(1986), No. 253. pp. 2109-2114.

[5] Aldos, T.K., Savonius Rotor Using Swinging Blades as an Augmentation System, *Wind Engineering*, Vol. 18(1984), No. 4, U.K.

[6] Aldos, T.K., Obeidat, K.M., Performance Analysis of Two Savonius Rotors Running Side by Side Using The Discrete Vortex Method, *Wind Engineering*, Vol. 11(1987), No.5, U.K.

[7] Fujisawa, N., Velocity Measurements and Numerical Calculations of Flow fields in and Around Savonius Rotors, *Journal of Wind Engineering and Industrial Aerodynamics*, Vol. 59(1996), U.K.

[8] Huda, M.D., Selim, M.A., Islam, A.K.M.S., Islam, M.Q., The Performance of an S-shaped Savonius Rotor with a Deflecting Plate, *RERIC Int. Energy Journal*, Vol. 14(1992), No. 1, Bangkok, Thailand.

[9] Kamal, F. M., Aerodynamic Characteristics of a Vertical Axis Vane Type Wind Turbine, M. Sc. Engg. Thesis, Dept. of Mech. Engg., Bangladesh University of Engineering & Technology, Bangladesh, 2008.

[10] Rahman, M., Aerodynamic Characteristics of a Three Bladed Savonius Rotor, M. Sc. Engg. Thesis, Dept. of Mech. Engg., Bangladesh University of Engineering & Technology, Bangladesh, 2000.